



ADVANCED MASTERS IN STRUCTURAL ANALYSIS OF MONUMENTS AND HISTORICAL CONSTRUCTIONS

Master's Thesis

Demiana Tse

Numerical analysis of an earthen masonry structure subjected to blast loading



University of Minho

Portugal | 2021





ADVANCED MASTERS IN STRUCTURAL ANALYSIS
OF MONUMENTS AND HISTORICAL CONSTRUCTION



Master's Thesis

Demiana Tse

**Numerical analysis of an
earthen masonry structure
subjected to blast loading**

DECLARATION

Name: Demiana Tse

Email: tse.demiana@gmail.com

Title of the Msc Dissertation: Numerical analysis of an earthen masonry structure subjected to blast loading

Supervisor(s): Dr. João M. Pereira, Professor Paulo B. Lourenço

Year: 2020/2021

I hereby declare that all information in this document has been obtained and presented in accordance with academic rules and ethical conduct. I also declare that, as required by these rules and conduct, I have fully cited and referenced all material and results that are not original to this work.

I hereby declare that the MSc Consortium responsible for the Advanced Masters in Structural Analysis of Monuments and Historical Constructions is allowed to store and make available electronically the present MSc Dissertation.

University: Universidade do Minho

Date: July 16, 2021

Signature:



This page intentionally left blank.

To the future...

This page intentionally left blank.

ACKNOWLEDGEMENTS

This work was developed within the framework of the SAHC Masters Course at the University of Minho. The research was conducted under the joint supervision of Dr. João M. Pereira and Prof. Paulo B. Lourenço from the University of Minho.

This thesis would not have been possible without all those who helped me both professionally and personally. First and foremost, I would like to thank Dr. João M. Pereira for his continuous support during the dissertation. This research relied heavily on his expertise, and I have enjoyed tackling this project under his mentorship. His enthusiasm and knowledge in this topic made this thesis possible. I am deeply grateful to Professor Paulo B. Lourenço for his guidance in both the theoretical and technical aspects of this dissertation.

I owe a debt of gratitude to Dr. Javier Ortega and Annalaura Vuoto who shared indispensable information on the Moorish Tower. Without them, this case study could never have been completed during these challenging times. I must also thank Dr. Marco F. Funari and Giorgos Vlachakis for their help and tutoring using Abaqus.

I would like to thank the Fundação Millennium BCP for their generous financial support provided through the SAHC Millennium scholarship.

I am grateful to all the professors and lecturers I met during the SAHC program for showing me the different methods, applications, and issues in heritage conservation. I also owe special thanks to Dr. Mario Santana Quintero, from Carleton University, without whom I would never have found my passion for conservation and preservation of historical constructions.

Finally, I would not have been able to produce this work without my family and friends—both here in Guimarães and back in Ottawa—for all the moments of respite during these part months. Your love and support mean everything to me.

This page was intentionally left blank.

ABSTRACT

Historic monuments and constructions capture the knowledge of civilizations of the past and are a source of pride for people of the present. Over the centuries, these buildings have been at risk from natural and man-made causes. The Alhambra, a UNESCO World Heritage Site, is one of such places. Located in Granada, Spain, it was constructed between the 13th and 15th centuries, and is one of the last remaining palatine cities from the Islamic Period in the Iberian Peninsula. This thesis aims to evaluate the structural performance of the *Torre de la Vela*, a tower in the Alhambra, under blast and impact loads. The tower, constructed of rammed earth and brick masonry, has been mostly preserved in its original form.

This work can be divided into the following phases: a focus on the context of the Alhambra, a review of the state-of-the-art, the preparation and calibration of a 3D numerical model, and the structural analysis to assess the behaviour of the tower under blast and impact loading. The loads were based on historical records of barrels of gunpowder and were modelled as simplified pressure profiles using existing empirical equations. The effect of impulsive loading on the material properties was accounted for using dynamic increase factors, determined experimentally by previous authors. The problem was solved using explicit dynamic analysis available in Abaqus. Four numerical models were considered for the blast analysis, namely: a full model of the *Torre de la Vela*, a model of the South façade, a model of the second level, and a model of an interior wall. A model of the upper portion of the South façade was used in the impact analysis.

The results from the blast analysis for a load applied on the exterior of the full model concluded that the building would be safe under the applied load, based on the failure volume damage index. Comparisons made between the results obtained using continuum model and contact model led to the determination that the local displacements remained the same but the overall stress distributions in the models differed. Based on the failure volume damage index, a blast load applied inside the second level of the tower led to the conclusion that severe damage would occur in the interior of the building immediately after the application of the load. For the wall experiencing the most damage, a smaller mesh size led to more accurate damage patterns. The removal of elements exceeding a given damage threshold led to more visible damage patterns than the Concrete Tension Damage option in Abaqus. The use of a historical cannon ball as an impactor on the *Torre de la Vela* did not lead to any damage. Under impact loading, the continuum and contact models showed different displacements and stress distributions due to the difference in energy dissipation. Finally, a hypothetical impactor was modelled and only caused minimum damage to the surface of the wall.

This page was intentionally left blank.

RESUMO

Monumentos e construções históricas capturam o conhecimento de civilizações do passado e são motivo de orgulho para as pessoas do presente. Ao longo do tempo, estes edifícios estão sujeitos a ações naturais e feitas pelo Homem. A Alhambra, Patrimônio Mundial da UNESCO, é um desses lugares. Localizada em Granada, Espanha, foi construída entre os séculos XIII e XV, e é uma das últimas cidades palatinas remanescentes do Período Islâmico na Península Ibérica. Esta tese tem como objetivo avaliar o desempenho estrutural da *Torre de la Vela*, uma torre na Alhambra, quando sujeita a explosões e impacto. A torre, construída em taipa e alvenaria de tijolo, foi em grande parte conservada na sua forma original.

Este trabalho pode ser dividido nas seguintes fases: um enfoque no contexto da Alhambra, uma revisão do estado da arte, a preparação e calibração de um modelo numérico 3D e a análise estrutural para avaliar o comportamento da torre sujeita a explosões e impacto. As cargas foram baseadas em registros históricos de barris de pólvora e foram modeladas como perfis de pressão usando equações empíricas existentes. O efeito das velocidades de deformação nas propriedades do material foi tido em conta recorrendo a fatores de incremento dinâmico, determinados experimentalmente na literatura. Para resolução do problema, foi usada análise dinâmica explícita, disponível no Abaqus. Quatro modelos numéricos foram desenvolvidos para a análise de explosões: um modelo completo da *Torre de la Vela*, um modelo da fachada sul, um modelo do segundo andar e um modelo de uma parede interior. Um modelo da parte superior da fachada sul foi usado na análise de impacto.

Os resultados obtidos pela análise do modelo completo quando sujeito a explosão aplicada no exterior permitiram concluir que o edifício estaria seguro sob a carga aplicada, com base no índice de dano por volume de falha. As comparações feitas entre os resultados obtidos usando o modelo contínuo e o modelo de contato permitiram observar que os deslocamentos locais foram semelhantes, mas as distribuições de tensões diferiram, nos modelos. Com base no índice de dano por volume de falha, uma explosão com origem no segundo andar da torre originaria danos graves no interior do edifício imediatamente após a aplicação da carga. Com o modelo da parede mais danificada, foi possível observar que uma malha mais refinada permite obter padrões de dano mais precisos. A remoção de elementos que excedem um determinado limite de dano permitiu uma caracterização mais visual do dano na estrutura. Quando sujeita ao impacto de um projétil de canhão daquele período histórico, a *Torre de la Vela* não apresentou nenhum dano. Quando sujeito a impacto, os modelos contínuo e de contato mostraram diferentes deslocamentos e distribuições de tensões devido à diferença na dissipação de energia. Finalmente, um projétil hipotético foi modelado e causou apenas danos mínimos à superfície da parede.

This page was intentionally left blank.

RÉSUMÉ

Les monuments et constructions historiques capturent les connaissances des civilisations du passé et sont une source de fierté auprès des peuples du présent. À travers les siècles, ces édifices ont été à risque de causes naturelles et artificielles. L'Alhambra, un site sur la Liste du Patrimoine mondial UNESCO, est un de tels endroits. Situé en Grenade, Espagne, L'Alhambra a été construit entre les 13^e et 15^e siècles, et est une des dernières villes palatines restantes de la période islamique dans la péninsule Ibérique. Cette dissertation a comme but d'évaluer la performance structurelle de la « Torre de la Vela », une tour dans l'Alhambra, soumise à des explosions et à des impacts. La tour, construite de pisé et de maçonnerie de briques, a été en grande partie conservé dans sa forme originale.

Ce travail de recherche peut être divisé dans les sections suivantes : une étude sur le contexte de l'Alhambra, une revue de l'état de l'art, la préparation et calibration d'un modèle numérique trois-dimensionnelle, et finalement une analyse structurelle pour déterminer le comportement de la tour sous charge d'explosion et d'impact. Les charges ont été basées sur des barils de poudre à canon historiques et ont été modélisées comme des profils de pressions en utilisant des équations empiriques existantes. L'effet du chargement impulsif sur les propriétés matérielles a été représenté en utilisant des facteurs d'augmentation dynamiques, déterminés expérimentalement par des auteurs précédents. Le problème a été résolu en utilisant l'analyse dynamique explicite disponible dans Abaqus. Quatre modèles numériques ont été considérés pour l'analyse sous charge d'explosion, notamment : un modèle complet de la « Torre de la Vela », un modèle de la façade sud, un modèle du 2^e niveau, et un modèle d'un mur intérieur. Pour l'analyse sous charge d'impact, un modèle d'une portion supérieure de la façade sud a été utilisé.

Les résultats de l'analyse d'une charge d'explosion appliquée à l'extérieur du modèle complet de l'édifice ont conclu que l'édifice sera en sécurité sous la charge appliquée, basé sur l'indice de dommage du volume de défaillance. Des comparaisons entre les résultats obtenus en utilisant un modèle macroscopique et un modèle d'éléments de contact ont permis de déterminer que les déplacements locaux sont restés pareils, mais que les distributions de stress dans le modèle seront différentes. Basé sur l'indice de dommage du volume de défaillance, une charge explosive appliquée à l'intérieure du deuxième niveau de la tour a permis de conclure que des dommages sévères auront lieu à l'intérieur de l'édifice immédiatement après que la charge soit administrée. Pour le mur avec le plus de dommages, un maillage plus petit a mené à des modèles de dommages plus exacts. La suppression d'éléments qui dépassent un seuil donné de détérioration a permis de voir des motifs de détérioration plus visibles que celles de l'option « Concrete Tension Damage » dans Abaqus. L'utilisation d'un boulet de canon historique comme impacteur sur la « Torre de la Vela » n'a causé aucun dommage. Sous charge d'impact, les modèles macroscopiques et d'éléments de contact ont démontré des déplacements et des distributions de stress différents en raison de la différence dans la dissipation de l'énergie. Finalement, un impacteur hypothétique a été modélisé et a seulement causé des dommages mineurs à la surface du mur.

This page was intentionally left blank.

TABLE OF CONTENTS

1 INTRODUCTION.....1

2 THE ALHAMBRA AND THE *TORRE DE LA VELA*3

2.1 History of the Alhambra.....5

2.2 Layout of the Alhambra and the *Alcazaba*6

2.3 The *Torre de la Vela*8

2.3.1 Plans/Geometry9

2.3.2 Past Interventions and Construction Techniques13

3 STATE OF THE ART: LOADING AND ANALYSIS19

3.1 Blast Loading19

3.1.1 Scaling Laws.....21

3.1.2 Equivalent TNT.....21

3.1.3 External Blast Loading.....22

3.1.4 Internal Blast Loading29

3.1.5 Structural response32

3.2 Impact Loading.....34

3.2.1 Classifications of Impact Loading.....35

3.2.2 Structural response36

3.3 History of Military Weapons.....36

3.3.1 Gunpowder.....37

3.3.2 Cannons.....38

4 NUMERICAL MODEL.....41

4.1 Masonry Structures Under Blast Loading.....41

4.1.1 Abaqus/Explicit41

4.1.2 Concrete Damage Plasticity.....42

4.1.3 Material Behaviour at High Strain Rates.....44

4.1.4 Contact Interactions.....45

4.2 *Torre de la Vela*46

4.2.1 Finite Element Mesh47

4.2.2 Material Properties and Material Model49

4.3 Model Validation.....52

5 BLAST LOADING55

5.1	External Blast Loading.....	55
5.1.1	Loading Definition.....	55
5.1.2	Exterior Blast Results on Whole Building.....	56
5.1.3	Exterior Blast Results on Single Wall.....	64
5.2	Internal Blast Loading.....	70
5.2.1	Loading Definition.....	71
5.2.2	Interior Blast Loading Results on Level 2.....	72
5.2.3	Interior Blast Loading Results on Single Wall.....	78
6	IMPACT LOADING.....	84
6.1	16 th and 17 th Century Cannonballs.....	84
6.2	Hypothetical Impactor.....	90
7	CONCLUSIONS AND FUTURE WORK.....	94

LIST OF FIGURES

Figure 1. Map of Spain indicating the location of Granada.	3
Figure 2. The Alhambra (Schinz, 1984)	4
Figure 3. Map of the City of Granada and the Alhambra Fort with the works carried out in 1810 and 1811 (Garcia-Pulido, 2013).	4
Figure 4. Layout of the Alhambra, including the <i>Generalife</i> (adapted from López Díaz de la Guardia, 1961).	6
Figure 5. Plan of the <i>Alcazaba</i> with the <i>Torre de la Vela</i> highlighted in green (adapted from Pavón Maldonado, 1971).	7
Figure 6. The <i>Torre de la Vela</i> : (a) viewed from the East (Bermudez Lopez et al., 1992); (b) viewed from the North (Jebulon, 2012).	8
Figure 7. Bell and bell gable on the terrace of the <i>Torre de la Vela</i> (Chamoso G, 2009).	9
Figure 8. Isometric view of the <i>Torre de la Vela</i>	10
Figure 9. Bridge leading to the entrances of the <i>Torre de la Vela</i> (Vuoto, 2020).	10
Figure 10. Plans and cross sections of the <i>Torre de la Vela</i> by Gómez-Moreno Calera (2002).	11
Figure 11. Plans of the <i>Torre de la Vela</i> by López Bueno and Torres Balbás (1923).	11
Figure 12. Vaults on Levels 1 though 4: (left) isometrical view; (right) plan view.	13
Figure 13. Ruins of the <i>Torre Quebrada</i> (Villegas, 2012).	14
Figure 14. <i>Tapial calicostrado</i> wall shown in (a) cross section and (b) front view with various stages of erosion (de la Torre López et al., 1996).	15
Figure 15. Vault construction examples: (a) Barrel vault construction without centering (Lancaster, 2009) and (b) groin vault construction without centering (Villegas, 2012).	16
Figure 16. Cross-section of the <i>Torre de la Vela</i>	17
Figure 17. Types of geometry of the infill: (a) homogenous infill; (b) parallel partitions (Villegas, 2012).	18
Figure 18. Time-history and spatial evolution of a blast (adapted from Masi, 2020).	20
Figure 19. Idealized blast loading profile (adapted from Pereira, 2014).	21
Figure 20. Classifications of external explosions: free-air, air, and surface burst (adapted from Masi, 2020).	23
Figure 21. External blast wave loading on a structure (adapted from Cormie et al., 2011).	26
Figure 22. Classifications of internal explosions: fully vented, partially confined, and fully confined explosions (adapted from Masi, 2020).	30
Figure 23. Overpressure time-history response for a rectangular bunker with a sensor on the left (Chan & Klein, 1994).	30
Figure 24. Change of the reflection coefficient caused by the angle of incidence (UFC 3-340-01, 2002).	31
Figure 25. Simplification of the internal blast wave reflections (adapted from Cormie et al., 2011).	32
Figure 26. SDOF system subjected to an idealized blast load (adapted from Cormie et al., 2011).	33
Figure 27. Concrete beams subjected to impact loading: (a) local response; (b) global response (adapted from Fujikake et al., 2009).	35
Figure 28. Simplified models recommended by Eurocode for structures under impact loads (adapted from CEN, 2003).	36
Figure 29. Composition of black powder over the years.	37

Figure 30. Sixteenth-century Spanish artillery (Manucy, 1949): (a) a culverin (Class 1), (b) a cannon (Class 2), (c) a *pedrero* (Class 3), and (d) a mortar (Class 3) (Manucy, 1949).....39

Figure 31. Modelling strategies for masonry structures: (a) detailed micro-modelling; (b) simplified micro-modelling; (c) macro-modelling (Lourenço, 2008).41

Figure 32. Comparison between experimental, numerical (DEM), and numerical (FEM) results (Masi, 2020).42

Figure 33. CDP failure surface, represented in the deviatoric plane S1, S2, and S3 (Kmiecik & Kamiński, 2011).43

Figure 34. Stress-strain curves: (a) in tension; (b) in compression (Lubliner et al., 1989).43

Figure 35. Expected strain rates for different types of loading (Ngo et al., 2007).44

Figure 36. Schematic of the test setup used by Pereira (2014): (1) drop-weight tower; (2) additional masses; (3) hammer; (4) test specimen; (5) load cell; (6) acquisition system; (7) fast-cam video.45

Figure 37. Example of parts imported into Abaqus: (a) inner nave; (b) outer nave; and (c) floor.47

Figure 38. Boundary Conditions: (a) East façade; (b) South façade; (c) Bottom.47

Figure 39. Mesh of the *Torre de la Vela* model in Abaqus.48

Figure 40. Elements: (a) tetrahedron pyramidal element (C3D10); (b) hexagonal brick element (C3D8R) (ABAQUS, 2010).49

Figure 41. Assumed behaviour for the materials in: (a) Compression; (b) Tension (DIANA FEA BV, 2020).51

Figure 42. Compression and tension stress-strain extracted from Diana.52

Figure 43. Eigenmodes comparison between the Abaqus model (left) and the Diana model (right) provided by Vuoto (2020). The modes compared are: (a) Mode 2; (b) Mode 3; (c) Mode 4.54

Figure 44. Location of blast loading on the exterior of the *Torre de la Vela*.56

Figure 45. Pressure profiles acting on the *Torre de la Vela* for 110 kg TNT at 4 m.56

Figure 46. Displacement time history at the upper corners of the building in the North-South direction.57

Figure 47. Deformed shape time history.58

Figure 48. Tensile stress at 0.62 s: (a) Rammed earth exterior; (b) Brick masonry.59

Figure 49. Compressive stress at 0.62 s: (a) Rammed earth exterior; (b) Brick masonry.59

Figure 50. Time history of the displacement at the top of the entrance.60

Figure 51. Compressive stress at different instances of the displacement history at the top of the entrance opening.61

Figure 52. Tensile strain at 0.62 s: (a) exterior of the building; (b) interior of the building.62

Figure 53. Compressive strain at 0.62 s: (a) exterior of the building; (b) interior of the building.62

Figure 54. Damage in tension greater than 0.77.64

Figure 55. Boundary conditions on the south wall.65

Figure 56. Comparison between the displacement at the front façade upon blast loading: (a) whole building model; (b) front façade model with springs.65

Figure 57. Displacement in the direction of the blast: (a) single exterior wall; (b) whole building model.66

Figure 58. Tensile stresses in the front façade: (a) contact model; (b) whole building model.67

Figure 59. Compressive stresses in the front façade: (a) contact model; (b) whole building model.67

Figure 60. Tensile strains in the front façade: (a) contact model; (b) whole building model.68

Figure 61. Compressive strains in the front façade: (a) contact model; (b) whole building model.....68

Figure 62. Front façade using continuum element, where elements exceeding the damage threshold have been removed.....69

Figure 63. South façade of the simplified continuum model: (a) tensile stress; (b) compressive stress. .70

Figure 64. Simplified model of Level 2.....70

Figure 65. Zone locations for the interior blast.....71

Figure 66. Loading Profiles for: (a) Zone 1; (b) Zone 2; and (c) Zone 3.72

Figure 67. Excessive displacement on the wall.....73

Figure 68. Tensile stresses: (a) inner walls facing East; (b) inner walls facing West; (c) vaults; and (d) exterior north wall facing South.....74

Figure 69. Compressive stresses: (a) inner walls facing East; (b) inner walls facing West; (c) vaults; (d) exterior north wall facing South.....75

Figure 70. Tension strains: (a) inner walls facing East; (b) inner walls facing West; (c) vaults.....76

Figure 71. Compression strains: (a) inner walls facing East; (b) inner walls facing West; (c) vaults.....77

Figure 72. Time history of the damage to the interior walls of the building.....78

Figure 73. Mesh sizes: (a) 0.1 m; (b) 0.2 m; (c) 0.3 m.....79

Figure 74. Displacement at 0.06 s for different sized meshes: (a) 0.1 m; (b) 0.2 m; (c) 0.3 m.....80

Figure 75. Displacement at the centre of the wall over time.....80

Figure 76. Time history of the rotation of the wall for different mesh sizes.....81

Figure 77. Tensile damage at 0.06 s: (a) 0.1 m; (b) 0.2 m; (c) 0.3 m.....81

Figure 78. Damage index of the wall over time.82

Figure 79. Tension damage to wall Z1-S at 0.1 s: (a) 0.1 m mesh; (b) 0.1 m mesh with removed damaged elements; (c) 0.2 m mesh; (d) 0.2 m mesh with removed elements; (e) 0.3 m mesh; (f) 0.3 m mesh with removed elements.....83

Figure 80. Loading definition: (a) continuum model; (b) contact element model; (c) impactor.....85

Figure 81. Refined mesh around the location of impact.....85

Figure 82. Time history of compression stresses immediately after impact on the front of the wall: (a) continuum model; (b) contact model.86

Figure 83. Compression stresses in the back of the models after impact: (a) continuum model; (b) contact element model.....87

Figure 84. Time history of tensile stresses immediately after impact on the front of the wall: (a) continuum model; (b) contact model.....88

Figure 85. Tensile stresses in the back of the models after impact: (a) continuum model; (b) contact element model.....88

Figure 86. Displacement at the impacted node in the direction of the load.....89

Figure 87. Total energy of the output set.....89

Figure 88. Time history of compression stresses.....91

Figure 89. Tensile stresses in the wall caused by the impactor over time.....92

Figure 90. Time history of the diameter of the hole.....93

LIST OF TABLES

Table 1. Explosives and their charge factors, CF (Bangash & Bangash, 2006)	22
Table 2. Dimensions of powder barrels (Griffiths, 1856).....	38
Table 3. Experimental and calculated explosion energy, in kJ/g, for TNT and black powder (Basco et al., 2010).....	38
Table 4. Weights of Spanish cannons circa 1603 (Hall, 1952) and ("Cannon," 2021).....	39
Table 5. Ranges of Spanish cannons circa 1603 (Hall, 1952).	40
Table 6. Interaction properties.	46
Table 7. Unit system used in Abaqus.....	47
Table 8. Element sizes.....	48
Table 9. Material properties of the rammed earth, brick masonry, and infill used in the analysis of the <i>Torre de la Vela</i>	49
Table 10. Dynamic increase factors for the brick masonry, the rammed earth, and the infill under blast loading.....	50
Table 11. Updated material properties using DIFs.....	50
Table 12. Suggested parameters by the Abaqus User's Manual (Abdelmoneim Elamin Mohamad & Chen, 2016).	51
Table 13. Comparison between the expected mass from the AutoCAD model and the results from the Abaqus Model.	53
Table 14. Global modes for the <i>Torre de la Vela</i> obtained by eigenvalue analysis.....	53
Table 15. Damage levels for the failure volume index (Asteris et al., 2014).....	63
Table 16. Estimated damage level, damage index, and volume of failed elements.	64
Table 17. Total volume, volume of damaged elements, damage index, and damage level for different structural components.	78
Table 18. Properties of the impactor.	84
Table 19. Properties of the hypothetical impactor.....	90

GLOSSARY

A	Area
a_0	Speed of sound in the undisturbed atmosphere
C_D	Drag coefficient
C_r	Sound velocity in the reflected region
$C_{r\alpha}$	Reflection coefficient
d	Ductility Index
E	Young's Modulus
F_D	Drag force
$\mathbf{F}(t)^{ext}$	External force
$\mathbf{F}(t)^{int}$	Internal force
G	Dimension
G_{fc}	Compressive fracture energy
G_{ft}	Tensile fracture energy
i	Impulse
i_r	Normally reflected impulse
i_{rT}	Total specific impulse
i_s	Impulse of positive phase
i_{s-}	Impulse of negative phase
K	Spring constant
K_c	Ratio
\mathbf{M}	Lumped mass matrix
M	Mass of the structure
M_1, M_2	Partial mass of the structure
M_x	Mach number
P_o	Ambient pressure
P_r	Reflected pressure
P_{rT}	Total peak reflected pressure
P_{so}	Peak side-on overpressure
P_s	Overpressure
$p(t)$	Distributed impact load
Q_{TNT}	Mass specific energy of TNT
Q_x	Mass specific energy of given explosion
P_d	Dynamic pressure
$P_{d,max}$	Maximum dynamic pressure
R	Standoff distance
r_c	Charge radius
S	Dimension
T	Natural period of vibration
t	Time
t_a	Arrival time
t_{a1}	Arrival time on the front facade
t_{a2}	Arrival time of the blast wave at the top and side facades

t_{a3}	Arrival time of the blast wave at the rear facade
t_d	Positive phase duration
t_{d-}	Negative phase duration
t_{max}	Time of maximum dynamic deflection
t_r	Reverberation time
\ddot{u}	Accelerations
\dot{u}_s	Particle velocity behind wavefront
u	Vertical displacement
u_{max}	Maximum dynamic deflection
u_{st}	Static deflection
W	Charge mass
W_{TNT}	Equivalent charge mass
W_x	Mass of given charge
Z	Scaled distance
α	Incident angle
γ	Specific heat ratio
$\dot{\epsilon}$	Strain rate
ϵ_c	Eccentricity
μ_v	Viscosity Parameter
ν	Poisson's Ratio
π	Constant pi
ρ	Density
ρ_s	Density of air
σ_c	Compressive strength
σ_t	Tensile strength
ψ, Ψ	Functions of frequency, time, and period
Ψ'	Dilation angle
ω	Natural circular frequency of vibration

CHAPTER 1

1 INTRODUCTION

The Alhambra is a UNESCO World Heritage Site located in the South of Spain, in the city of Granada. This site is a testimony to Muslim Spain between the 13th and 15th centuries. This palatine city is the only preserved example remaining from the Islamic period in the Iberian Peninsula. The architecture and decorative elements in the Alhambra are a masterpiece of creative genius, a unique testimony to the cultural tradition of its period and represents a significant stage in the history of humankind. This work focuses on the *Torre de la Vela*, a rammed earth tower in the defensive area named the *Alcazaba* located within the Alhambra. The tower has previously been damaged by lightning and gunpowder factory explosions.

The main objective of this thesis is to evaluate the structural response of the *Torre de la Vela* under blast and impact loading. In addition to the main objective, this thesis aims to discuss the different methods to characterize damage and the effects of mesh size on that damage. The work also aims to discuss the difference between macro-modelling versus micro-macro modelling in regions where higher displacement is expected. This thesis presents seven chapters, which are described as follows:

Chapter 1 introduces the case study, the objectives, and the organizational structure of the document.

Chapter 2 presents the *Torre de la Vela* and its context within the Alhambra, including its history, geographical location, geometry, construction techniques, and previous interventions.

Chapter 3 encompasses a literature review of the available concepts and theories related to blast and impact loading, including the definition and classification of loads, and a review of military weapons used in 16th and 17th-century Spain.

Chapter 4 presents a literature review of the available numerical models for masonry structures under blast loading, including the available solvers, material models, and material behaviour at high strain rates. The modelling of the case study including geometry, boundary conditions, mesh creating, and definition of material properties, and effect of high strain rates are discussed. Additionally, an eigenvalue analysis is conducted to calibrate the current model against an existing model.

Chapter 5 presents the numerical analysis of the *Torre de la Vela* under specified blast loading conditions. The global and local response of the tower under external and internal blast loading will be presented. The local response of individual structural members will also be presented. A comparison between macro-modelling and modelling using contact elements will be made. The effect of the mesh size on the damage will also be investigated.

Chapter 6 presents the local response of a section of the *Torre de la Vela* under impact loading by a 16th-century cannonball. The section of the tower using macro-modelling and contact elements will be presented. The damage caused by a hypothetical impactor on the tower will also be presented.

Chapter 7 presents the conclusions and recommendations for future work.

CHAPTER 2

2 THE ALHAMBRA AND THE *TORRE DE LA VELA*

The Alhambra is located in the South of Spain, in the city of Granada (Figure 1). The site stands on the al-Sabika hill, beside the river Darro. The Alhambra is composed of three main areas: the military zone (or *Alcazaba*), the palatine (or imperial) city, and the medina (or the residential, administrative, and religious area). The word Alhambra is derived from the Arabic work "al-Hamra", meaning "the red one", likely because of the colour of the rammed earth it is constructed from.

Alhambra (Figure 2) is a palatine city, the only preserved example of its kind from the Islamic period in the Iberian Peninsula. It is also the best example of Nasrid (the last Muslim dynasty in the Iberian Peninsula) due to its architecture and decorate elements. In fact, the Alhambra was listed as a UNESCO World Heritage site in 1984 under three criteria: it is a masterpiece of creative genius, a unique testimony to cultural tradition, and an outstanding architectural ensemble showing a significant stage in human history.



Figure 1. Map of Spain indicating the location of Granada.

Granada is located at the end of an extensive and highly cultivated plain. It is bounded by the mountains of Sierra Nevada, 900 m above the sea level. The rivers Darro and Genil are nearby and provide irrigation to the city. The Alhambra fortress is located to the West of the city of Granada, at the top of the al-Sabika hill, 760 m in height. This hill is the last bastion of the Sierra Nevada and faces the districts of Albaicin and Sacromonte in the city of Granada.



Figure 2. The Alhambra (Schinz, 1984)

The location of the Alhambra is of significant importance with respect to its military power. The natural barriers such as the site's location on a hill without trees, the mountains of the Sierra Nevada, and the surrounding valleys and depressions make it nearly impossible for the Alhambra to suffer an assault from an outside army. In addition to the natural barriers, the features and structures surrounding the Alhambra, such as the *Generalife*, the *Puerta de las Granadas* (Gate of the Pomegranates), the *Torre Bermejas* (Bermejas Tower), and the *Puerta de la Justicia* (Gate of Justice) (Figure 3), all act as barriers that protect and isolate the Alhambra from any attacks. During the Napoleonic era, fortifications were added around the Alhambra to improve its defensive position. The map in Figure 3 shows the militarized area of the Alhambra, spreading from St Helena to *Las Barreras* (the Barriers) hills, identified with red ellipses (Garcia-Pulido, 2013).

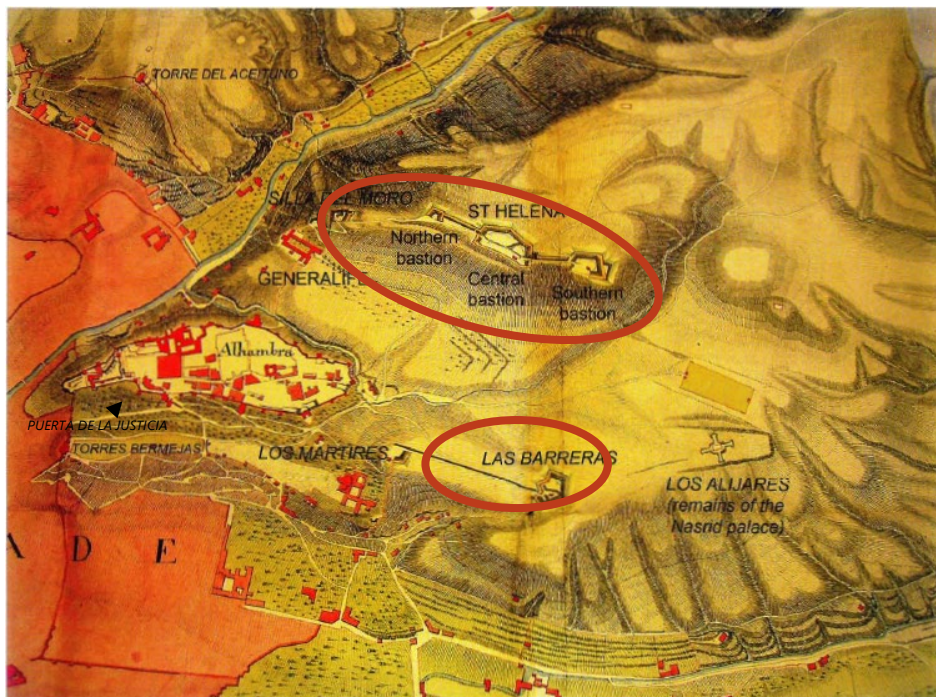


Figure 3. Map of the City of Granada and the Alhambra Fort with the works carried out in 1810 and 1811 (Garcia-Pulido, 2013).

2.1 History of the Alhambra

The construction of the Alhambra complex began during the Nasrid dynasty between the years 1238–1273. During the construction of the Alhambra by Muhammad I, the *Alcazaba* was constructed in the South of the hill with the intention of housing the royal guard, and the medina (or royal residences) were built in the North to house the various workers in the citadel. The Alhambra was the residence and power central to sultans, who made Granada the capital of the so-called *Reino de Granada* (Kingdom of Granada). The *Torre de la Vela* (Tower of the Bell) was also used as a feudal residence during this period (Jaquin, 2008). This period also saw a significant shift in the appearance of the Alhambra: it evolved from being a place of military architecture to a place of palace architecture. However, the first reference to the Alhambra is believed to be during the battles between the Arabs and the Muladies (Christians who adopted Islam during the Moorish occupation), which occurred during the rule of the Emir of al-Andalus c. 888–912 (Dodds et al., 1992).

The Alhambra was renovated and extended during the 300 years of the al-Andalus rule or Muslim Kingdom. Between 1273 and 1302, the *Puerta del Vino* (Wine Gate) and the *Torre de los Picos* (Tower of the Spikes) in the Alhambra were constructed under the rule of Muhammad II. In 1348, walls were constructed around most of the Alhambra under the orders of Yusuf I. This period also saw additions of multiple towers such as the *Torre de los Siete Suelos* (Tower of Seven Floors), the *Puerta de la Justicia* (Gate of Justice), the *Torre del Agua* (Water Tower), and the *Torre de Balthasar de la Cruz* (Tower of Balthasar of the Cross). The year 1408 led to the construction of the Palace of Yusuf III and the Partial Gardens, and the year 1445 saw the construction of the *Torre de las Infantas* (Tower of the Princesses) and the expansion of the *Torre de los Picos* (Tower of the Spikes) (Jaquin, 2008).

After the Christian reconquest of Spain on January 2, 1492, the Alhambra changed occupancy. During this time, the Alhambra was transformed into a monumental complex and became the Royal house of the Spanish Kingdom. Thus, work on the building continued and the infrastructure was adapted to its new uses. Single buildings were divided into multiple buildings and were redistributed among nobles. The Christian conquest also saw the introduction of new emblems and symbols (Dodds et al., 1992).

After the conquest by Ferdinand II and Isabella I, the Alhambra was occupied by their grandchild, Emperor Charles V (1516–1556). He rebuilt multiple portions of the Alhambra in the Renaissance style and destroyed other portions of the complex to build an Italianate palace (Britannica, 2019).

Later, this complex had many other occupants such as Napoleonic troops, Spanish Romany residents, war prisoners, and travelling artists (Eggleton, 2012). Napoleon's occupation of the Alhambra during the War of Independence until 1812 led to the destruction of some parts of the walls (Jaquin, 2008), and also to the destruction of some of the towers in the Alhambra by means of explosives (Britannica, 2019).

Eventually, there was a desire to repair and upkeep the Alhambra. Requests for money to upkeep the building were submitted to the Spanish government, some of which by the writer Washington Irving who resided in the Alhambra starting in 1829. In 1830, Ferdinand VII dedicated a set sum of money for the upkeep of the buildings in the Alhambra. Following the revolution of 1868, the legal status of the Alhambra marked an important change. The state transferred the legal jurisdiction of the Alhambra to

itself instead of the crown. The entire complex of the Alhambra was declared a national monument in 1870. The maintenance of the Alhambra was given a special commission in 1905, which was replaced by a *Patronato* (patronage) in the *Dirección General de Bellas Artes del Ministerio de Instrucción Pública* (Directorate General of Fine Arts of the Ministry of Public Instruction) in 1913. Between 1944 and 1985, a new *Patronato* (patronage) was created which was dependent on the Ministry of Culture. In December 1985, the *Patronato de la Alhambra y Generalife* (Board of Trustees of the Alhambra and *Generalife*) was assigned as an independent body which is now responsible for the monumental site (Dodds et al., 1992).

2.2 Layout of the Alhambra and the Alcazaba

The Alhambra has three principal areas within its walls: the *Alcazaba*, which is primarily reserved for military use; the palace and its surroundings, which functions as a royal residence with up to seven distinct palaces; and the *medina*, which is a residential and artisan's city, where administrative and commercial activities take place for the royal court (Figure 4). The *medina*, contoured in the dashed blue line in Figure 4, is located in the southern portion of the complex, while the palaces (highlighted in blue in Figure 4) are in the northern part of the complex. One palace, Palace de Carlos V, is located inside the *medina*. Despite being outside the city walls, the *Generalife* is typically included in the description of the Alhambra (highlighted in green in Figure 4). The *Generalife*, separated and located to the east of the Alhambra, is a semiurban, semirural residence with palaces and terraced gardens. These gardens served as pasture for the livestock.

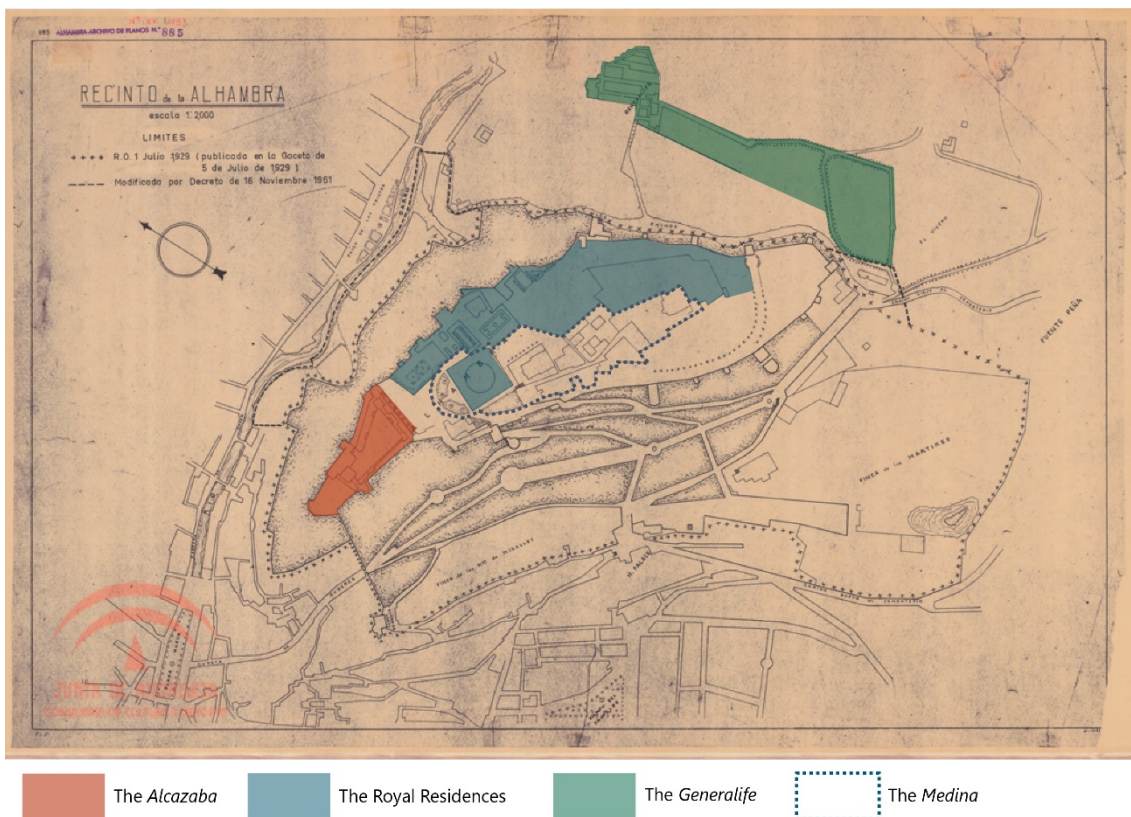


Figure 4. Layout of the Alhambra, including the *Generalife* (adapted from López Díaz de la Guardia, 1961).

The *Alcazaba* (Figure 5) is the military area of the Alhambra, situated on the West of the al-Sabika hill, which is also the hill's highest point. On its North side, the *Alcazaba's* maximum length is 100 m, and along the external wall facing the palaces it measures 74 m in length. Between the East and West sides, the *Alcazaba's* enclosure gradually narrows, giving it an irregular quadrilateral shape. An artillery bastion named the *Revellín* was added to the West of *Torre de la Vela* during the 15th century by the Nasrids. This bastion served to station and store artillery during this era.

Most other medieval fortresses typically had an open space without any buildings, and only had tents or shelters that were quick to dismantle. However, the *Alcazaba* is unlike these other medieval fortresses; its *Plaza de Armas* (Barrack Square) is occupied by many buildings. In particular, the military quarters, or *Barrio Castrense*, consisted of seventeen small houses for the elite guard and their families. These houses occupied the north part of the military quarters and was distributed in the characteristic Islamic urban pattern, joined and separated by narrow corridors and alleyways. The southern half of the military quarters was occupied by barracks laid out in a regular pattern. A water cistern and a bath for military use are located to the west of the urban area. It also appears as though the importance of the buildings increase as they approach the *Torre de la Vela* (Dodds et al., 1992). The *Torre del Homenaje* (the Keep), otherwise known as the command post for intelligence and strategy, is located at the northwest of the *Alcazaba* complex. This positioning allows for the best view of the surrounding terrain before and during battles.

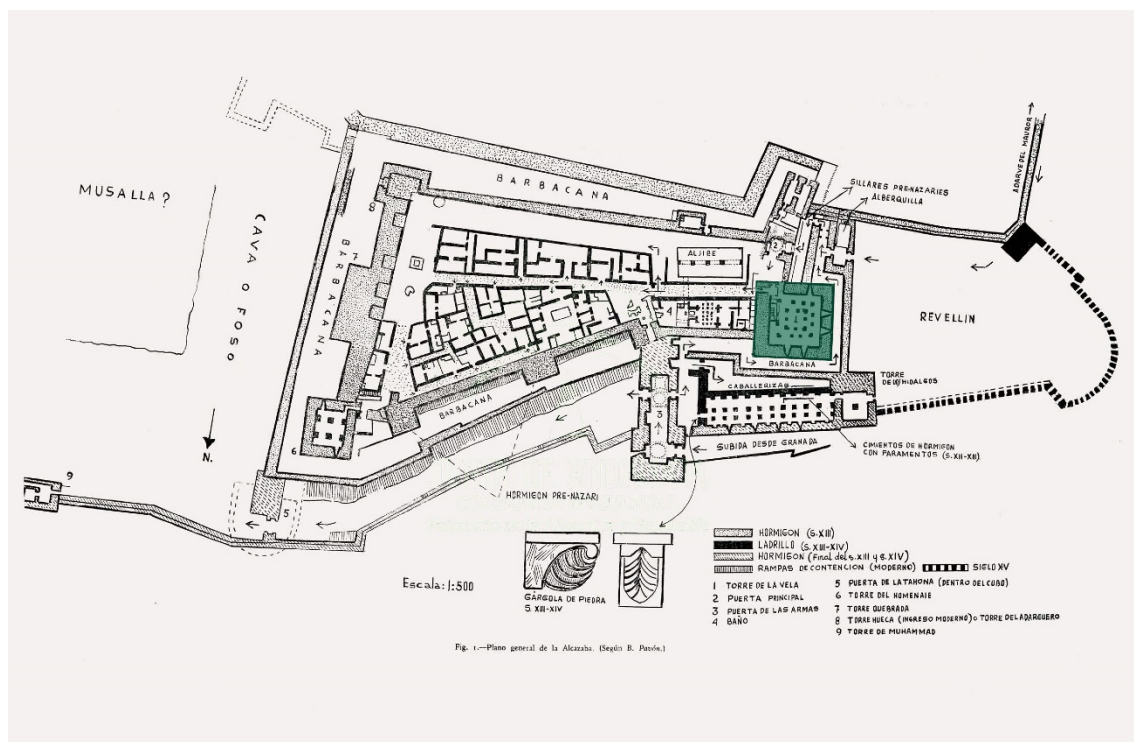


Figure 5. Plan of the *Alcazaba* with the *Torre de la Vela* highlighted in green (adapted from Pavón Maldonado, 1971).

2.3 The *Torre de la Vela*

The *Torre de la Vela* was the first structure in the *Alcazaba* to be constructed. It was initiated in 1238 by the Sultanate of Muhammad I. Even during the early states of its construction, the tower could be used as a watchtower to defend the city. Over the years, the tower has undergone numerous changes: some by its change in occupancy, and others related to modern-day conservation works. These modern-day interventions are evident due to the stark contrast between the original rammed earth construction and the brick masonry portions (Figure 6). After several different names, it was named *Torre de la Vela*, after the Christian conquest, because of the name of the first bell that was rung in the tower, called "La Vela." This bell was placed in the tower after the Christians conquered the city in 1492 to announce their victory to all. The word "Vela" also means "lookout" because this tower was also used as a watchtower. Some traumatic events have marked the *Torre de la Vela* over the years. In 1522 and 1821, the tower and the complex as a whole suffered an earthquake. In 1590, a gunpowder factory located directly below the tower exploded, leaving the tower significantly damaged. In 1882, the tower was struck by lightning (Jaquin, 2008).

The bell gable, and its bell on the west side of the terrace, is one of the character-defining elements of the tower (Figure 7). Originally located in the north-west corner until 1840, the tower's first bell was donated by the Catholic Monarchs. Since this period, the bell has been replaced numerous times, the first of which occurred in 1569, and the last replacement having occurred in 1773. This last replacement, cast by José Lorenzo Carmona, is the current bell that still rings today. The bell gable itself had to be rebuilt in 1882 following the aforementioned lightning strike. Previously, the bell was an important marker of time as it indicated the change of guard duty of the Alhambra's garrison. It also indicated to the farmers in the valley the hours to water and tend to their fields. Finally, the bell was also paramount in indicating danger to the citizens of Granada. Currently, the bell is rung only for ceremonial purposes. On January 2nd, the bell can be rung by anyone as this day commemorates the surrender of Granada to the Catholics. The bell is also rung on Easter and on Spain's National Day. This tradition is one of the intangible values of the *Torre de la Vela* which still exists today.

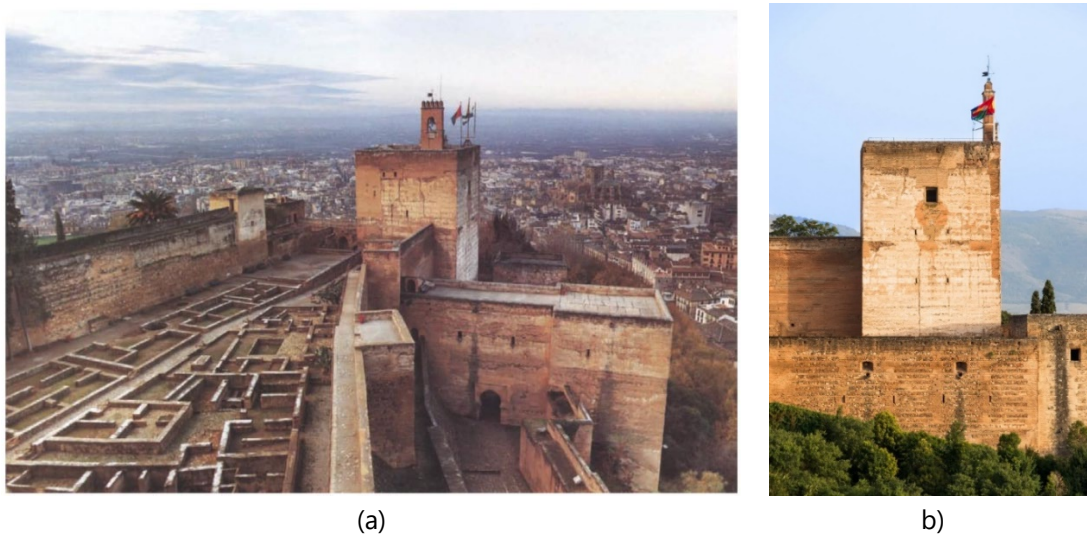


Figure 6. The *Torre de la Vela*: (a) viewed from the East (Bermudez Lopez et al., 1992); (b) viewed from the North (Jebulon, 2012).



Figure 7. Bell and bell gable on the terrace of the *Torre de la Vela* (Chamoso G, 2009).

2.3.1 Plans/Geometry

The *Torre de la Vela*, being the highest tower in the Alhambra, measures 26.8 m in height. Its square plan measures 16.0 m on either side (Figure 8). The tower is four stories in height, where the thickness of the walls decreases with each increasing storey (Figure 10). Two entrances exist in the *Torre de la Vela*. The main entrance to the building is located on the second floor of the tower, on the south side. This entrance is tortuous and does not allow for straight access to the building, making it good for military defence. Another entrance is located on the south side of the third floor. The staircase, which is present on Levels 2, 3, and 4, is located in the south-east corner of the building, and is isolated from the building by a mortar wall. Almost all the arches in the *Torre de la Vela* are semicircular, but the central voussoir converges to a point lower than the centre of the curve, making these arches identical to the Moorish arch. On the exterior of the building, the *Torre de la Vela* is connected to various other elements in the *Alcazaba*. The *Alcazaba* wall is connected on the building's east side, while a bridge is directly adjacent to the building's south side (Figure 9). The 3rd floor entrance is located at the top of this bridge, while the 2nd floor entrance is located underneath. The south-east corner of the building is below ground, or 11.3 m on the south side and 12.3 m on the east side. The depth of the underground portion is 7.8 m, meaning the entire Level 1 is effectively below ground.

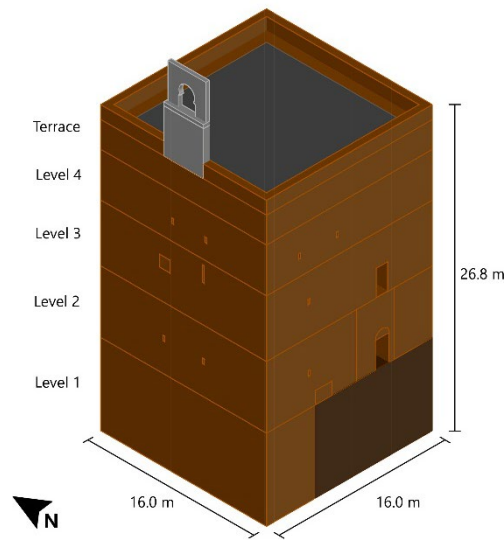


Figure 8. Isometric view of the *Torre de la Vela*.



Figure 9. Bridge leading to the entrances of the *Torre de la Vela* (Vuoto, 2020).

The walls on the second floor are vertically in-line with those of the upper floors. However, the ground floor does not have a wall that is vertically aligned with the rest of the walls from the upper floors. Based on this arrangement, it appears as though the ground floor was initially not intended to account for the upper floors. Due to this, the addition of relieving arches was implemented but was insufficient to prevent the deformation of the vaults, and cracking and crushing in the pillars. This is a likely explanation for the arches and wall added in the central room of Level 1 (Vuoto, 2020). A detailed description of the tower's features is described below, based on Pavón Maldonado (1971) and Gómez-Moreno (1907). Additionally, historical records of the plans and cross-sections of the tower are available from two sources. The plans and cross-section in Figure 10 date from 1907 by Gomez Moreno, and those in Figure 11 date from 1923 and 1936, being created by Lopez Bueno for the architect Leopoldo Torres Balbas. A 3D model using laser scanning technology was also available for the description of the tower, provided by Vuoto and Ortega.

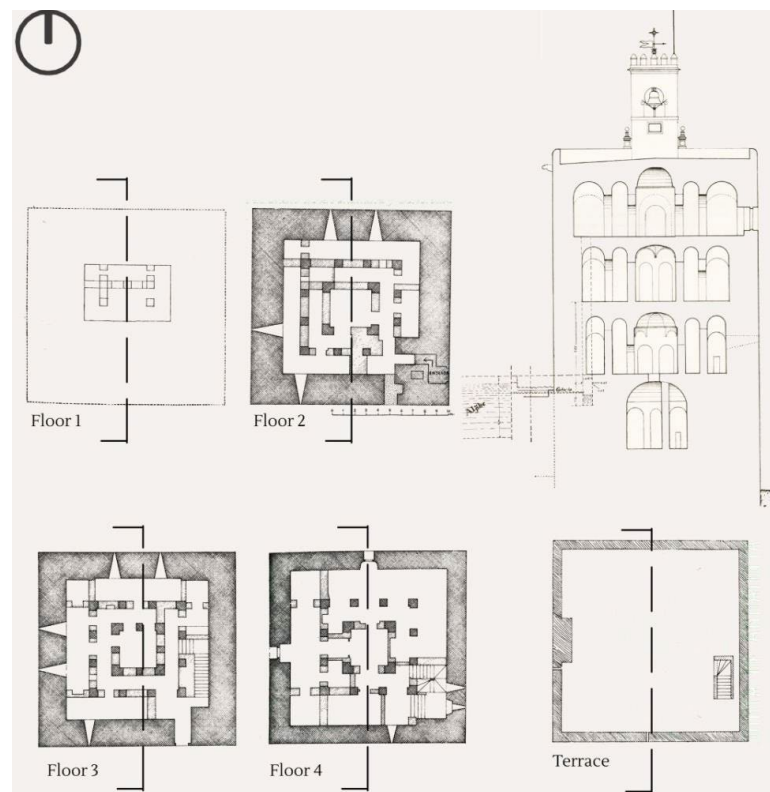


Figure 10. Plans and cross sections of the *Torre de la Vela* by Gómez-Moreno Calera (2002).

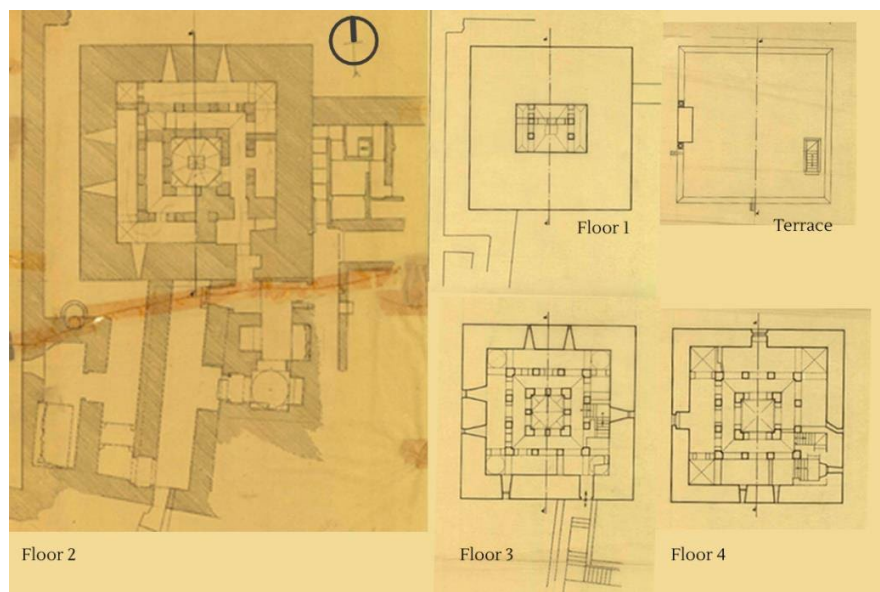


Figure 11. Plans of the *Torre de la Vela* by López Bueno and Torres Balbás (1923).

The ground floor of the tower is composed of a rectangular plan, wider in the East-West direction than the North-South, with a single nave dungeon. This floor can only be reached from the second floor by means of ropes or ladders, likely a method preventing risk of prisoners escaping (Gómez-Moreno Martinez, 1907). Additionally, the height of the floor on this level is not at the same level as the base of the tower. Rather, the base of the floor sits on a floor of rammed earth 1.8 m higher than the tower's

base. Three vaulted ceilings are present on the ground floor: one in the centre, and two on either side (Figure 12). All the vaults on this floor consists of trough vaults. Two narrow arches divide the centre vault from east to west. The smaller vaults are separated from the central vault by a series of arches: a larger filled arch is on the north side of the division and two smaller arches are to the south of this division. One of the small arches on the west side has been filled to form a wall. The outer wall on the ground floor has a width of 4.6 m. Two pointed arches are also seen in this storey, which is a distinct feature in the Alhambra.

Unlike Level 1, the upper three levels share many more similarities in plan. A central room measuring 3.1 m on each of the four sides can be found on Levels 2, 3, and 4. On Level 2 and Level 4, this central room is surrounded by four arches: one on either side of the square. On Level 3, the central room is connected to the outer nave by 8 arches: two on each side of the square room. Levels 2, 3, and 4 all have a set of arches which separate the interior corridor from the exterior corridor. On all three, this separation is created by a total of 12 arches, with 3 on each side forming a square. As the thickness of the exterior wall decreases with the increased level, the width of the exterior corridor increases (Figure 12).

Similar to the layout of the arches, the upper three floor share similarities in the types of vaults as well (Figure 12). The interior and exterior corridors of Levels 2, 3, and 4 all have ceilings composed of barrel vaults. It is when observing the central vaults and corner vaults that differences are evident between these three floors. On Level 2, the vault in the central room is a large trough vault, consisting of eight panels sitting on groin vault-shaped pendentives. The central vault on Level 3 is a groin vault, which sits on four angular semi-vaults. The ceiling of the central room on Level 4 is a large trough vault but is formed of four panels. The vaults at the four exterior and interior corners of Levels 2 and 4 are groin vault. On Level 3, groin vaults are present at the interior corners, but sail vaults are used for the exterior corners.

The amount, size, and position of the window openings vary on each floor of the tower. There are no windows at all on the ground floor, likely due to the use of this floor as a prison. A few small window openings exist on Level 2, in addition to the opening for the entrance on the South façade. Pairs of windows can be found on the North and West façades of the building, and another single window can be found on the South façade. With respect to openings on Level 3, a large door-like opening can be found on the South façade of the building, directly above the building entrance. Another small window is also located on the South façade. The West façade has two windows: one large and one long and narrow. The North façade has two small windows which are vertically aligned with the floor below. The East façade has a single small window in the centre of the façade. On Level 4, a large window opening can be found on the North and East sides of the building. The South and West sides of the building have a pair of small windows each.

The terrace at the top of the tower is surrounded by a low parapet on all of its sides. The bell gable, which was mentioned previously, is located on the centre of the west side of the tower. The stairwell leading up to the terrace is also located on the south-east corner of the plan.

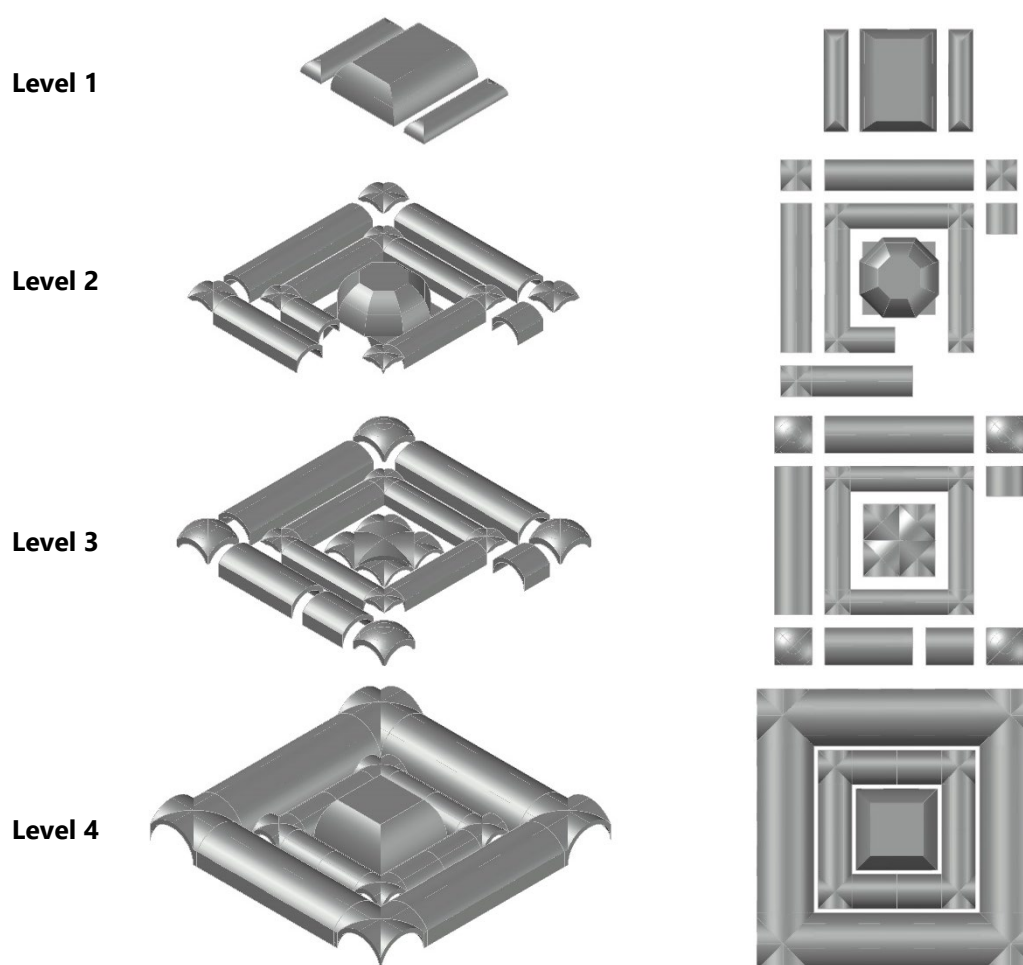


Figure 12. Vaults on Levels 1 though 4: (left) isometrical view; (right) plan view.

2.3.2 Past Interventions and Construction Techniques

In the Alhambra, traditional masonry materials and techniques were employed. The towers, gates, and walls of the fortified city have mostly been constructed from rammed earth and brick masonry. As the external walls of the towers were typically constructed of rammed earth, the visible locations of brick masonry indicate locations of possible reconstructed portions. Local subsoil was the base of the materials for both the rammed earth walls and the mortar used.

The traditional method of construction of rammed earth walls can be seen throughout the complex of the Alhambra. The term rammed earth is a blanket term for the construction technique employed regardless of the type of material. This technique traces back to the Roman tradition of limestone cement and rammed earth and is typical in Spanish-Muslim Grenadine architecture (de la Torre López et al., 1996). Various typologies of earthen construction exist in the Alhambra, but only the *tapial calicostrado* is found in the *Torre de la Vela* (de la Torre López et al., 1996).

With respect to past interventions of the *Torre de la Vela*, some parts of the building have been rebuilt. Additionally, arches on the second and third floors have been filled over the years, which resulted in the loss of the original configuration of the building. However, as updated drawings were not available,

precise locations of reconstructed portions and closed openings could not be located. When the top floor of the tower was converted into an apartment, a modern staircase was added to facilitate access.

In the *Torre de la Vela*, two main construction techniques can be found, which are: a) *Tapial calicostrado*; b) Brick masonry; and c) Infill for the horizontal elements. These construction techniques will be further detailed below.

Tapial calicostrado

The exterior of the *Torre de la Vela* is constructed of *tapial calicostrado*, although some areas which have been reconstructed can be seen in brick. The method of construction of the *tapial calicostrado* is very similar to traditional rammed earth masonry. Formwork is obtained by placing two vertical wood planks in parallel and joining them by wooden crossbeams. Typically, the interior and exterior vertical elements were tied together at the top with ropes such that the material did not cause the formwork to open. Different thickness layers of material were packed into the completed formwork using a heavy rammer. The formwork was removed once it was filled, and the construction continued until the selected height was reached. When openings were required, splayed wooden lintels were placed during the erection of the wall. Lintels on the interior and exterior of the walls can be found in many openings (de la Torre López et al., 1996).

Though the walls of the *Torre de la Vela* are very thick, no indication exists to consider these walls as having multiple leaves. This assumption can be made by observing the ruins of the *Torre Quebrada* (Broken Tower)—a ruined tower in the *Alcazaba*. As visible from the top-left portion of Figure 13, the external walls are continuous in their thickness (Gómez-Moreno Calera, 2002).



Figure 13. Ruins of the *Torre Quebrada* (Villegas, 2012).

It should be noted that the rammed earthen walls seen in the Alhambra are not constructed of a homogenous material. Instead, layers of earth richer in clay and richer in lime were placed in an alternating method into the formwork. The layers with lime were placed in the exterior part of the wall, in the form of wedges, which can be seen in Figure 14. Thus, on the exterior surface of the wall, the

layer of lime forms a homogenous surface. Due to the waterproof properties of this lime-earth mixture, the exterior of the wall did not have to be plastered. When the wall becomes eroded, the use of the layers becomes more evident. However, research into the mineralogical composition of the wall shows there is little difference between the materials in the same wall (de la Torre López et al., 1996). As no detailed study has been made on this phenomenon for the *Torre de la Vela*, it is assumed the walls are similar to those found in the rest of the Alhambra. A more quantitative description of the physical and mineralogical composition of the *tapial calicostrado* can be seen in literature (de la Torre López et al., 1996).

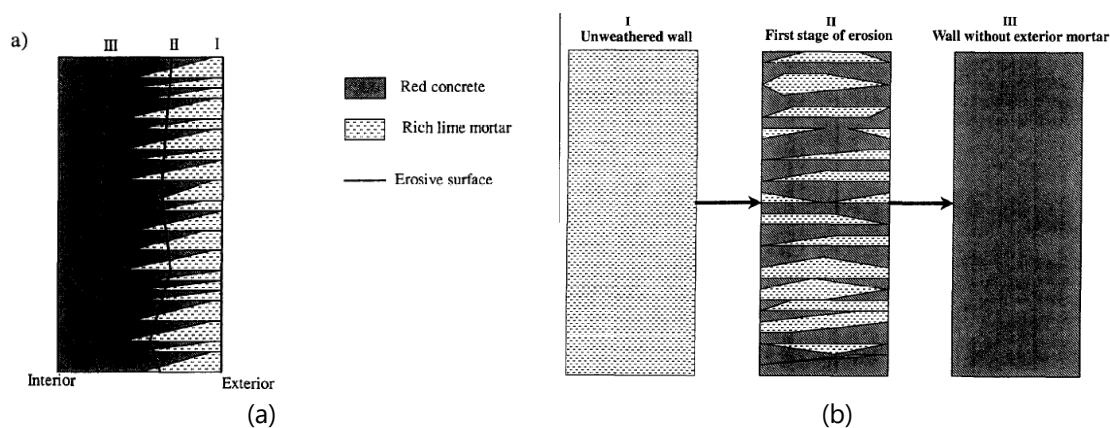


Figure 14. *Tapial calicostrado* wall shown in (a) cross section and (b) front view with various stages of erosion (de la Torre López et al., 1996).

There are many advantages to the use of the *tapial calicostrado* system (de la Torre López et al., 1996): a) when compared to walls which only used lime conglomerate, the use of the *tapial calicostrado* saves a large amount of material resources without compromising the strength of the wall. This is particularly important due to the massive thickness for defensive structures of this era; b) exterior coating such as plaster was not required due to the properties of the exterior material. In addition, the wedge shape of the lime material inside the wall significantly improves the friction, making the wall more durable; c) when comparing this construction system to traditional rammed earth with external plaster, there is significantly less weathering and there are less erosion processes, making the *tapial calicostrado* much better preserved.

Brick Masonry

Bricks are typically used inside the towers of the Alhambra as the primary construction material for pillars, arches, vaults, and staircases. Bricks are also used when a more adequate structural behaviour is required and when a decorative element is added. Bricks are often plastered or painted to imitate a regular pattern (Gómez-Moreno Calera, 2002).

As with other towers in the Alhambra, the interior structural elements of the *Torre de la Vela*, such as pillars, arches, and vaults, have been built using brick masonry. This masonry can be characterized as well-baked irregular clay bricks, and have mortar joints of up to 3 cm in thickness. With respect to the brick units, those used in the inner structure of the *Torre de la Vela* have dimensions of 29 x 14 x 5–6 cm and are part of the Almohad brick typology (Pavón Maldonado, 1971). Different bond patterns

were used for the brick depending on the location of the bricks and the geometry of the element. Those patterns included the herringbone bond, the header bond, and the traditional Hispano-Muslim arrangement named of stretcher and header bond.

Mortars having a reddish colour date to the Nasrid period. The mortars used to assemble the brick units are very similar to rammed earth and have thick joints between the units. The composition of the mortar in the interior elements is made of earth, clay, and lime. However, the mortars used in the vaults can be characterized as a hard gypsum mortar (Gómez-Moreno Martínez, 1907). The decorative plaster elements were made of lime mortar. Gypsum mortars can be found in the arches and vaults, as this type of mortar allows for the construction of arches and vaults without the use of centering. The construction of the vaults without the use of centering can be seen in Figure 15.

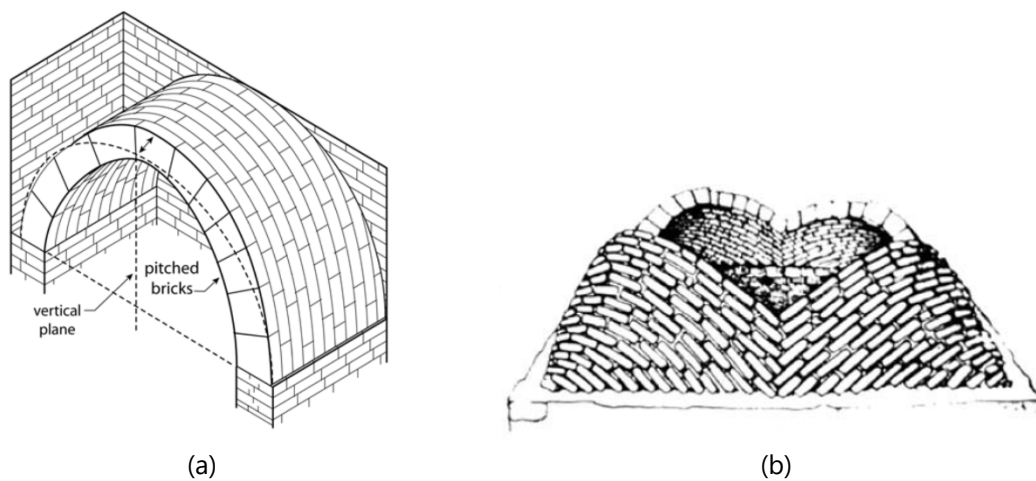


Figure 15. Vault construction examples: (a) Barrel vault construction without centering (Lancaster, 2009) and (b) groin vault construction without centering (Villegas, 2012).

It was not possible to determine if the vertical elements in the interior of the tower were continuous with respect to the other floors based on the drawings presented in Section 2.3.1. By looking at the ruins of the *Torre Quebrada* (Broken Tower) (Figure 13), some vertical elements are aligned from one storey to another. However, this statement is not true of all the vertical elements, as some of the vertical elements on the second level are in line vertically with the centre of the arches of the level below. Due to the inability to access the *Torre de la Vela* to conduct a more conclusive determination of the construction techniques of the interior core, as well as the lack of available information, the vertical elements in the *Torre de la Vela* can be assumed as continuous (Figure 16), according to Vuoto (2020).

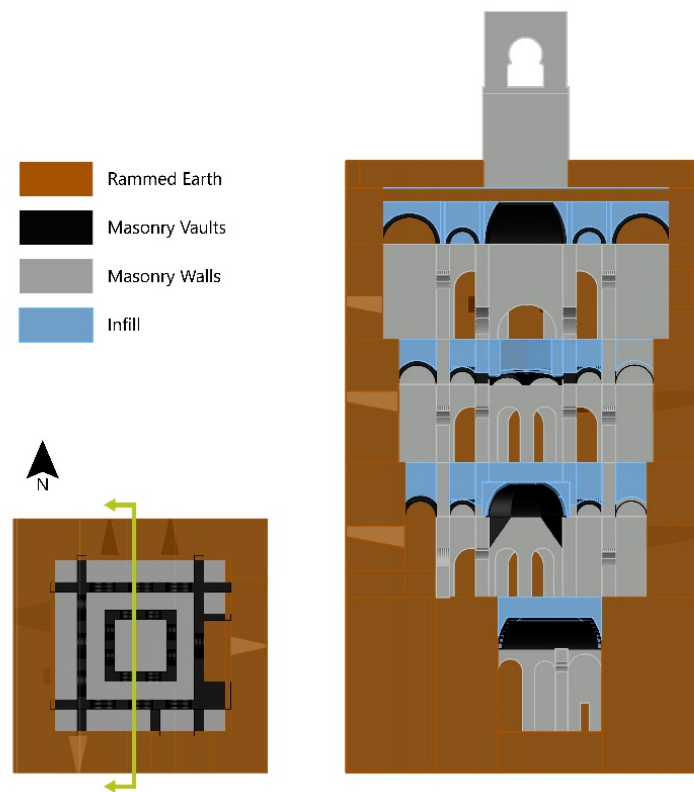


Figure 16. Cross-section of the *Torre de la Vela*.

Horizontal Elements

As seen previously in Section 2.3.1, the *Torre de la Vela* was constructed of various types of vaults and domes. For this reason, the construction of a horizontal floor directly above these vaults would have been challenging. Two hypotheses exist for the type and geometry of the infill used to create these horizontal elements.

The first hypothesis is based on the images of the ruins of the *Torre Quebrada* (Broken Tower) (Figure 13) where the infill seems to be homogenous until the upper floor. Thus, the assumption is that a homogenous infill with mortar and coarse aggregates was used on all the floors until the upper floor (Figure 17a). Based on a study by the Laboratory of Geotechnics of CEDEX (*Centro de Estudios y Experimentación de Obras Públicas*), which characterized the *Torre de Comares* (Comares Tower), the infill of the tower is composed of material very similar to the *tapial calicostrado* and does not use elements to lighten the load of the floors (González Limón & Casas Gómez, 1997).

The second hypothesis is based on the documented construction techniques of floor systems in the Hispano-Muslim period. This technique consists of creating parallel partitions on top of the vaults in order to create a single-direction system of parallel walls (Figure 17b). These were then covered with small barrel vaults made of bricks. The infill was then placed on top of this system. This technique lightens the load on the dome system (Villegas, 2012).

In the numerical model of the *Torre de la Vela*, the *tapial calicostrado* material will be assumed for the infill, based on the first hypothesis. The geometry of the infill in the model will assume the partitions stated in the second hypothesis.

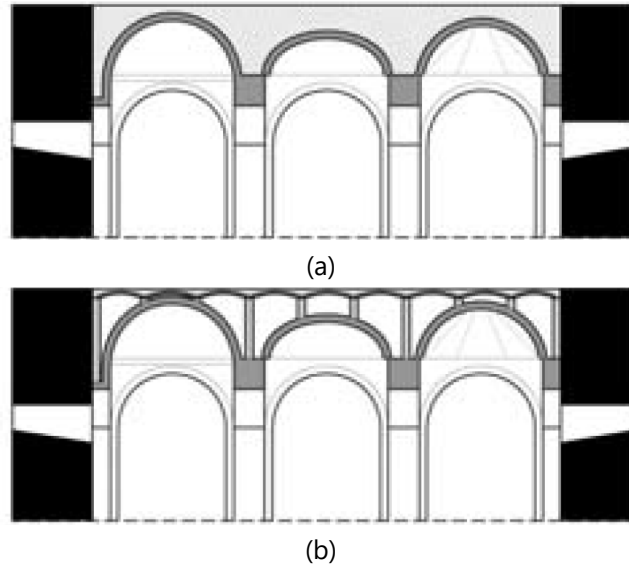


Figure 17. Types of geometry of the infill: (a) homogenous infill; (b) parallel partitions (Villegas, 2012).

CHAPTER 3

3 STATE OF THE ART: LOADING AND ANALYSIS

The vulnerability of masonry envelopes under blast loading is critical due to the potential loss of lives. Blasts near or inside a building can damage and destroy parts of the building and can produce both local and global responses related to different failure modes within structural members. Particularly, the out-of-plane response of masonry under dynamic loading is critical due to the risk this poses on the loss of life. Under dynamic loading conditions, materials can have different behaviour when compared with quasistatic conditions. Despite this, static material properties are often assumed on research work regarding the structural response and damage under impact and blast loading, which can lead to an inaccurate prediction of the damage. Few numerical studies have been conducted regarding the effect of blasts and impact on masonry structures. Thus, it is important to better understand the behaviour of masonry structures under these conditions.

This chapter summarizes the available concepts and theories related to blast and impact loading. Regarding blast loading, this chapter presents definitions of explosions, blast waves, and their interaction with the structure. With respect to impact, this chapter introduces the definition and the classification of loads. Simplifications and assumptions with regards to the analysis, the loading, and the material behaviour under blast and impact loading are also presented. Finally, a brief literature review on the military weapons used in the 17th century is also presented.

3.1 Blast Loading

Explosions or blasts are defined as sudden releases of energy, where gas expands and increases in volume rapidly. This rapid expansion of gasses can be caused by either physical or mechanical change (Ngo et al., 2007). The nature of explosions can be classified in the following three categories:

- Physical: energy is released from e.g. catastrophic failure of a cylinder of compressed air, when two liquids are mixed at different temperatures, or during volcanic eruptions.
- Chemical: energy is released from the rapid oxidation of carbon and hydrogen atoms.
- Nuclear: energy is released from the formation of different atomic nuclei and the redistribution of the protons and neutrons within the interacting nuclei.

During an explosion, a layer of compressed air (also defined as the blast wave) is formed in front of the gas volume with the most energy released by the explosion. Consequently, the pressure of the blast wave—known as the side-on overpressure—increases to a pressure above the standard atmospheric pressure. The term overpressure is used to define a differential pressure, relative to the ambient pressure, P_o . The peak side-on overpressure, P_{so} , relates to the free air pressure waves which have yet to encounter an obstacle (Masi, 2020).

The spatial evolution and time history of the incident overpressure are both seen in Figure 18. At a given distance, R , from the blast source, the overpressure increases almost instantaneously to the peak pressure, P_{so} (Figure 18a). This peak pressure occurs at the arrival time, defined as t_a . This is the

beginning of the positive phase, which lasts for a duration of t_d . During the positive phase, when the time is greater than the arrival time ($t > t_a$), the overpressure decreases exponentially (Figure 18b). At the end of the positive phase, the value of overpressure becomes negative, and enters the negative phase, which lasts for a duration of t_{d-} . In the negative phase, the overpressure asymptotically approaches the ambient pressure, which was the initial value. It should be noted that the absolute value of pressure in the negative phase is much lower than the absolute value of pressure in the positive phase. However, the negative phase has a much longer duration than the positive phase.

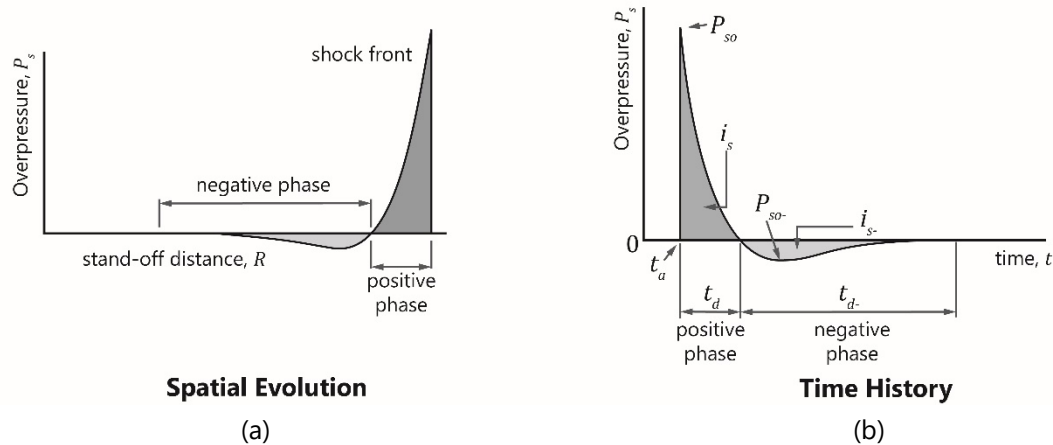


Figure 18. Time-history and spatial evolution of a blast (adapted from Masi, 2020).

The impulse of the positive, i_s , and negative phase, i_{s-} , can be computed as follows in Equation 1 and Equation 2, respectively.

$$i_s = \int_{t_a}^{t_a+t_d} P_s(t) dt \quad \text{Equation 1}$$

$$i_{s-} = \int_{t_a+t_d}^{t_a+t_d+t_{d-}} P_s(t) dt \quad \text{Equation 2}$$

The applied pressure of the blast load can be idealized as a triangular-shaped load for design purposes. Two different approaches to this simplification exist. The first is a conservative approach (I, Figure 19), which considers the maximum value of the pressure and the entire duration of the positive phase. The second (II, Figure 19) keeps the same maximum pressure value as the original curve but calculates the duration of the load such that the new impulse from the triangular load and the original impulse are identical. The equation for the impulse, i , is the area of the triangular load, given as follows:

$$i = \frac{1}{2} P_{so} t_d \quad \text{Equation 3}$$

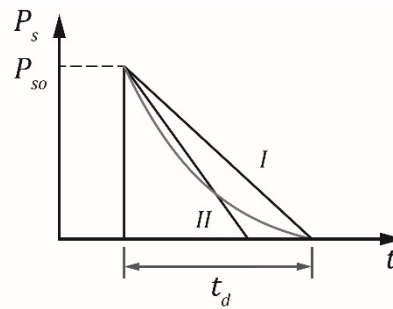


Figure 19. Idealized blast loading profile (adapted from Pereira, 2014).

3.1.1 Scaling Laws

Scaling laws allow for parametric correlations between a given explosion and a standard charge of the same substance. This is typically done to predict the effects of large-scale explosions using a significantly smaller scale. More information related to the scaling laws can be found in Brode (1955) and all references to the equations will not be discussed later in text. Using the Hopkinson-Cranz scaling laws (Hopkinson, 1915) (Cranz, 1925), the scaled distance, Z , in $m/kg^{1/3}$, can be given as follows:

$$Z = R/W^{1/3} \tag{Equation 4}$$

where R is the standoff distance from the centre of the detonation, in m, and W is the charge mass in kg of equivalent TNT.

3.1.2 Equivalent TNT

All blast parameters are dependent on the magnitude of the explosion, measured by the amount of energy released, otherwise known as the explosive yield. The generally accepted reference standard for the explosive yield is the energy released in equivalent mass of TNT. Thus, for explosives other than TNT, the equivalent energy is determined as follows:

$$W_{TNT} = \frac{Q_x}{Q_{TNT}} W_x \tag{Equation 5}$$

where W_{TNT} is the equivalent charge in TNT, W_x is the mass of a given explosive, Q_x is the mass specific energy of the given explosive, and Q_{TNT} is the mass specific energy of TNT. Common TNT equivalents of explosive charges and their mass specific energy in kJ/kg can be seen in Table 1.

Table 1. Explosives and their charge factors, CF (Bangash & Bangash, 2006)

Explosives	Mass specific energy (kJ/kg)	TNT equivalent (CF)
TNT	4520	1.00
GDN (glycol dinitrate)	7230	1.60
Pyroxilene	4750	1.05
Pentrite	6690	1.48
Dynamite	5880	1.30
Schneiderite	3160	0.70
Dinitrotoluene (DNT)	3160	0.70
Ethylenedinitramine	5650	1.25
Compound B [0.6RDX + 0.4TNT0]	5190	1.15
RDX (cyclonite)	5360	1.18
HMX	5650	1.26
Semtex	5660	1.25
Dentolite 50/50	-	1.13
DENT	-	1.28

The charge contained in the explosive device is used to define its size. According to Bangash and Bangash (2006), explosive devices can be categorized in four sizes:

- Small explosions (up to 5 kg of TNT);
- Medium explosions (up to 20 kg of TNT);
- Large explosions (up to 100 kg of TNT); and,
- Very large explosions (up to 2500 kg of TNT).

3.1.3 External Blast Loading

External (or unconfined) explosions are classified based on the relative position and angle of the source of the explosion, and the structure subjected to the blast load. Three classifications of external blast loading exist and are described as follows (UFC 3-340-02, 2008).

- *Free-air burst*: this explosion occurs in free air. The blast waves spread outwards from the source in the form of a sphere and do not interact with the ground or any other obstacle prior to acting on the structure.
- *Airburst*: this explosion occurs in free air. The blast waves spread outwards from the source in the form of the sphere and will interact with the ground prior to acting on the structure.
- *Surface burst*: this explosion happens near the ground surface. The blast waves interact with the ground immediately prior to spreading hemispherically outwards and acting on the structure.

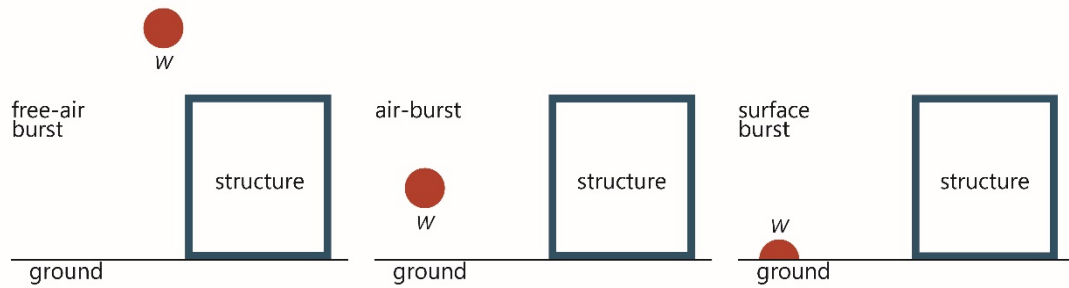


Figure 20. Classifications of external explosions: free-air, air, and surface burst (adapted from Masi, 2020).

3.1.3.1 Analytical solutions for overpressure

One of the key parameters when dealing with blast is the determination of the overpressure generated from the explosion. Usually, this depends on the mass of the explosive and the distance between the explosive and the point of measurement. It should be noted that the analytical solutions developed over the years depend on the type of explosion (Figure 20).

3.1.3.1.1 Spherical Airbursts

Multiple studies have been conducted in order to estimate the overpressures generated from spherical airbursts, developed from various large sets of experimental data with different sizes of blasts and scaled distances. Sadovskyi (1952) introduced the following equation:

$$P_{so} = \frac{0.085}{Z} + \frac{0.3}{Z^2} + \frac{0.82}{Z^3} \quad \text{Equation 6}$$

Here, Z represents the scaled distance, in $\text{m/kg}^{1/3}$, and the peak side-on overpressure, P_{so} , is presented in MPa.

In 1955, Brode introduced an analytical solution for the estimation of the peak side-on overpressure due to spherical blast (Brode, 1955):

$$P_{so} = \begin{cases} \frac{0.67}{Z^3} + 0.1, & \text{for } (1 < P_{so}) \\ \frac{0.0975}{Z} + \frac{0.1455}{Z^2} + \frac{0.585}{Z^3} - 0.0019, & \text{for } (0.01 \leq P_{so} \leq 1) \end{cases} \quad \text{Equation 7}$$

where Z represents the scaled distance, in $\text{m/kg}^{1/3}$, and the peak side-on overpressure, P_{so} , is presented in MPa.

Kinney and Graham (1985) proposed the following to estimate the peak side-on overpressure:

$$P_{so} = P_o \frac{808 \left[1 + \left(\frac{Z}{4.5} \right)^2 \right]}{\sqrt{\left[1 + \left(\frac{Z}{0.048} \right)^2 \right]} \times \sqrt{\left[1 + \left(\frac{Z}{0.32} \right)^2 \right]} \times \sqrt{\left[1 + \left(\frac{Z}{1.35} \right)^2 \right]}} \quad \text{Equation 8}$$

where Z represents the scaled distance, in $\text{m/kg}^{1/3}$, P_o represents the ambient pressure, in MPa, and the peak side-on overpressure, P_{so} , is presented in MPa.

Mills (1987) also provided an expression to estimate the peak side-on overpressure, P_{so} :

$$P_{so} = \frac{1.772}{Z^3} + \frac{0.114}{Z^2} + \frac{0.108}{Z} \quad \text{Equation 9}$$

where Z represents the scaled distance, in $\text{m/kg}^{1/3}$, and the peak side-on overpressure, P_{so} , is presented in MPa.

3.1.3.1.2 Hemispherical Surface Bursts

For hemispherical explosions, there have also been several proposals over the years. These equations have been developed based on various large sets of experimental data which used different sizes of blasts and scaled distances. In 1961, Newmark and Hansen provided an expression to calculate the peak overpressure for high explosive charges detonated near the ground (Newmark & Hansen, 1961):

$$P_{so} = 0.6784 \frac{W}{R^3} + 0.294 \left(\frac{W}{R^3} \right)^{\frac{1}{2}} \quad \text{Equation 10}$$

Here, R represents the distance, in m, and W represents the charge of the explosion, in kg. The overpressure, P_{so} , is presented in MPa.

Wu and Hao (2005) have also presented expressions for the determination of peak overpressure for hemispherical bursts:

$$P_{so} = \begin{cases} 1.059 \left(\frac{R}{W^{\frac{1}{3}}} \right)^{-2.56} - 0.051, \text{ for } \left(0.1 \leq \frac{R}{W^{\frac{1}{3}}} \leq 1 \right) \\ 1.008 \left(\frac{R}{W^{\frac{1}{3}}} \right)^{-2.01} - 0.051, \text{ for } \left(1 < \frac{R}{W^{\frac{1}{3}}} \leq 10 \right) \end{cases} \quad \text{Equation 11}$$

Here, R represents the distance, in m, and W represents the charge of the explosion, in kg. The overpressure is presented in MPa.

3.1.3.2 Interaction with the structure

When a blast wave starts developing and spreading outwards, it interacts with the surrounding environment. Blast waves can reflect and diffract, similarly to other types of waves. When a blast wave reaches a solid surface (or an object denser than air) it will reflect from it, and depending on its

geometry and size, diffract around it. This reflection phenomenon will cause an amplification of the peak overpressure. These amplification factors mostly depend on the intensity of the wave and its angle of incidence.

For large scale explosions, the different façades of the structure will be subjected to two different types of loads: the diffraction of the blast wave around the entire structure, and the drag force due to the dynamic pressures. This phenomenon is observed in Figure 21. The peak side-on overpressure applied to the front façade (Figure 21a) is the reflected pressure, P_r . This occurs at the moment the incident shock front reaches the wall. The reflected pressure will decay at a time t_c , known as the clearing time, and will decay until the pressure is equal to the sum of the time-varying incident and dynamic pressures. In Figure 21a, the clearing time t_c is the difference between $t - t_{a1}$, where t_{a1} is the arrival time of the blast wave on the front façade. The clearing time can be defined as follows (UFC 3-340-02, 2008):

$$t_c = \frac{4S}{\left(1 + \frac{S}{G}\right) C_r} \quad \text{Equation 12}$$

where S is the clearing distance, in m, and is the lowest of the height of the front wall or half of the width. G is the greatest of the wall height or half the width, in m. C_r is defined as the sound velocity in the reflected region, in m/ms. The clearing time, t_c , is given in milliseconds.

The top and sides of the structure (Figure 21b) see a deviation from the linear decay of pressure when the blast is halfway along the structure, defined as time t_{a2} . This is due to the complex flow where the top and sides of the building connect with the front façade. On the rear façade (Figure 21c), the load profile is a non-zero rise time due to the time the blast waves need to travel to the rear of the building in order to complete its diffraction process. The arrival time of the blast wave on the rear façade is defined as t_{a3} .

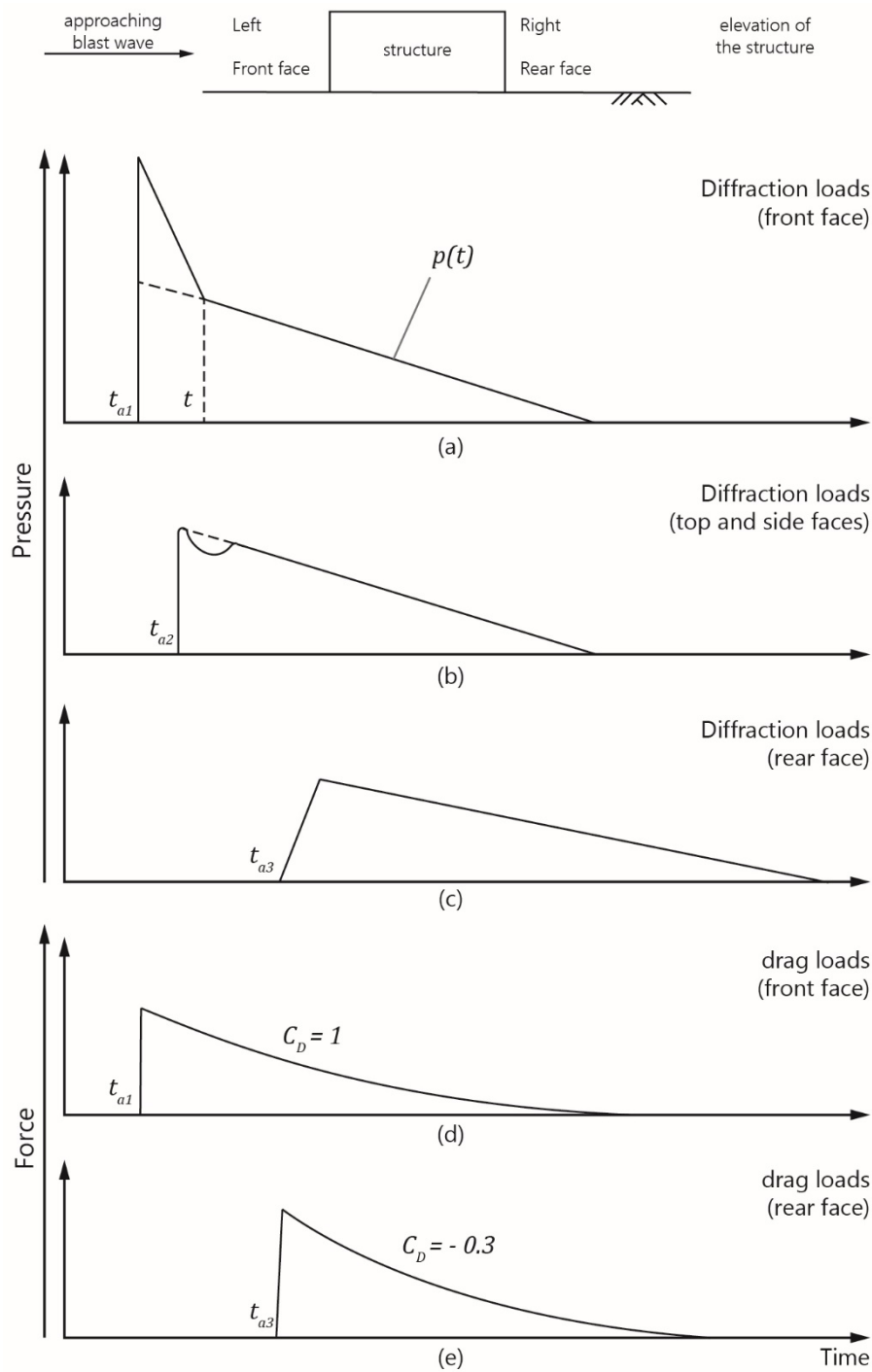


Figure 21. External blast wave loading on a structure (adapted from Cormie et al., 2011).

The drag loads on the front and rear façades of the building due to the dynamic pressure component of the blast wave can be seen in Figure 21d and Figure 21e, respectively. This drag force, F_D , can be defined as follows:

$$F_D = C_D \times P_d \times A \tag{Equation 13}$$

where C_D is the drag coefficient of the target based on the target's geometry, A is the area loaded by the pressure, in m^2 , and P_d is the dynamic pressure, in MPa. The drag force, F_D , is given in kN. The maximum dynamic pressure can be defined as follows (Liepmann & Roshko, 1957):

$$P_{d,max} = \frac{5P_{so}^2}{2(P_{so}+7P_o)} \quad \text{Equation 14}$$

The dynamic pressure, q_s , can also be defined in kN/m^2 as follows:

$$P_d = \frac{1}{2}\rho_s u_s^2 \cdot 0.001 \quad \text{Equation 15}$$

where ρ_s is the density of air, in kg/m^3 , and u_s is the particle velocity behind the wavefront given by:

$$u_s = \frac{a_0 P_{so}}{\gamma P_o} \left(1 + \left(\frac{\gamma + 1}{2\gamma} \right) \frac{P_{so}}{P_o} \right)^{-1/2} \quad \text{Equation 16}$$

where P_{so} is the peak overpressure, in MPa, a_0 is the speed of sound in the undisturbed atmosphere, in m/s, and γ is the specific heat ratio. The particle velocity, u_s , is given in m/s.

For an incident angle of zero degrees, the reflected pressure will be given by the following equation:

$$P_r = 2P_{so} + (\gamma + 1)P_d \quad \text{Equation 17}$$

By introducing Equation 15 and Equation 16 into Equation 17, and by setting the specific heat ratio of air, γ , to the known value of 1.4, the following equation is obtained:

$$P_r = 2P_{so} \left(\frac{7P_o + 4P_{so}}{7P_o + P_{so}} \right) \quad \text{Equation 18}$$

Multiple empirical relations exist to define the arrival time, t_a , of the shock wave front. Kinney and Graham (1985) have previously introduced the following:

$$t_a = \frac{1}{a_o} \int_{r_c}^R \left[\frac{1}{1 + \frac{6P_{so}}{7P_o}} \right]^{\frac{1}{2}} dR = \frac{1}{a_o} \int_{r_c}^R \left(\frac{1}{M_x} \right) dR \quad \text{Equation 19}$$

where a_o is the speed of sound in the undisturbed atmosphere, in m/s, M_x is the Mach number, r_c is the charge radius, in m, R is the standoff distance, in m, P_o is the atmospheric pressure, in MPa, and P_{so} is the peak side-on overpressure, in MPa. The arrival time, t_a , is given in milliseconds.

Wu and Hao (2005) developed another approach to calculating the arrival time, t_a , which is given as follows:

$$t_a = 0.34 \frac{R^{1.4} W^{-0.2}}{a_o} \quad \text{Equation 20}$$

where R is the distance, in m, W represents the charge of the explosion, in kg, and a_o represents the speed of sound in the undisturbed atmosphere, in m/s. The arrival time, t_a , is given in milliseconds.

A subsequent equation for the arrival time of the shock wave front was developed by Iqbal and Ahmad (2009) as follows:

$$t_a = 560 \frac{R^{1.4} W^{-0.2}}{a_o} \quad \text{Equation 21}$$

where R is the distance, in m, W represents the charge of the explosion, in kg, and a_o represents the speed of sound in the undisturbed atmosphere, in m/s. The arrival time, t_a , is given in milliseconds.

According to an investigation by Ullah et al. (2017), the equation by Wu and Hao (Equation 20) is the closest to the UFC charts (UFC 3-340-02, 2008), and the equation by Kinney and Graham (Equation 19) gives the largest value of arrival time.

With respect to the duration of the positive phase of the blast wave, several empirical relations exist. Sadovskiy (1952) defined the following:

$$t_d = 1.2 \sqrt[6]{W} \sqrt{R} \quad \text{Equation 22}$$

where R is the standoff distance, in m, W represents the charge of the explosion, in kg. The positive phase duration, t_d , is given in milliseconds.

Kinney and Graham (1985) defined the following equation for the positive phase duration:

$$t_d = \frac{980 \left[1 + \left(\frac{Z}{0.54} \right)^{10} \right]}{\left[1 + \left(\frac{Z}{0.02} \right)^3 \right] \left[1 + \left(\frac{Z}{0.74} \right)^6 \right] \sqrt{1 + \left(\frac{Z}{6.9} \right)^2}} W^{\frac{1}{3}} \quad \text{Equation 23}$$

where Z represents the scaled distance, in $\text{m/kg}^{1/3}$, and W represents the charge of the explosion, in kg. The positive phase duration, t_d , is given in milliseconds.

Another formulation by Bangash and Bangash (2006) exists to estimate the positive phase duration based on the charge of the explosive device and the peak side-on overpressure:

$$t_d = 10.23 \frac{W^{1/3}}{\sqrt{P_{so}}} \quad \text{Equation 24}$$

where W represents the charge of the explosion, in kg, and P_{so} represents the peak side-on overpressure, in bars. The positive phase duration, t_d , is given in milliseconds.

Iqbal and Ahmad (2009) defined the following:

$$t_d = 4.6 \left(\frac{R}{W^{\frac{1}{3}}} \right)^{-0.1} + 2.462 \left(\frac{R}{W^{\frac{1}{3}}} \right)^{-0.472} \quad \text{Equation 25}$$

where R is the standoff distance, in m, W represents the charge of the explosion, in kg. The positive phase duration, t_d , is given in milliseconds.

According to Ullah et al. (2017), the equation given by Iqbal and Ahmad (Equation 25) gives the largest value of positive phase duration, whereas the equation from Kinney and Graham (Equation 23) gives the smallest value for most of the range. Sadovskyi's equation (Equation 22) gives the closest values to those of the UFC (UFC 3-340-02, 2008).

3.1.4 Internal Blast Loading

Internal (or confined) explosions occur when each surface is subjected to the shock waves caused by the reflections of multiple surfaces. The loading density, which is defined as the charge weight over the free volume of the structure, will determine if the internal explosion is fully vented, partially confined, or fully confined (UFC 3-340-02, 2008):

- *Fully vented explosion*: produced within or immediately beside a barrier or a cubicle-like structure with at least one surface open to the atmosphere. The initial shock wave and the detonation products are fully vented to the atmosphere and can spread away from the structure.
- *Partially confined explosion*: produced within a barrier or a cubicle-like structure having a limited number and size of openings. The initial shock wave and the detonation products can be vented to the atmosphere after a given period of time. As the detonation products are confined, the accumulation of high temperatures and gaseous products occur, and results in a quasi-static pressure with a longer duration than the shock wave.
- *Fully confined explosions*: produced within a barrier structure with total or near total containment. The internal blast loads are composed of unvented shock loads with long duration quasi-static pressure which varies based on the degree of confinement.

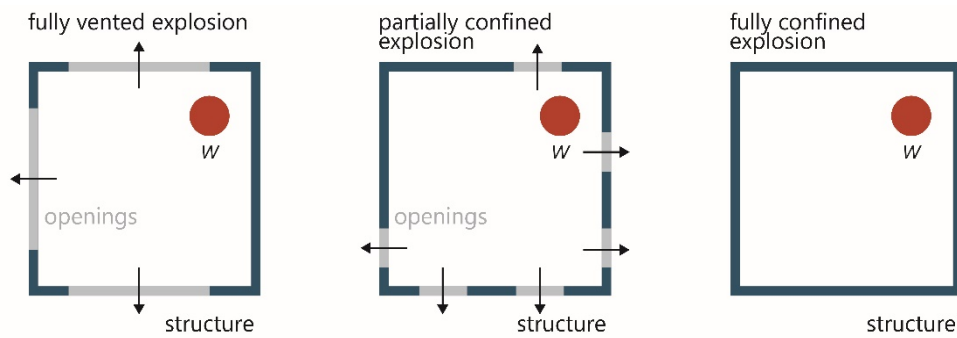


Figure 22. Classifications of internal explosions: fully vented, partially confined, and fully confined explosions (adapted from Masi, 2020).

A blast occurring in an internal or confined environment increases the effect of that blast on the structure. In an internal blast, the peak reflected overpressure will be amplified (Remennikov & Rose, 2005). Not only is the peak overpressure in a confined space greater in magnitude than an unconfined explosion, but the blast wave also has a longer duration (Liu et al., 2008; Shi et al., 2009). As the impulse is defined by the area of the overpressure history, the increase in the peak overpressure and length of the blast will result in an enhanced impulse.

Additionally, studies have shown that the overpressure time-history inside a structure is more complex than that of an external blast. In fact, in a confined blast, multiple shock reflections with significant magnitudes can be expected to occur over a significant period of time. This phenomenon, seen in Figure 23, was observed by Chan and Klein (1994). Two distinct loading phases exist in a confined explosion. The reflected shock loading is the first phase in this loading scenario. This initial reflected shock is closely followed by a series of reflected pulses due to the reverberation of repeated wave reflections. The second loading phase is a result of the expansive combustion, which causes a build-up of pressure. This type of loading is also called gas pressure loading (Cormie et al., 2011).

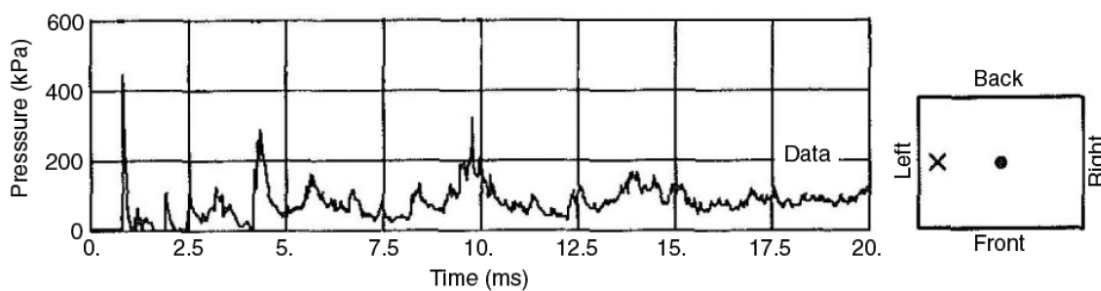


Figure 23. Overpressure time-history response for a rectangular bunker with a sensor on the left (Chan & Klein, 1994).

At an incident angle of 90° , no reflection occurs, and the peak side-on overpressure is the load on the surface. For incident angles between 0° and 90° , both regular reflection and Mach reflection exist (Smith & Hetherington, 1994). Regular reflection occurs at angles between 0° and 40° , while Mach reflection occurs at angles greater than 40° . These reflection coefficients, C_{ra} , can be seen plotted against the incident angle, α , for a range of incident overpressure in Figure 24.

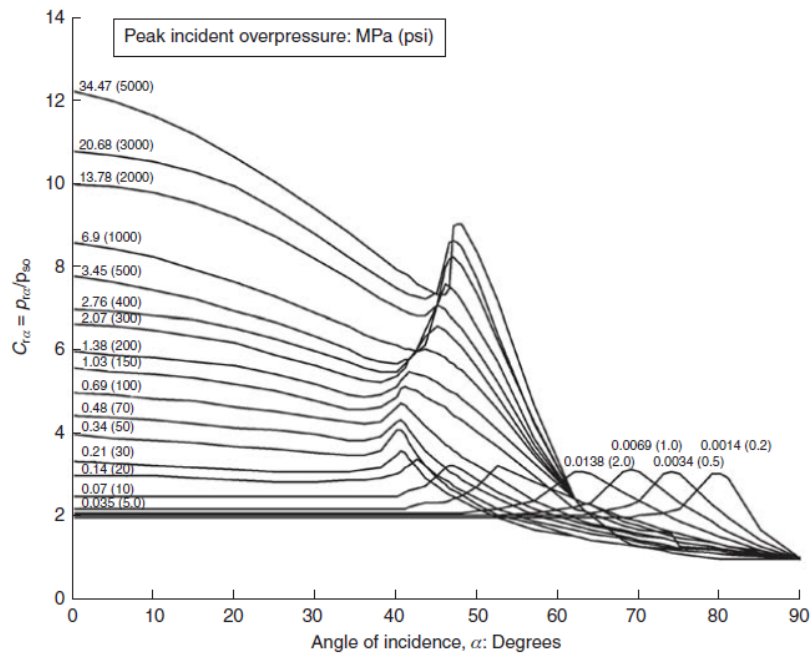


Figure 24. Change of the reflection coefficient caused by the angle of incidence (UFC 3-340-01, 2002).

Thus, the corresponding reflected impulse, i_{α} , can be determined by interpolating between the incident impulse, i_s , and normally-reflected impulse, i_r . The impulses can be defined in kN-s. The interpolation equation is as follows (Cormie et al., 2011):

$$i_{\alpha} = i_s(1 + \cos \alpha - 2 \cos^2 \alpha) + i_r \cos^2 \alpha \quad \text{Equation 26}$$

Unlike initial reflected shock wave parameters (P_r , i_r), the magnitude of re-reflected waves is more difficult to quantify. Nevertheless, an approximate analysis of internal pressure time-histories can be done by idealizing the shock pulse as a triangular load, as discussed previously.

Baker et al. (1980) suggested an approach where the peak pressure is reduced by half for each re-reflection, while keeping the duration of each pulse constant. Thus, the impulse is also decreased by half for each pulse. It is assumed that the pressure of any reflected wave is equal to zero after three reflections. This phenomenon is illustrated in Figure 25, and is better represented by the equations below.

$$\begin{aligned} P_{r_2} &= \frac{1}{2}P_{r_1} & i_{r_2} &= \frac{1}{2}i_{r_1} \\ P_{r_3} &= \frac{1}{2}P_{r_2} = \frac{1}{4}P_{r_1} & i_{r_3} &= \frac{1}{2}i_{r_2} = \frac{1}{4}i_{r_1} \\ P_{r_4} &= 0 & i_{r_4} &= 0 \end{aligned} \quad \text{Equation 27}$$

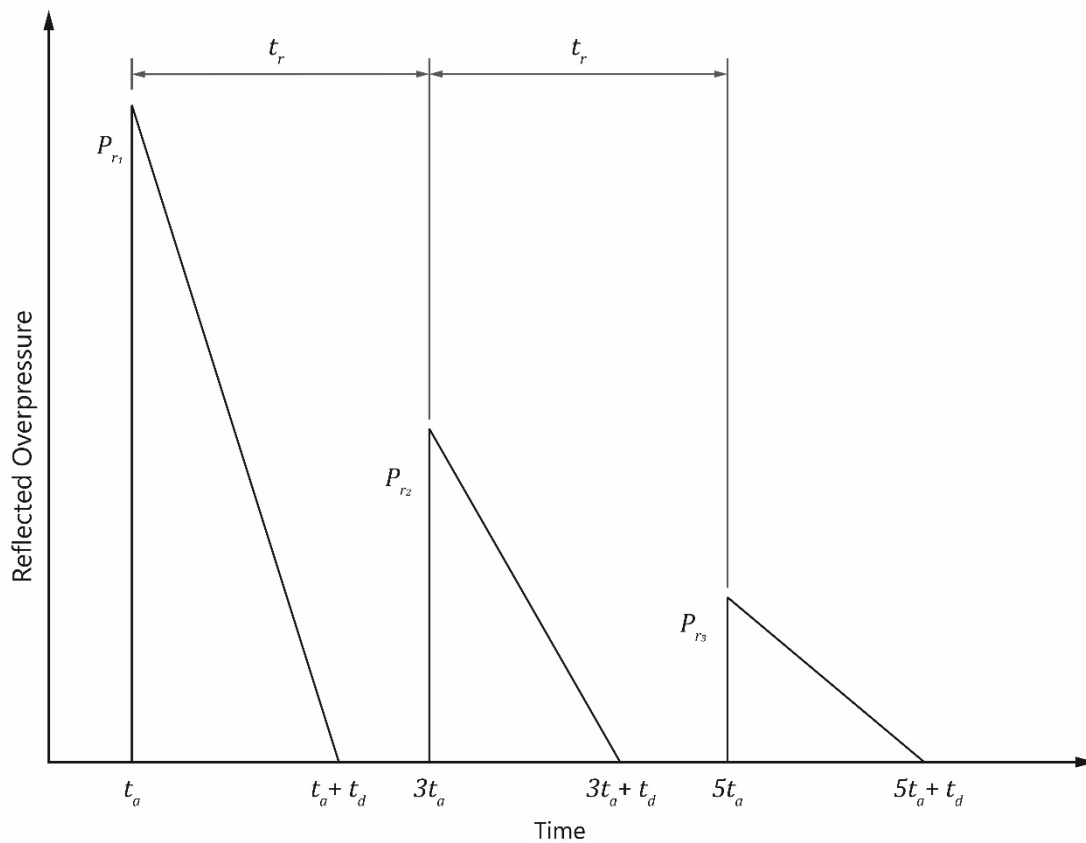


Figure 25. Simplification of the internal blast wave reflections (adapted from Cormie et al., 2011).

The reverberation time can also be defined as the delay between each blast wave arriving at an internal surface in the structure. Another assumption of this simplification is that the reverberation time, t_r , is constant. The reverberation time can also be defined as $t_r = 2t_a$, where t_a is the arrival time of the first blast wave. This assumption deviates from the reality in that the successive shocks will be weaker and consequently will travel more slowly than the first shock wave.

Another simplification by Baker et al. (1980) can be made if the response time of the loaded structure is significantly longer than the total duration ($5t_a + t_d$). All three pulses can be combined into a single pulse where the total peak pressure, P_{rT} , and total specific impulse, i_{rT} , can be defined as follows:

$$P_{rT} = P_{r1} + P_{r2} + P_{r3} = 1.75P_{r1} \tag{Equation 28}$$

$$i_{rT} = i_{r1} + i_{r2} + i_{r3} = 1.75i_{r1} \tag{Equation 29}$$

It should be noted that the use of these assumptions will lead to the overestimation of the structural response and consequently a more conservative design.

3.1.5 Structural response

The analysis of the dynamic response of blast-loaded structures requires consideration of the non-linear inelastic material behaviour, of the effect of the high strain rates, the uncertainties of blast load

calculations, and the time-dependent deformations. Still, many widely accepted assumptions can be made to simplify the analysis.

The structure can be idealized as a single degree of freedom (SDOF) system. This is often done as the final state of the structure is typically more important than the displacement time-history of the structure. The link between the positive phase of the blast and the structure's natural vibration period can also be established. Thus, the blast load can be idealized, and the classification of the blast load regimes can be simplified. Here, the structure can be replaced by an equivalent system composed of a concentrated mass and a weightless spring, to represent the resistance of the structure to deformation (Figure 26). The external force, $F(t)$, acts on the mass of the structure, M . The structural resistance is expressed by the vertical displacement, u , and the spring constant, K .

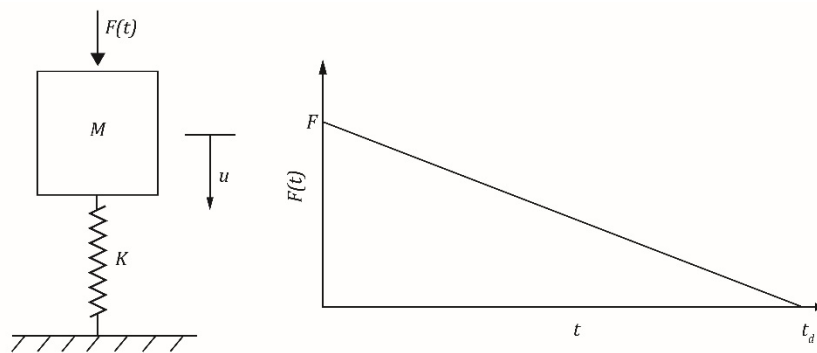


Figure 26. SDOF system subjected to an idealized blast load (adapted from Cormie et al., 2011).

As previously stated, the loading profile of a blast can be simplified as a triangular load shape, with a peak P_r and a positive phase duration t_d . Thus, the equation of motion of the undamped elastic system can be given as follows for a time ranging between zero and the end of the positive phase duration, t_d .

$$M\ddot{u} + Ky = P_r \left(1 - \frac{t}{t_d}\right) \quad \text{Equation 30}$$

The general solutions for the displacement and the velocity can be expressed as follows in Equation 31 and Equation 32, respectively. By setting $\frac{du}{dt}$ in Equation 31 to zero, the maximum dynamic deflection u_{max} can be evaluated (Cormie et al., 2011).

$$u(t) = \frac{P_r}{K} (1 - \cos\omega t) + \frac{P_r}{K t_d} \left(\frac{\sin\omega t}{\omega} - t \right) \quad \text{Equation 31}$$

$$\ddot{u}(t) = \frac{du}{dt} = \frac{P_r}{K} \left[\omega \sin\omega t + \frac{1}{t_d} (\cos\omega t - 1) \right] \quad \text{Equation 32}$$

The natural circular frequency of vibration of the structure, ω , and the natural period of vibration of the structure, T , are defined in Equation 33.

$$\omega = 2\pi T = \sqrt{\frac{K}{M}} \quad \text{Equation 33}$$

The dynamic load factor, DLF, is defined as the ratio between the maximum dynamic deflection occurring at time t_{max} , u_{max} , over the static deflection, u_{st} , which is a result of the static application of the peak load. The dynamic load factor can be equated as follows (Cormie et al., 2011):

$$DLF = \frac{u_{max}}{u_{st}} = \frac{u_{max}}{P_r/K} = \psi(\omega t_d) = \Psi\left(\frac{t_d}{T}\right) \quad \text{Equation 34}$$

where ψ and Ψ are functions of ωt_d and $\frac{t_d}{T}$, and greatly influence the structural response to blast loading. According to Baker et al. (1980), three loading regimes can be categorized as follows:

- Impulsive loading regime, $\omega t_d < 0.4$
- Quasi-static loading regime, $\omega t_d > 40$
- Dynamic loading regime, $0.4 < \omega t_d < 40$

The *impulsive loading regime* occurs when the positive phase duration is small with respect to the natural period of vibration. Here, the force has finished acting on the structure before the structure is able to respond significantly. Thus, most deformations will occur after the time t_d . The *quasi-static loading regime* occurs when the positive phase duration is large with respect to the natural period of vibration. If the structure reaches maximum deflection, the force may be considered as constant. The *dynamic loading regime* occurs when the positive phase duration and the natural period of vibration are similar. The evaluation of the structural response is more complex if this occurs.

In the event that a structure cannot be idealized by the SDOF simplification, a multi-degree of freedom (MDOF) analysis using numerical methods can be applied. This MDOF system approach is based on the lumped-mass assumption, where the total number of degrees of freedom of the equivalent system is equal to the number of possible motions of the system. An equation of motion exists for each degree of freedom and these equations are used to compute the natural frequencies and corresponding modes of the system (Pereira, 2014).

When subjected to blasts, structural elements experience large plastic deformations. In addition to these effects, strain rate effects, strain hardening, and temperature variation can be considered using numerical simulations. To run numerical simulations, software capable of performing non-linear explicit analysis must be used, in conjunction with the use of Finite Elements (FE). According to Yandzio and Gough (1999), the most acceptable levels of accuracy for the dynamic response of a structure is through the use of FE analysis techniques. For simple components such as beams, slabs, columns, and walls, simpler methods, such as SDOF and MDOF, can be used to model and predict the structural response. When analyzing complete buildings or complex structural components, the use of nonlinear finite element analysis using explicit dynamics is recommended (Pereira, 2014).

3.2 Impact Loading

Impact loading falls under the "dynamic loads" category. When an object in motion hits a structure, the response will depend on the velocity and the material properties of both the structure and the object in motion. Thus, if a high velocity impact between a minor object and a structure occurs, local

damage around the impact zone will develop much faster than the global deformation of the structure. Additionally, the stresses will depend on the material properties of both the object and the structure (Ekström, 2017). For a structure under concentrated impact loading, the structural component can demonstrate different behaviours: a local failure response (Figure 27a) and a global failure response (Figure 27b).

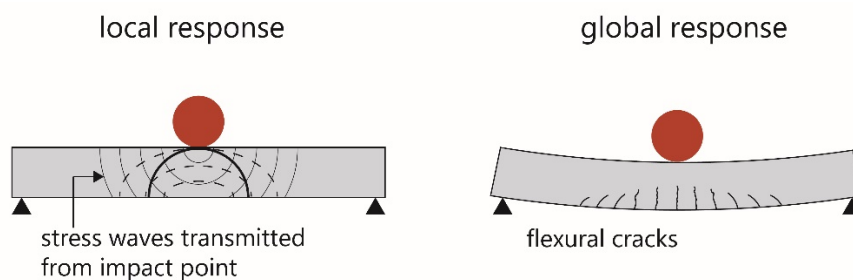


Figure 27. Concrete beams subjected to impact loading: (a) local response; (b) global response (adapted from Fujikake et al., 2009).

When analyzing a structure under impact loading, numerical simulation can be used. Materials subjected to different speeds of impact will have different strength properties, and this effect modifies the resistance of the material with respect to penetration. Methods of numerical identification can be used to describe the material properties of a structure when subjected to an impact at different velocities. Common material models for the numerical modelling of solid penetration through a structure are: the Mohr-Coulomb model, the Johnson-Cook model, the Zerilli-Armstrong model, and the thermo-mechanical material model (Žmindák et al., 2016).

Abaqus/Explicit can be used to simulate ballistic impact. The explicit dynamic analysis procedure in Abaqus/Explicit uses the implementation of an explicit integration rule in combination with diagonal or “lumped” element matrices (Žmindák et al., 2016). The lumped mass matrix, \mathbf{M} , and the internal and external forces ($\mathbf{F}(t)^{int}$ and $\mathbf{F}(t)^{ext}$, respectively) enable the calculation of the nodal accelerations at any point in time, $\ddot{\mathbf{u}}(t)$, according to:

$$\ddot{\mathbf{u}}(t) = \mathbf{M}^{-1} \cdot \mathbf{F}(t)^{ext} - \mathbf{F}(t)^{int} \quad \text{Equation 35}$$

3.2.1 Classifications of Impact Loading

Impact loads can be classified in two ways: either by their intensity and duration, or by the dissipative mechanism.

Classifications based on Intensity and Duration

Three classifications of impact loading that are based on the load’s impact and duration are: particle impact, rigid body impact, and transverse impact on flexible bodies (Kam-wing Wong, 2005). Particle impact is an analytical approximation which only considers the normal component of the impact force. This type of impact is for unspecified sources of force but with a strong force and a very short duration, the latter which can be considered negligible. This type of impact can provide a simple solution if the global structural vibration is negligible and only the kinematics of impact are concerned

(Kam-wing Wong, 2005). Rigid body impact occurs between two compact bodies where the contact area is small relative to the dimensions of all sections. With the increase in radial distance from the contact region, the stress created in the contact area decreases significantly. The time-history of the impact force, with the exception of the kinematics of impact, can be obtained by various contact laws. The rigid body impact can be modelled using the massive beam model and the effective mass model (Kam-wing Wong, 2005). Transverse impact on flexible bodies occurs if the impact force results in one of the bodies displacing in bending. As the bending leads to a reduction in the stiffness, the impact force is consequently reduced (Kam-wing Wong, 2005).

Classifications based on Dissipative Mechanism

Two classifications of impact loading based on the dissipative mechanism was proposed by Eurocode (CEN, 2003) for concrete structures. The first classification is a hard impact where the initial kinetic energy is dissipated by striking objects. The objects involved in this impact can have a deformable component, such as the deformable bows on vehicles. The second classification is soft impact. Here, most of the initial kinetic energy is dissipated by the structure being impacted. Both objects involved in this classification are rigid.

3.2.2 Structural response

When considering the classifications of impact as defined by Eurocode, two simplified approaches can be used to understand the global response of concrete structures under soft and hard impacts. For soft impacts, this can be simplified into a single degree of freedom problem. For hard impacts, this can be simplified into a two degree-of-freedom problem. The spring models can be seen in Figure 28. In the single degree-of-freedom model seen in Figure 28a, a distributed impact load, $p(t)$, is acting on a partial mass of the structure, M_1 . The impact load can be idealized with a mass point element connected to a spring element, which represents the global stiffness of the member when subjected to an equal concentrated dynamic load. In the two degree-of-freedom model seen in Figure 28b, the impactor is modelled as a mass instead of a distributed load. The idealized system is represented by two lumped masses, M_1 and M_2 , connected by a spring.

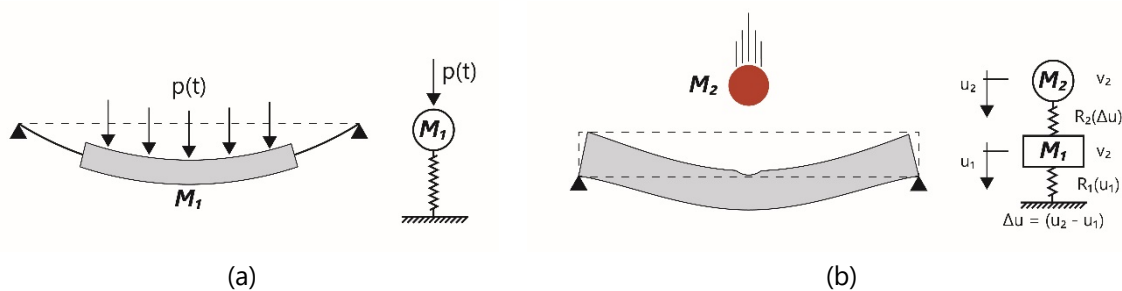


Figure 28. Simplified models recommended by Eurocode for structures under impact loads (adapted from CEN, 2003).

3.3 History of Military Weapons

The Alhambra (Section 2) has been used as a fortress or stronghold in many different centuries. From sieges to military bases, a large variety of military weapons could have caused structural damage to the building over the centuries. The explosion of a gunpowder factory below the *Torre de la Vela* in

1590 further emphasizes this possibility. This section intends to gather knowledge on old military weapons, so that reasonable scenarios can be considered in the following sections.

3.3.1 Gunpowder

Gunpowder was first invented in China during the 9th century and spread throughout most of Eurasia by the end of the 13th century. Though it was originally developed for medicinal purposes, gunpowder was used for warfare around 904 AD (Andrade, 2016). Black powder was the type of gunpowder employed in all firearms until other types of smokeless propellants were invented in the late 1800s. Although the term "black" powder is typically utilized, this type of gunpowder was sometimes brown (Hall, 1952). Even though many explosive compounds have been known for centuries, the first accurate formula for black powder dates to 1044 by a Chinese official. In the 1300s, this mixture was widely applied by both Chinese and Mongols for fire arrows, bombs, and rockets. In the mid-thirteenth century, black powder was used by Muslim artilleryists to create explosive trebuchet projectiles. Black powder was then brought to Europe by the Muslims. The first reliable record of black powder formula in the West was made in 1267. Until the 1380s when the Europeans developed a way to manufacture saltpeter (potassium nitrate), European gunpowder manufacturers had to import saltpeter from the East (Kinard, 2007).

Black powder is the combination of three main ingredients: saltpeter, charcoal, and sulphur. However, the proportions of this mixture have been modified and refined over the years. The early European black powder recipe was created using equal parts of all three ingredients. Over time, the amount of saltpeter was increased until the proportions were reported to be 4-1-1 by weight. In the late 1700s, common war powder was created, and had proportions of 6-1-1. Eventually, the recipe for black powder was refined to proportions of 75-15-10 by weight (Hall, 1952).

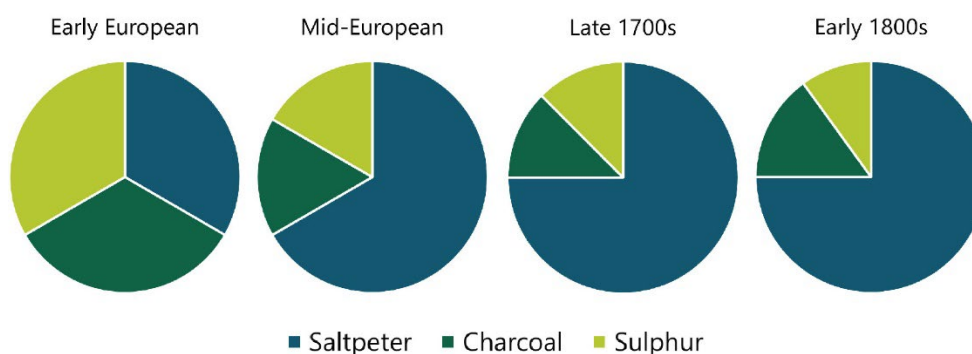


Figure 29. Composition of black powder over the years.

Gunpowder storage was an important aspect to consider as it is highly sensitive to flames, sparks, and moisture. In places such as Canada, Iran, Australia, and the British Isles, buildings called "gunpowder magazines" were designed to store explosive gunpowder in wooden barrels as a safety precaution. During the 18th century, the English had as a standard to build the floor of these magazines half a metre above the ground, and stone chips were laid under the flooring. The gunpowder barrels were typically laid on their sides and rolled to different positions incrementally to prevent the saltpeter from settling at the bottom of the barrel (Manucy, 1949).

With respect to powder barrels, three distinct sizes can be found in the British military in the 1800s and were named after the mass of powder that could be stored in these barrels. The whole barrel could contain 100 lbs (45.4 kg) of powder, the half barrel 50 lbs (22.7 kg), and the quarter barrel 25 lbs (11.3 kg) (Griffiths, 1856). The dimensions of these three barrels can be seen in Table 2.

Table 2. Dimensions of powder barrels (Griffiths, 1856).

	Whole Barrels		Half Barrels		Quarter Barrels	
	[in]	[cm]	[in]	[cm]	[in]	[cm]
Depth	20 ½	52.07	16 ¾	42.55	14	35.56
Diameter at top	15 ½	39.37	12 ¼	31.12	9 ½	24.13
Diameter at bulge	16 ¾	42.55	13 ¼	33.66	10 ¼	26.04
Diameter at bottom	15 ½	39.37	12 ¼	31.12	9 ½	24.13

The chemical formula of black powder can be defined as $\text{KNO}_3:\text{C}:\text{S}:\text{H}_2\text{O}$. Basco et al. (2010) compiled information on the explosion energy (kJ/g) both experimentally and through calculations for TNT and black powder, which can be seen in Table 3. Following a modern-day investigation of an explosion at a black powder manufacturing facility, Reza et al. (2013) determined that 1 kg of black powder is the equivalent of approximately 0.60 kg of TNT.

Table 3. Experimental and calculated explosion energy, in kJ/g, for TNT and black powder (Basco et al., 2010).

Name	Composition (%w/w)	Experimental		Calculations	
		ΔH_{expl}	ΔH_{comb}	ΔH_{expl}	ΔH_{comb}
TNT	$\text{C}_7\text{H}_5\text{N}_3\text{O}_6$	4.6	15.0	5.4	14.9
Black Powder	KNO_3 (75) C (15) S (10)	2.8	8.7	3.0	8.6

3.3.2 Cannons

The earliest known examples of cannons are from the Song dynasty in China, around the 12th century, even though solid archaeological evidence of the same was not found until the 13th century (Gwei-Djen et al., 1988). Evidence of cannons in the Middle East appeared in the 14th century, and cannons were used soon after in Europe. As with gunpowder, cannons were widespread in Eurasia by the end of the 14th century (Andrade, 2016).

Cannons were particularly important during the Granada War. Between 1482 and 1491, the Catholic Monarchs Isabella I of Castile and Ferdinand II of Aragon led a joint project against the Nasrid dynasty's Emirate of Granada. A notable facet of this war was the use of bombards and cannons, which resulted in shortening the sieges in the war. As stated by Cook (1993):

"Gunpowder firepower and artillery siege operations won the Granadan war, and other factors in the Spanish victory were actually secondary and derivative."

As the history of cannons is extensive throughout Europe, the history of cannons in this dissertation will focus specifically on the cannons used in Spain. Illustrations of 16th century Spanish artillery can be seen in Figure 30. A publication by Hall (1952) enumerates the various weights of Spanish cannons in the 17th century and the weight of the shot of those respective cannons (Table 4). This publication also lists the ranges of these cannons based on the possible weight of the shot, and the angle at which they are fired (Table 5). Notably, a replica of the *culverin extraordinary* was made in 2003 as part of the Discovery Channel series *Battlefield Detectives* (Discovery Channel, 2004). This replica achieved a muzzle velocity of 408 m/s with a range of over 450 m when fired at point-blank.

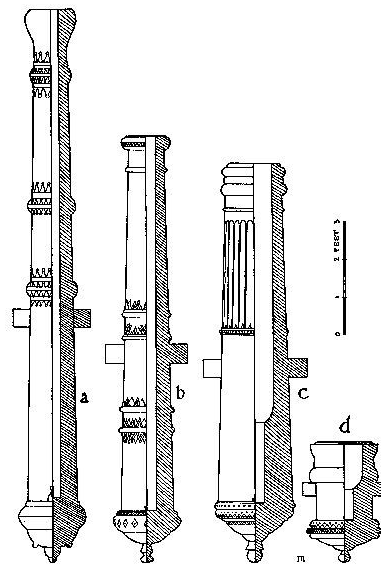


Figure 30. Sixteenth-century Spanish artillery (Manucy, 1949): (a) a culverin (Class 1), (b) a cannon (Class 2), (c) a *pedrero* (Class 3), and (d) a mortar (Class 3) (Manucy, 1949).

Table 4. Weights of Spanish cannons circa 1603 (Hall, 1952) and ("Cannon," 2021).

	Weight of Gun (kg)	Weight of Shot (kg)	Diameter of Shot (cm)
Demi-cannon	1089	7.26	15.40
Culverin	2508	7.26	13.00
Demi-culverin	1270	3.63	10.00
Saker	794	-	8.26
Falconet	476	1.36	5.00

Table 5. Ranges of Spanish cannons circa 1603 (Hall, 1952).

Points of the Quadrant	Point-Blank	7.5°	15°	22.5°	30°	37.5°	45°
Range (m)							
Cannon of 50 lb.	760	1900	2964	3040	3409	3458	3542
Cannon of 45 lb.	722	1824	2888	3000	3393	3511	3572
Cannon of 40 lb.	684	1687	2812	3280	3412	3633	3642
Cannon of 35 lb.	646	1550	2713	3256	3506	3622	3674
Cannon of 30 lb.	608	1418	2600	3213	3523	3659	3724
Demi-cannon of 25 lb.	570	1216	2432	2888	3370	3648	4256
Demi-cannon of 20 lb.	532	1170	2341	2751	3108	3440	4096
Demi-cannon of 12 lb.	456	973	1946	2584	3025	3227	3329
Third-cannon of 12 lb.	380	785	1570	1962	2329	2508	2508
Culverin of 22 lb.	608	1320	2634	4216	4916	5411	5590
Culverin of 20 lb.	547	1186	2394	3800	4552	5006	5472
Culverin of 18 lb.	532	1130	2260	3432	4118	4849	5092
Culverin of 15 lb.	494	1087	2174	3260	3914	4347	4697
Demi-culverin of 12 lb.	456	1003	2006	3010	3610	4063	4332
Demi-culverin of 10 lb.	418	920	1839	2759	3676	3879	4180
Demi-culverin of 8 lb.	380	836	1672	2508	3135	3526	3800
Saker of 6 lb.	342	752	1505	2257	2844	3174	3420
Falcon of 4 lb.	304	669	1338	2006	2508	2821	3040
Falcon of 2 lb.	251	535	1070	1605	2006	2257	2432

CHAPTER 4

4 NUMERICAL MODEL

Numerical modelling is used to mathematically represent the physical behaviour of a structure based on hypotheses and assumptions to simplify the problem. More and more, numerical models are being employed to simulate the response of structures. Numerical models can simulate the non-linear behaviour of materials, large displacements, inter-surface contact, etc. Consequently, they are important for better understanding the structural response of buildings under blast and impact loading. This chapter will present a review of the analysis methods, the behaviour of materials under high strain rates, and the geometry, finite element mesh and material model of the *Torre de la Vela*. The numerical model of the *Torre de la Vela* was implemented in the software Abaqus CAE. The geometry and material properties for this model were based on work done by Vuoto (2020). The geometry of the tower was provided in AutoCAD 3D format and was imported into Abaqus to create the mesh and to conduct the analysis.

4.1 Masonry Structures Under Blast Loading

Several approaches to numerically represent masonry structures exist in the field of structural analysis. The approaches of micro-modelling and macro-modelling are widely accepted in the masonry community. Micro-modelling consists of the modelling of individual components such as the units (brick, stone, etc.) and the mortar. This idea can be further developed into two categories: detailed micro-modelling (Figure 31a) and simplified micro-modelling (Figure 31b). Within the detailed approach, continuum elements are used to represent the units and the mortar joints, and discontinuum elements are used to represent the unit-mortar interface. The simplified approach employs continuum elements to represent expanded units, and discontinuum elements are used to represent the behaviour of mortar joints and the unit-mortar interface. Macro-modelling, seen in Figure 31c, consists of modelling masonry as a composite material, where a homogeneous continuum is employed to represent the units, mortar, and unit-mortar interface (Lourenço, 2008).

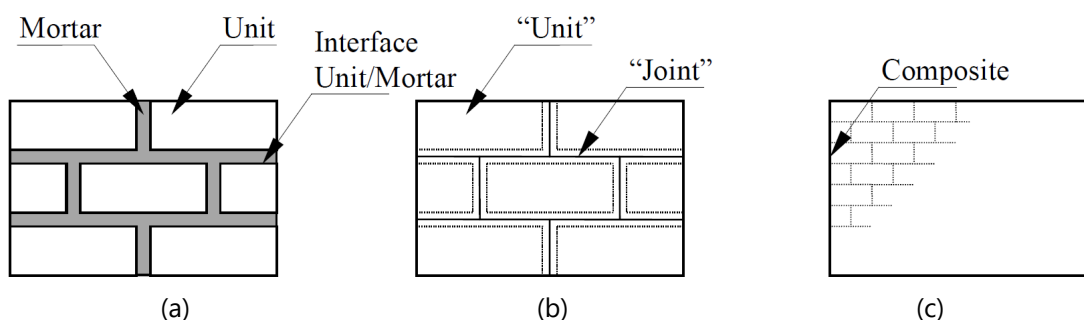


Figure 31. Modelling strategies for masonry structures: (a) detailed micro-modelling; (b) simplified micro-modelling; (c) macro-modelling (Lourenço, 2008).

4.1.1 Abaqus/Explicit

Abaqus/Explicit is a finite element software within the Abaqus/CAE modelling environment that is efficient in analyzing large models subjected to short dynamic response times. This procedure uses an

explicit central-difference time integration rule, where each increment is relatively inexpensive as no solution for a set of simultaneous equations exists. Thus, the operator satisfies the dynamic equilibrium equations at the start of the time increment (ABAQUS, 2010). Previous studies have employed Abaqus/Explicit to model masonry under blast loading. Pereira (2014) conducted a detailed structural safety assessment of public transportation infrastructure using non-linear dynamics available in Abaqus/Explicit. The case study was subjected to various external blast scenarios and the behaviour of the structure under these scenarios was analyzed. This study also proposed increasing the standoff distance as a mitigation measure for reducing the effect of the explosion. Masi (2020) developed a simplified and rapid material model for masonry which were used in large masonry structures subjected to blast loading to obtain preliminary estimates of the structural resistance and failure modes. This continuum model was developed to mimic the meso-scale behaviour of masonry and was compared to both experimental and numerical results using the discrete element method (DEM) (Figure 32). Jablonski et al. (2012) and Zakrisson et al. (2011) have both used Abaqus/Explicit to simulate blast events in soils and in metal elements. Abaqus/Explicit has also been used to model stone masonry (Abdulla et al., 2017), adobe masonry (Tarque et al., 2014), and rammed earth (Bui et al., 2019).

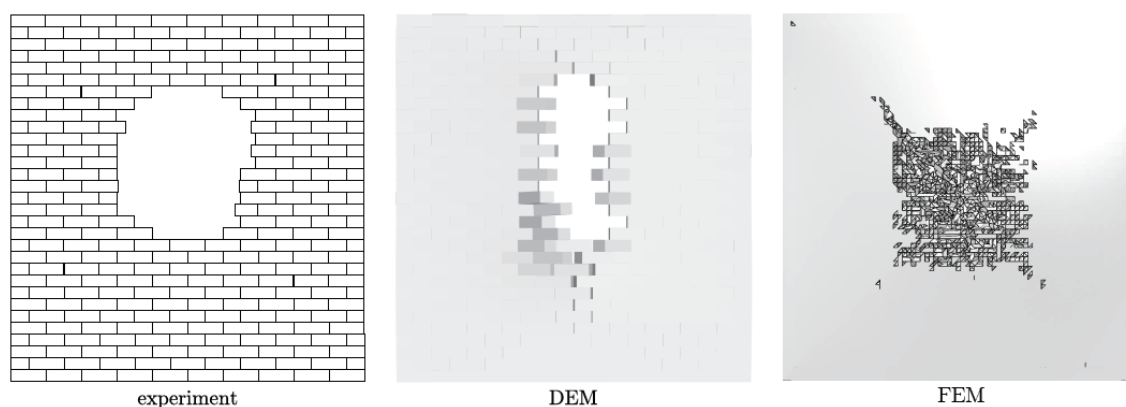


Figure 32. Comparison between experimental, numerical (DEM), and numerical (FEM) results (Masi, 2020).

4.1.2 Concrete Damage Plasticity

The Concrete Damage Plasticity (CDP) model, which is available in the Abaqus software, is a modification of the Drucker-Prager model made by Lubliner et al. (1989) and Lee and Fenves (1998). In the CDP model, the shape of the failure surface does not need to be circular; instead, the shape of the failure surface in the deviatoric plane is governed by the parameter K_c (Figure 33). This modification parameter K_c is the ratio of the distances between the hydrostatic axis, and the compression meridian and the tension meridian, respectively, in the deviatoric plane. The ratio defined by parameter K_c will always be greater than 0.5; when the ratio is 1, the deviatoric cross-section of the failure surface is circular (Kmieciak & Kamiński, 2011). This model represents the inelastic and fracture behaviour of the material by the concept of isotropic damage evolution combined with isotropic tensile and compressive plasticity. This model also assumes that damage plasticity characterizes the failure for tensile cracking and compressive crushing of the material. Additionally, it allows the definition of the

strain softening in tension and strain hardening in compression. The stress-strain curves in tension and compression can be seen in Figure 34.

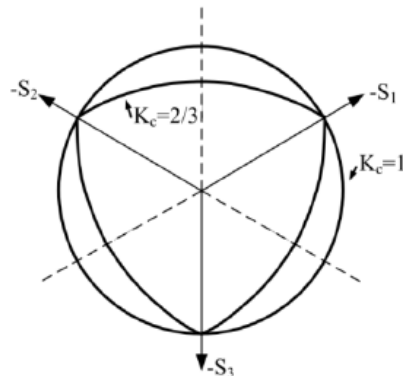


Figure 33. CDP failure surface, represented in the deviatoric plane S_1 , S_2 , and S_3 (Kmieciak & Kamiński, 2011).

To use this constitutive model in Abaqus, the following parameters are required: density, Young's modulus, compressive strength, fracture energy in compression, tensile strength, and fracture energy in tension. To ensure mesh-independent results, the fracture energy should be divided by a factor related to the element volume, where the factor is named the characteristic length or the crack bandwidth (Lourenço et al., 2018). For linear elements in Abaqus, the crack bandwidth is considered the element size. The Abaqus software requires additional parameters to be defined for the CDP model, namely: dilation angle, flow potential eccentricity, ratio of initial equibiaxial compressive yield stress to the initial uniaxial compressive yield stress, and viscosity parameter. The values for these parameters have been suggested in the Abaqus user's manual. Again, Pereira (2014) has used the CDP model for masonry buildings under blast loading. This material model has been employed also by Bhosale and Desai (2019) in the modelling of masonry walls, and Bui et al. (2019) for rammed earth constructions under seismic events. Altaee et al. (2020) and Huan et al. (2008) have used the CDP model for concrete members subjected to high strain rates corresponding to impact and blast loading.

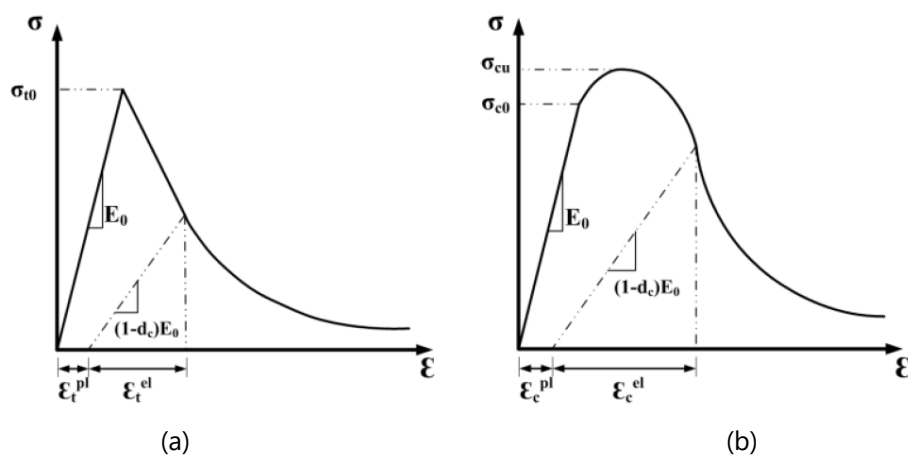


Figure 34. Stress-strain curves: (a) in tension; (b) in compression (Lubliner et al., 1989).

4.1.3 Material Behaviour at High Strain Rates

The type of load applied on a structure can significantly affect its response. Blast loads can produce very high strain rates, in the range of 10^2 to 10^4 s^{-1} , when acting on a structure. Impact loads can also cause high strain rates in the range of 10^0 to 10^2 s^{-1} . This high strain rate (or loading rate) alters the dynamic mechanical properties of the structure, consequently changing the predicted damage and capacity on many of the structure's elements (Ngo et al., 2007). The expected strain rates for various loading conditions can be seen in Figure 35. When concrete is subject to high strain rate dynamic loading conditions, it shows vastly different mechanical properties than concrete under static loading. The increase of strength can be accounted for by a dynamic increase factor (DIF), which describes the factor of the material properties under dynamic loading compared to the properties under static loading. When analyzing a structure, the correct dynamic increase factor must be selected to properly estimate the response. For example, the use of a DIF to increase the strength and the Young's Modulus of the material would lead to a reduction in displacement of a structure with respect to a static reference (Pereira, 2014). The underestimation of the DIF would lead to the overestimation of the displacement in the structure.

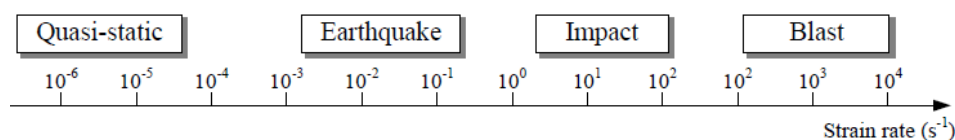


Figure 35. Expected strain rates for different types of loading (Ngo et al., 2007).

For masonry and earthen constructions, existing literature is scarce. Hao and Tarasov (2008) have conducted an experimental study of masonry under dynamic uniaxial compression by means of a Triaxial Static-Dynamic Testing machine. This study found that at a strain rate of 150 s^{-1} , the DIF for the compressive strength of approximately 2.3, the DIF for the ultimate strain was approximately 1.12, and the DIF of the Young's modulus was approximately 1.95. Burnett et al. (2007) conducted dynamic tensile experiments on a mortar joint using a Split Hopkinson pressure bar. At a strain rate of 1 s^{-1} , the dynamic increase of the mortar's tensile strength was 3.1. Using a modified Hopkinson bar and a Hydro-Pneumatic machine, Asprone et al. (2009) found that the tensile strength of a specific Italian stone increased by approximately three times. Pereira (2014) conducted an experimental campaign to determine the influence of the strain rates ranging between 2 s^{-1} to 200 s^{-1} on the mechanical properties of masonry using a drop weight tower. The data was acquired using both load cell acquisition and fast-cam video. A schematic of the test setup can be seen in Figure 36. Impact tests under uniaxial compression were performed to obtain stress-strain relations. The mechanical properties for each test were determined and the dynamic increase factors were calculated as a function of the strain rate. The specimens in this campaign included brick specimens, mortar specimens, and masonry specimens.

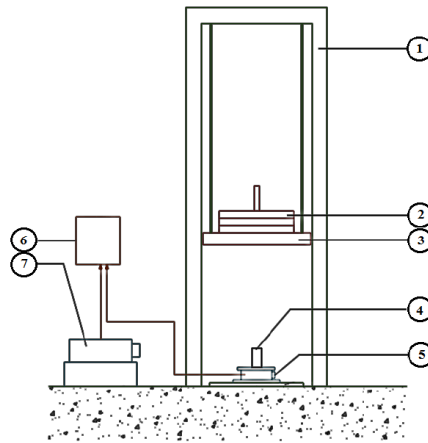


Figure 36. Schematic of the test setup used by Pereira (2014): (1) drop-weight tower; (2) additional masses; (3) hammer; (4) test specimen; (5) load cell; (6) acquisition system; (7) fast-cam video.

This study concluded the following empirical relations for brick masonry and mortar. The compressive strength of brick masonry, σ_c , as a function of the strain rate, $\dot{\epsilon}$, can be expressed as follows:

$$DIF(\sigma_c) = \begin{cases} 1, & 1E - 5s^{-1} < \dot{\epsilon} < 3s^{-1} \\ 0.2798 \ln(\dot{\epsilon}) + 0.6863, & 3s^{-1} < \dot{\epsilon} < 200s^{-1} \end{cases} \quad \text{Equation 36}$$

The Young's modulus, E , as a function of the strain rate, $\dot{\epsilon}$, for brick masonry can be expressed as follows:

$$DIF(E) = \begin{cases} 1, & 1E - 5s^{-1} < \dot{\epsilon} < 1.7s^{-1} \\ 0.2409 \ln(\dot{\epsilon}) + 0.8701, & 1.7s^{-1} < \dot{\epsilon} < 200s^{-1} \end{cases} \quad \text{Equation 37}$$

The compressive strength of mortar, σ_c , as a function of the strain rate, $\dot{\epsilon}$, can be expressed as follows:

$$DIF(\sigma_c) = \begin{cases} 1, & 1E - 5s^{-1} < \dot{\epsilon} < 4.35s^{-1} \\ 0.8166 \ln(\dot{\epsilon}) - 2.005, & 4.35s^{-1} < \dot{\epsilon} < 200s^{-1} \end{cases} \quad \text{Equation 38}$$

The Young's modulus, E , as a function of the strain rate, $\dot{\epsilon}$, for mortar can be expressed as follows:

$$DIF(E) = \begin{cases} 1, & 1E - 5s^{-1} < \dot{\epsilon} < 4.35s^{-1} \\ 0.5275 \ln(\dot{\epsilon}) + 0.2245, & 4.35s^{-1} < \dot{\epsilon} < 200s^{-1} \end{cases} \quad \text{Equation 39}$$

4.1.4 Contact Interactions

The Mohr-Coulomb was adopted here to model the sliding failure on the frictional interfaces between the individual blocks. When modelling contact interactions using the Mohr-Coulomb criterion in Abaqus, the model assumes non-associative flow since the interaction does not work within the plasticity framework. As such, the dilatancy angle in the model is automatically assigned a value of 0 degrees. The value of zero dilatancy was kept to model the contact interaction between the rammed earth material in line with works from previous authors (Shrestha et al., 2020) (Lourenço & Ramos, 2004). Using a dilation angle of zero will produce more conservative results because the strength of

the model increases with an increase in the dilation angle (Godio et al., 2018). In Abaqus, cohesion using the Mohr-Coulomb failure criterion cannot be modelled; thus, cohesion was considered negligible for this problem. Numerous authors have proposed values to model this interaction for earthen construction (Table 6). For the friction coefficient, an average value of 0.73 was taken. With respect to the normal and tangent stiffness, the values were selected according to Shrestha et al. (2020).

Table 6. Interaction properties.

Source	Friction Coefficient	Normal Stiffness $K_{n,joint}$	Tangent Stiffness $K_{s,joint}$
(Bui et al., 2020)	0.58	2.50e+8 kN/m ³	9.84e+7 kN/m ³
(Shrestha et al., 2020)	0.80	1.50e+8 kN/m ³	7.50e+7 kN/m ³
(Wangmo et al., 2019)	0.80	2.20e+10 kN/m ³	9.56e+9 kN/m ³
(El-Nabouch et al., 2018b)	(0.70-0.76)	-	-

When modelling using contact elements for sections of the wall, the joint stiffness must be accounted for to ensure the same wall stiffness is used for the model with continuum elements and discontinuum elements. To account for the joint stiffness, the Young's Modulus of the masonry unit could be found using the equation below (Lourenço et al., 2005):

$$K_{n,joint} = \frac{1}{h \left(\frac{1}{E_{wall}} - \frac{1}{E_{stone}} \right)} \quad \text{Equation 40}$$

where $K_{n,joint}$ is the joint stiffness in the normal direction, h is the height of the stone, E_{wall} is the Young's Modulus of the wall, and E_{stone} is the Young's Modulus of the stone. Using the normal joint stiffness defined by Shrestha et al. (2020) mentioned in Section 4.1.4, the Young's Modulus of the stone was calculated as 1.116×10^9 kN/m², without dynamic increase factors.

4.2 Torre de la Vela

The geometry used to model the *Torre de la Vela* in Abaqus was provided in AutoCAD 3D format by Vuoto (2020). As the Abaqus software does not have built-in units, consistent units had to be implemented at the creation of the model to ensure that all data is imported into the model correctly and so that all outputs can be interpreted properly. The units used in this model are shown in Table 7. From the AutoCAD format, the individual features were exported as *.igs files, and imported into Abaqus as individual parts (Figure 37). Once in Abaqus, the parts were all added as instances into the assembly, and then merged to create a single instance. This merge procedure allowed the prevention of unconnected regions in the model when running an analysis. In total, 124 parts were imported into Abaqus from AutoCAD. Boundary conditions were assigned to the structure in Abaqus (Figure 38) based on modal calibration conducted by Vuoto (2020). Pinned supports were added to the surface of the base of the structure and to a portion of the south-east corner, located underground. Lateral supports in the x-direction were assigned to a portion of the East façade connected to one of the walls in the *Alcazaba* (Section 2.3).

Table 7. Unit system used in Abaqus.

Length	Force	Mass	Time	Stress	Energy	Density
m	kN	T	s	kPa	kJ	T/m ³

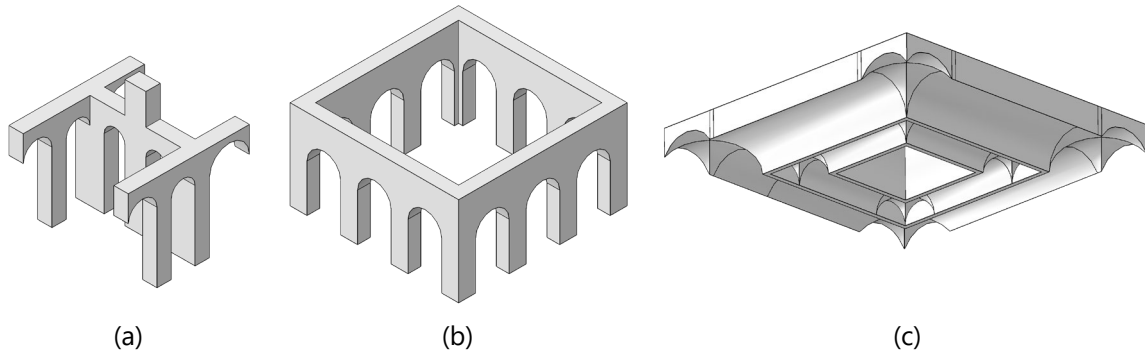


Figure 37. Example of parts imported into Abaqus: (a) inner nave; (b) outer nave; and (c) floor.

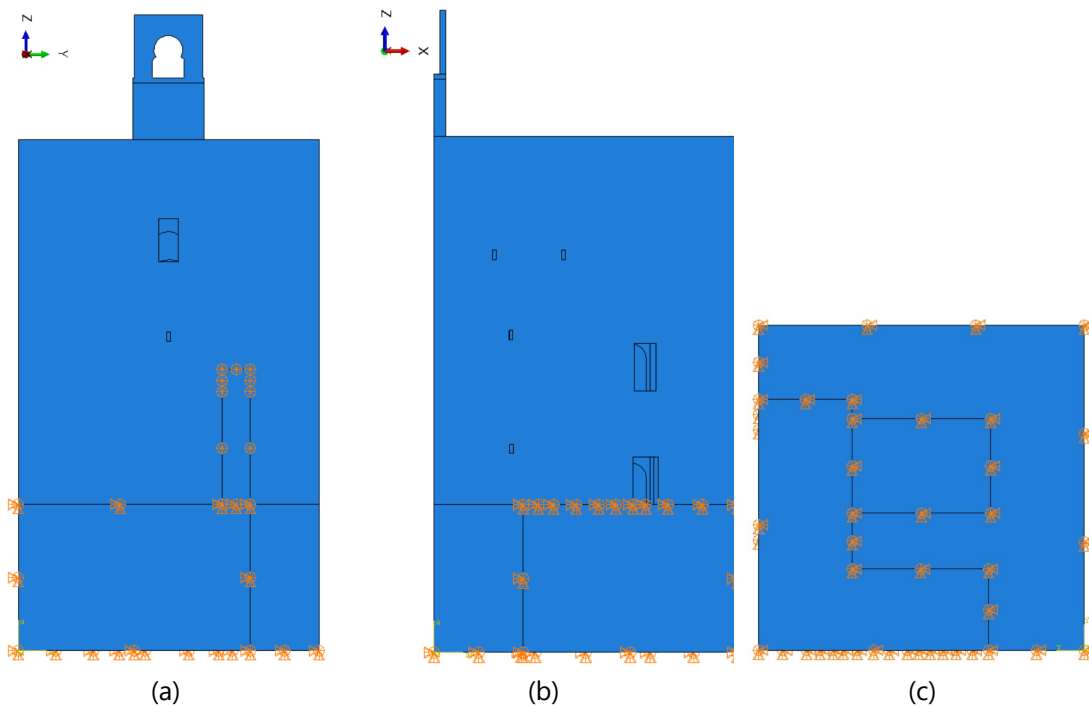


Figure 38. Boundary Conditions: (a) East façade; (b) South façade; (c) Bottom.

4.2.1 Finite Element Mesh

The geometrical model in Abaqus was discretized into a Finite Element mesh. As the computational effort increases significantly with the number of elements, different structural sections were assigned varying element sizes to keep the number of elements reasonable while maintaining the accuracy of the geometry (Figure 39). The model of the full building had 268,000 elements and 409,501 nodes in total, resulting in 1,228,503 degrees of freedom. The exact sizes and number of the elements varied according to the analysis performed, the location of the load, and the level of accuracy required. Thus,

the sizes presented in Table 8 are a baseline and are not the exact size for each model used. The volume elements in the full model were built with general purpose tetrahedron pyramidal elements (C3D10), which are ten-node, four triangular faces, quadratic solid elements (Figure 40a). This was due to the irregularity of the structure's geometry. Tetrahedron elements are less sensitive to the initial element shape compared to hexagonal elements (ABAQUS, 2010). In the models for the simplified South façade (Section 5.1.3), 8-node linear hexagonal brick elements with reduced integration (C3D8R) were used in the model (Figure 40b).

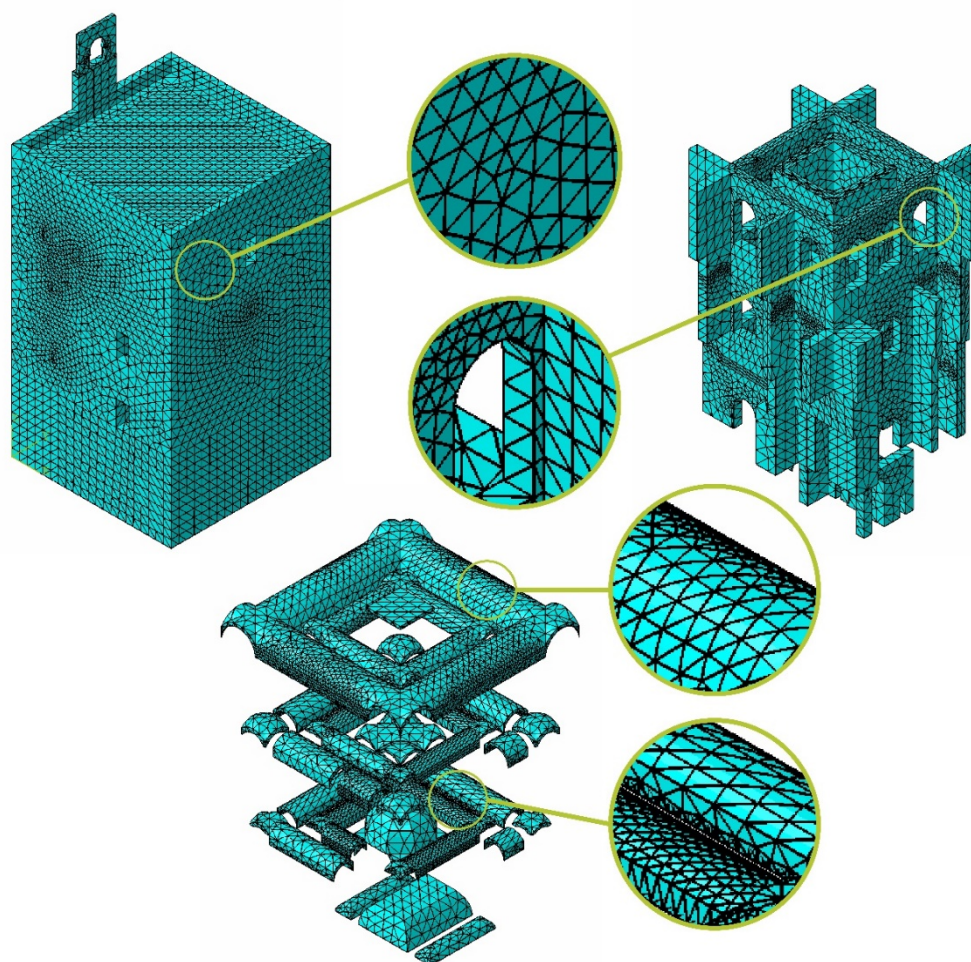


Figure 39. Mesh of the *Torre de la Vela* model in Abaqus.

Table 8. Element sizes.

	Global/Local Seed Size [m]	Curvature Control, h/L	Minimum Size Control [fraction]
<i>Exterior Walls/Gable</i>	0.80	0.10	0.10
<i>Corners/Naves/Connections</i>	0.60	0.05	0.50
<i>Slabs</i>	0.60	0.05	0.10
<i>Vaults</i>	0.30	0.05	0.50
<i>Single Vault (3rd Floor)</i>	0.80	0.05	0.01

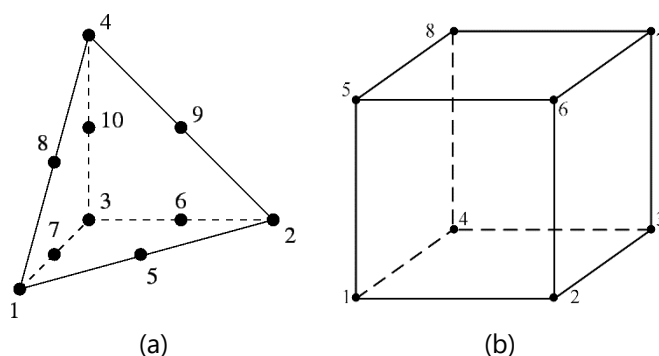


Figure 40. Elements: (a) tetrahedron pyramidal element (C3D10); (b) hexagonal brick element (C3D8R) (ABAQUS, 2010).

4.2.2 Material Properties and Material Model

The values for the material properties were obtained from previous work on the *Torre de la Vela* conducted by Vuoto (2020). The mechanical parameters used for the solid bricks and lime mortar masonry were determined based on the NTC 2018 and related *Circolare* (2019). The mechanical properties of the rammed earth (*tapial calicostrado*), of the infill used above the arches and of the brick masonry in the vaults were based on the Villegas (2012) approach. The assumptions for the material properties of the *tapial calicostrado*, the brick masonry, and the infill can be seen in detail in Vuoto (2020). Dynamic and sonic testing conducted by Vuoto and Ortega in September 2020 enabled the attainability of more accurate Young’s Modulus values for the rammed earth on all levels of the tower. The Young’s Modulus, E , Poisson’s ratio, ν , density, ρ , compressive strength, σ_c , tensile strength, σ_t , and fracture energies, G_{fc} and G_{ft} , used in this numerical campaign can be seen in Table 9.

Table 9. Material properties of the rammed earth, brick masonry, and infill used in the analysis of the *Torre de la Vela*.

Properties	Material			
	Rammed Earth		Brick Masonry	Infill
	Level 1	Other Floors		
E [kN/m ²]	5.90E+06	1.10E+06	1.60E+06	0.60E+06
ν [-]	0.30	0.30	0.25	0.30
ρ [T/m ³]	2.25	2.25	1.60	2.25
σ_c [kN/m ²]	2500	2500	4000	2500
G_{fc} [kN/m]	4.00	4.00	6.40	4.00
σ_t [kN/m ²]	300	300	200	300
G_{ft} [kN/m]	0.017	0.017	0.013	0.017

The dynamic increase factors were calculated using Equation 36 through Equation 39 while assuming a strain rate of 100 s⁻¹. Equations for the DIF of mortar (Equation 3 and 4) were used to obtain the DIF of rammed earth since the dynamic behaviour of rammed earth is unavailable. This is because the composition of earthen materials and mortar is similar, and the static mechanical behaviour is similar as well (Meyer, 2013). In the same line of thought, data is unavailable for the dynamic behaviour of

masonry and rammed earth under tension. For this reason, the dynamic increase factor for the tensile strength of the materials is assumed to be the same as the DIF for the compressive strength. The DIFs for the brick masonry, rammed earth, and infill, can be seen in Table 10.

Table 10. Dynamic increase factors for the brick masonry, the rammed earth, and the infill under blast loading.

Material Property	DIF	
	Brick Masonry	Rammed Earth and Infill
E	1.98	2.65
σ_c	1.97	1.76
σ_t	1.97	1.76

Subsequently, the DIFs were multiplied by their respective material properties, and the resulting material properties can be seen in Table 11. With respect to the fracture energy in compression, the fracture energy was obtained using the new value of compressive strength and a ductility index, d , of 1.6 mm, according to the following equation:

$$d = \frac{\sigma_c}{G_{fc}} \quad \text{Equation 41}$$

where the compressive strength, σ_c , is in MPa, and the fracture energy, G_{fc} , is in kN/m. The fracture energy in tension was recalculated using the new values of tensile strength in the following equation (Lourenço, 2009):

$$G_{ft} = 0.04 \cdot \sigma_t^{0.7} \quad \text{Equation 42}$$

where the tensile strength, σ_t , is in MPa, and the fracture energy, G_{ft} , is in kN/m.

Table 11. Updated material properties using DIFs.

Properties (with DIFs)	Material			
	Rammed Earth		Brick Masonry	Infill
	Level 1	Other Floors		
E [kN/m ²]	1.57E+07	2.92E+06	4.25E+06	1.59E+06
ν [-]	0.30	0.30	0.25	0.30
ρ [T/m ³]	2.25	2.25	1.60	2.25
σ_c [kN/m ²]	4390	4390	7020	4390
G_{fc} [kN/m]	7.02	7.02	11.24	7.02
σ_t [kN/m ²]	527	527	351	527
G_{ft} [kN/m]	0.026	0.026	0.019	0.026

The material model adopted was the Concrete Damaged Plasticity (CDP), as stated above. The values in Table 12 were suggested by previous authors to be used for the required parameters (Abdelmoneim

Elamin Mohamad & Chen, 2016). Additionally, a damage criterion was defined for all the materials in tension. A damage parameter of 0.95 in tension was assigned to all the materials at their respective maximum tensile strain.

Table 12. Suggested parameters by the Abaqus User's Manual (Abdelmoneim Elamin Mohamad & Chen, 2016).

Parameter	Value
Dilation angle (Ψ')	34°
Eccentricity (ϵ_c)	0.10
Strength Ratio (f_{b0}/f_{c0})	1.16
Modification Parameter (K_c)	0.67
Viscosity parameter (μ_v)	0.001

Stress-strain diagrams were required to define the compressive and tensile behaviour in Abaqus. To obtain these, a single-element cube was created in Diana, corresponding to each of the four materials present in the *Torre de la Vela*. The materials were modelled using the Total Strain-Based Crack Model (TSBC) which followed a smeared crack approach for the fracture energy. This material model describes both the compressive and tensile behaviour, and the stress-strain relationship can be idealized using different approaches. To be consistent with previous works (Vuoto, 2020), the parabolic stress-strain law was selected for compressive behaviour, and the exponential stress-strain law was selected for tensile behaviour. The corresponding curves can be seen in Figure 41 (DIANA FEA BV, 2020). The element size of $1 \times 1 \times 1$ cm was meshed with a single element corresponding to its geometry and was tested both in compression and in tension to obtain the stress-strain relation of the material (Figure 42).

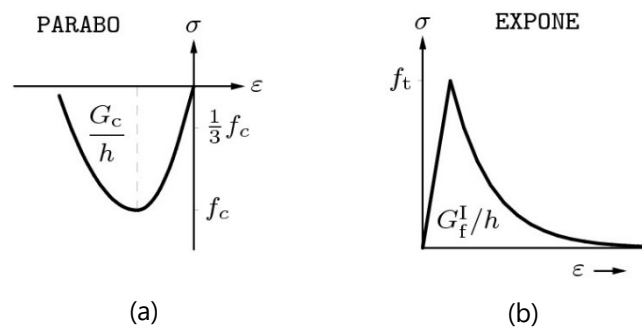


Figure 41. Assumed behaviour for the materials in: (a) Compression; (b) Tension (DIANA FEA BV, 2020).

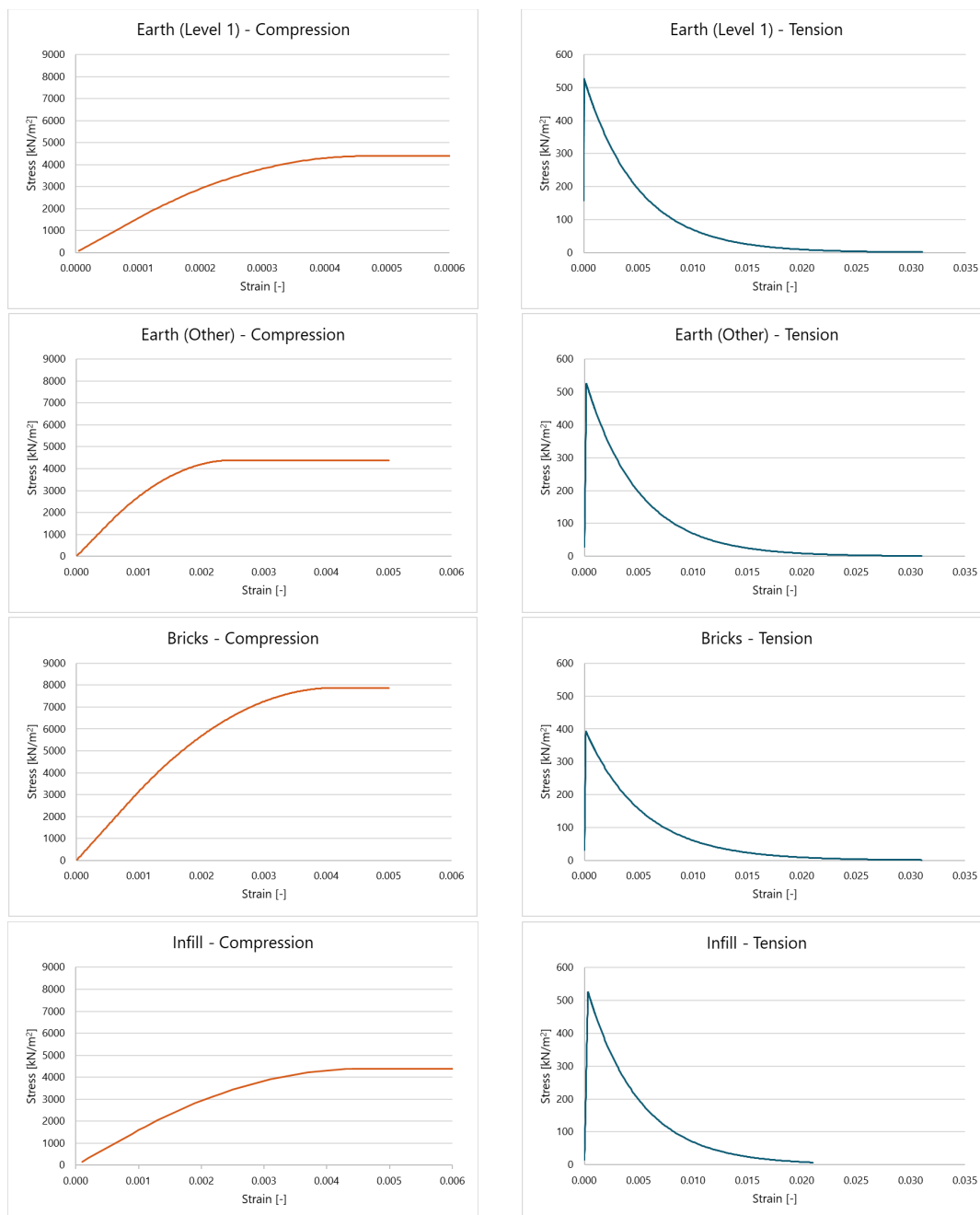


Figure 42. Compression and tension stress-strain extracted from Diana.

4.3 Model Validation

The model created in Abaqus had to be validated using the existing information on the *Torre de la Vela* to confirm the accuracy of the model. This involved checking the mass of the model against the model in AutoCAD, and conducting an eigenvalue analysis to validate the model against the existing Diana model provided by Vuoto (2020). A linear static analysis using the self-weight of the structure was performed to compare the mass of the model in Abaqus with the mass of the AutoCAD model obtained using hand calculations. The linear static analysis also enabled the detection of any potential errors in the structural model. Based on this analysis (Table 13), no difference in the self-weight was noted and the two models were in accordance with each other.

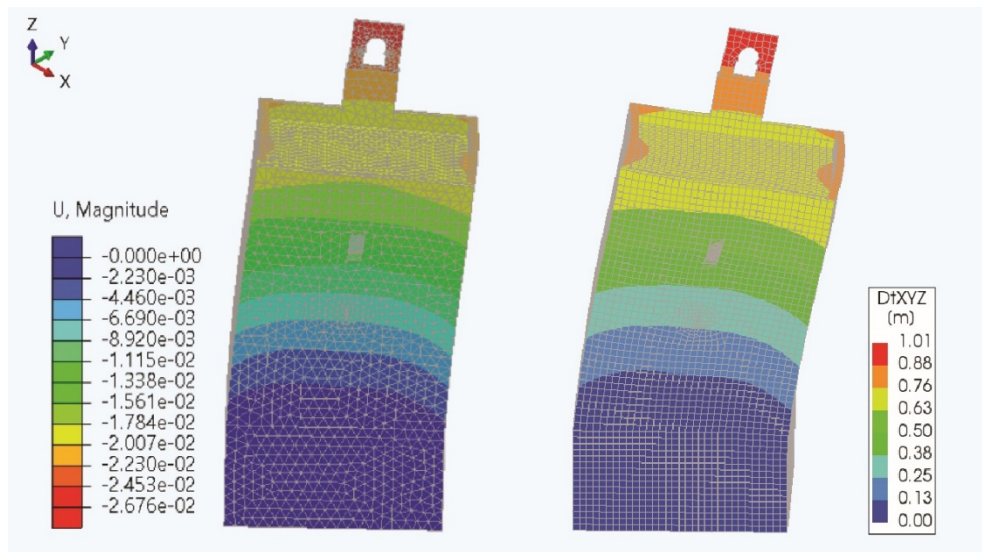
Table 13. Comparison between the expected mass from the AutoCAD model and the results from the Abaqus Model.

	AutoCAD Model		Numerical Model		Percentage Error [%]
	Volume [m³]	Density [T/m³]	Mass [T]	Mass [T]	
Rammed Earth	3955.30	2.25	8899.43	8899.43	0.000%
Brick Masonry	602.72	1.60	964.35	969.37	0.521%
Infill	528.55	2.25	1189.24	1189.25	0.001%
			11,053.03	11,058.05	0.045%

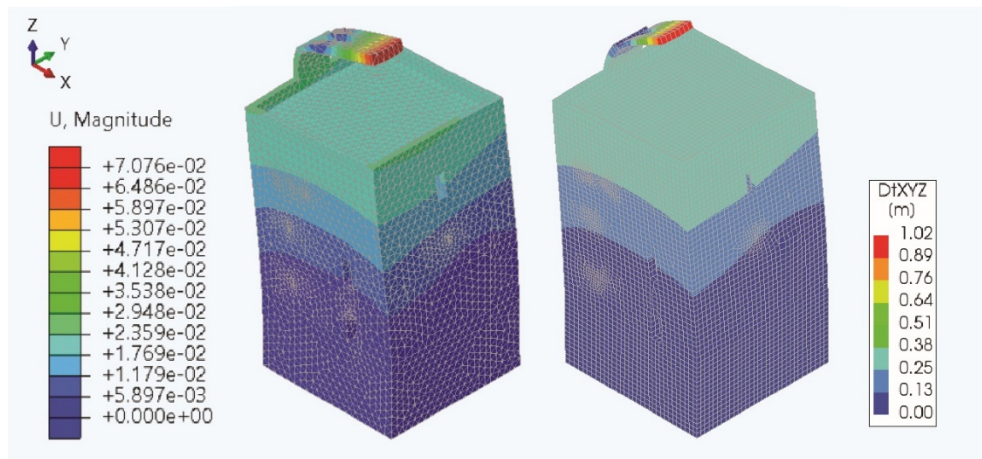
As a previous model of the *Torre de la Vela* already existed in Diana, this presented an opportunity to validate the newly developed model in Abaqus. To do so, an eigenvalue analysis was performed on both the Abaqus model and the Diana model. Similar global modes could be identified between the two models based on their frequencies, which can be seen in Table 14. The mode shapes of the two models further confirms their similarity (Figure 43). Here, the absolute values of displacements should be ignored as the modes merely indicate a shape with any multiplication factor being possible. In Diana, modes are normalized to a maximum value of 1, while in Abaqus they are not. The mode shapes on the left of Figure 43 correspond to the results from Abaqus, while those on the right correspond to the results from Diana. As seen below, Mode 2 represents a global translational mode in the y-direction (Figure 43a), Mode 3 represents a global translational mode in the x-direction (Figure 43b), mostly local at the belfry, and Mode 4 represents a global torsional mode (Figure 43c). It is evident from Figure 43, modes 2, 3, and 4 are nearly identical between the two models, thus validating the Abaqus model with the Diana model. It is noted that mode 1 is not considered as this mode was considered a local mode.

Table 14. Global modes for the *Torre de la Vela* obtained by eigenvalue analysis.

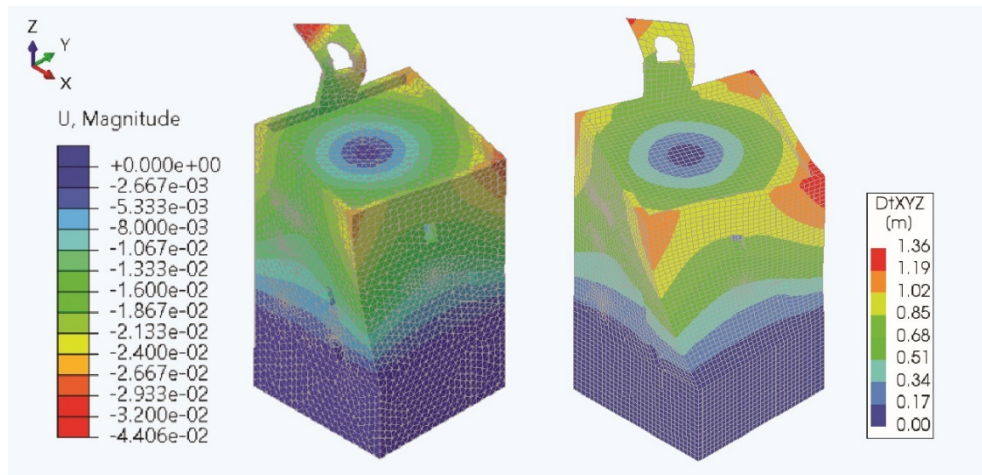
Mode	Frequency (Abaqus)	Frequency (Diana)	Percent Error [%]	Mode Shape
2	3.2396 Hz	3.2577 Hz	0.556%	Translation (y-axis)
3	3.5136 Hz	3.5450 Hz	0.886%	Translation (x-axis)
4	5.1693 Hz	5.1986 Hz	0.564%	Torsional



(a)



(b)



(c)

Figure 43. Eigenmodes comparison between the Abaqus model (left) and the Diana model (right) provided by Vuoto (2020). The modes compared are: (a) Mode 2; (b) Mode 3; (c) Mode 4.

CHAPTER 5

5 BLAST LOADING

In recent years, a number of explosions, both accidental and intentional, have made the headlines. These incidents, which include the Port of Beirut explosion (2020), the Lyon Bombing (2019), and the Sri Lanka Easter bombings (2019), caused significant loss of life and economic impact. Blasts occurring near or inside a building can damage and destroy parts of the building by producing local and global responses related to different failure modes. As such, the vulnerability of masonry envelopes under blast loading is critical to investigate and understand, as it can lead to the potential loss of life. This chapter will present the loading conditions and the results for exterior blast loading and interior blast loading. The global response of the building and the local response of individual structural members will be investigated. A comparison between the use of continuum elements and contact elements to simulate the behaviour of the structure will be made. Finally, the effect of the mesh size on the damage will be investigated.

5.1 External Blast Loading

The loading scenario studied in this analysis corresponded to four barrels of black powder (around 110 kg TNT). This assumption is based on the number of barrels that could be transported at the same moment for storage, and the position of the explosives was selected based on the possible route of transportation from the outside of the building to the inside for storage purposes. Thus, the explosive was placed at 4 m from the entrance on Level 3, on the south side of the building (Figure 44). The blast loading in this problem was defined as pressure profiles. The profiles acting on the surfaces were calculated based on the position and mass (in equivalent TNT) of the explosive.

5.1.1 Loading Definition

As the South façade, where the load is closest to, is quite large, this was divided into four sections: S1, S2, S3, and S4, as seen in Figure 44. The black surfaces in the model correspond to locations where the blast would not hit the surface. At the bottom corners, this corresponds to the location where the building is below ground level. The black surfaces around the South entrance and on the East side of the building correspond to where the *Torre de la Vela* is connected to the bridge and to the wall of the *Alcazaba*. These different sections also had different standoff distances: RS1, RS2, RS3, and RS4. The standoff distance for the top of the building, and the East and West façades were taken as the distance to the closest edge plus 8 m, corresponding to half of the width of the building. The standoff distance for the North façade was considered as the distance of the explosive to the front façade plus the entire length of the building. For the top of the building (T), and the East (E), West (W), and North (N) façades, the pressure profile was considered as constant throughout the respective façade. The loads on the bell gable were ignored to simplify the problem. The equations used to calculate the peak side-on overpressure (Equation 10), reflected pressure (Equation 18), arrival time (Equation 20), and duration (Equation 22), can be seen in Chapter 3. The pressure profiles for this loading scenario can be seen in Figure 45 for 110 kg of TNT at 4 m from the entrance of the building. The analysis was run for a

duration of 0.62 s, corresponding to two times the natural period of the structure, to allow for sufficient dissipation of energy.

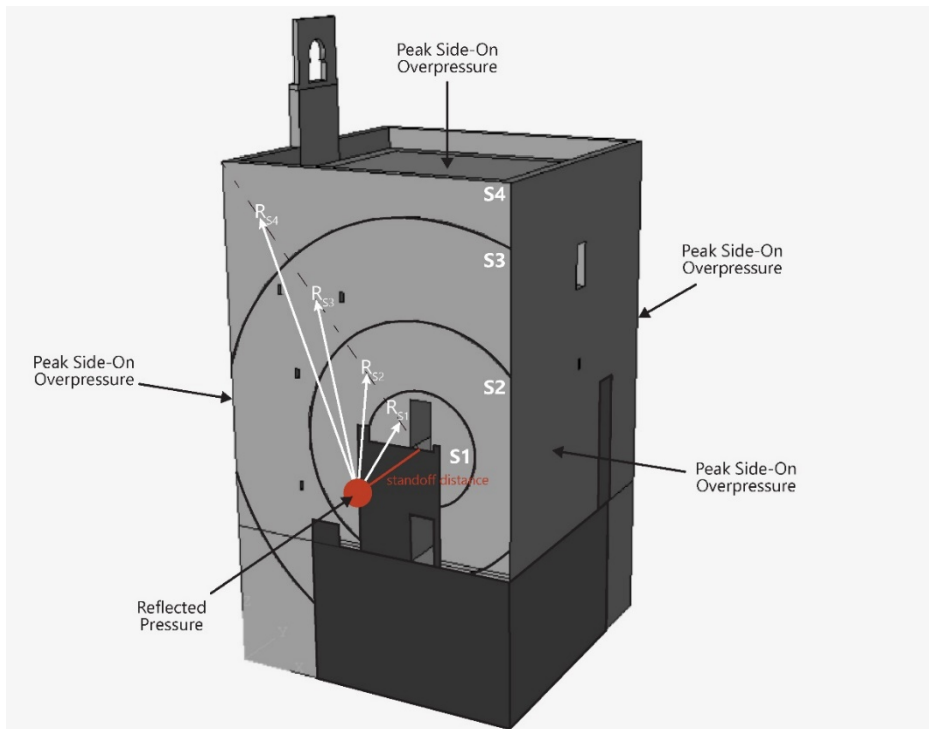


Figure 44. Location of blast loading on the exterior of the *Torre de la Vela*.

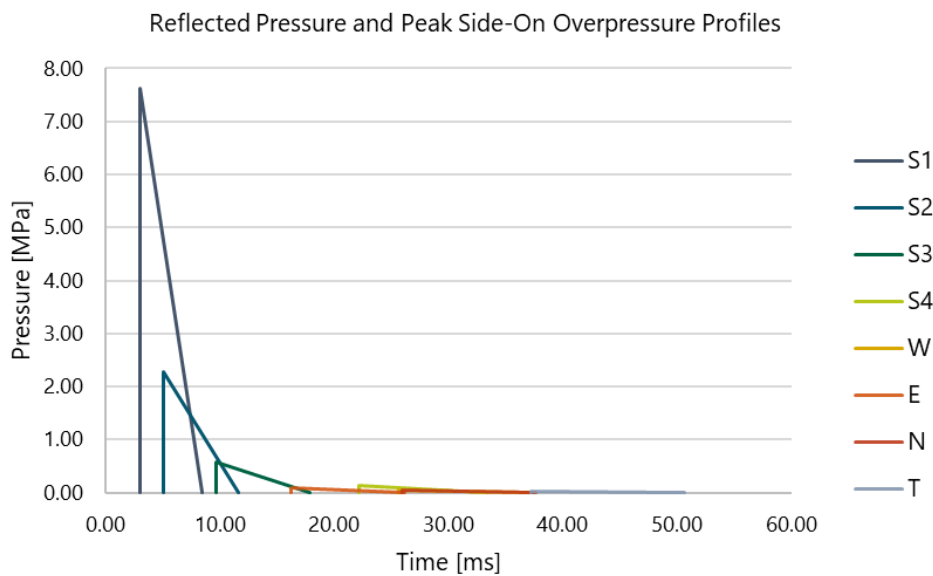


Figure 45. Pressure profiles acting on the *Torre de la Vela* for 110 kg TNT at 4 m.

5.1.2 Exterior Blast Results on Whole Building

After conducting the nonlinear analysis in Abaqus/Explicit, results of displacements, stresses, and strains could be obtained. The damage to the building could also be determined. In Figure 46, the

displacement time history in the North-South direction, corresponding to the direction of the blast, is plotted for the top corners of the building and shows the building continues to oscillate for approximately three cycles until the end of the analysis. Standard viscous damping is adopted, which may be somewhat low for the results obtained. A stronger movement in the structural elements in a given loading direction, as shown also below in this work, is typically expected during a blast analysis. The largest displacement in the direction of the blast at the corners is 1.44 cm at the southeast corner at 0.33 s. Here, the displacements on the north side of the building are greater than those on the South. Figure 47 shows the deformed shape time history in the *Torre de la Vela*, further emphasizing the displacement occurring in the north side rather than the south side. The bell gable in this plot has been removed as the local displacement of the bell gable is much greater than the global displacement of the structure. The oscillation of the building over time is also visible in Figure 47. The maximum displacement in the direction of the blast is 4.26 cm, occurring at 0.03 s in the inside of the door where the blast is being applied.



Figure 46. Displacement time history at the upper corners of the building in the North-South direction.

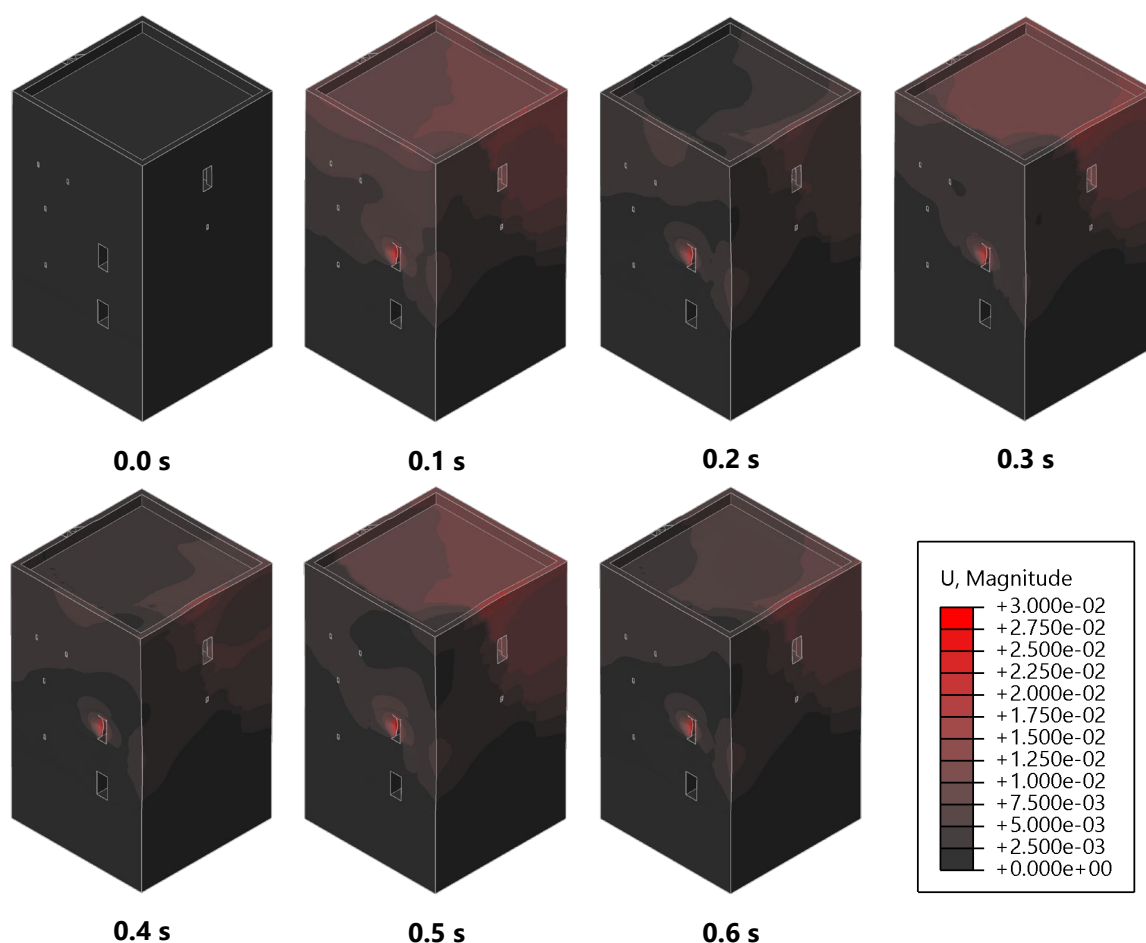


Figure 47. Deformed shape time history.

Next, the tensile stresses in the *Torre de la Vela* at the end of the analysis can be visualized. The tensile stresses (maximum principal stress) for the exterior of the building are plotted using 527 MPa as the maximum value, corresponding to the tensile strength of the rammed earth using dynamic increase factors (Figure 48a). The tensile stresses on the vaults and naves in the inside of the building are plotted with a maximum value of 394 MPa, representing the tensile strength of the brick masonry (Figure 48b). A larger concentration of tensile stresses is visible at the bottom of the South and East walls in Figure 48a, corresponding to the pinned part of the wall due to its location underground. This concentration of stress is likely caused by the displacement of the building moving in the y-direction. Concentrations of tensile stress are also visible on the roof of the *Torre de la Vela* (Figure 48a) and throughout the brick masonry in the inside of the building (Figure 48b). After the dissipation of energy, very few locations have tensile stresses in the range of the tensile strength. Similarly, the compressive stresses at the end of the analysis can be visualized. The compressive stresses (minimum principal stress) on the exterior of the building have been plotted with a minimum value of 4390 MPa, corresponding to the compressive strength of the rammed earth (Figure 49a). On the inside of the building, the compressive stresses were plotted with a minimum value of 7880 MPa, representing the compressive strength of the brick masonry (Figure 49b). On the South and East façades of the building, high concentrations of stresses can be seen at the locations where the boundary conditions change from pinned to unconstrained supports. Some low values of stress on the South façade are also visible,

likely caused by the pressure of the blast. In the interior of the building, the compressive stresses are negligible (Figure 49b).

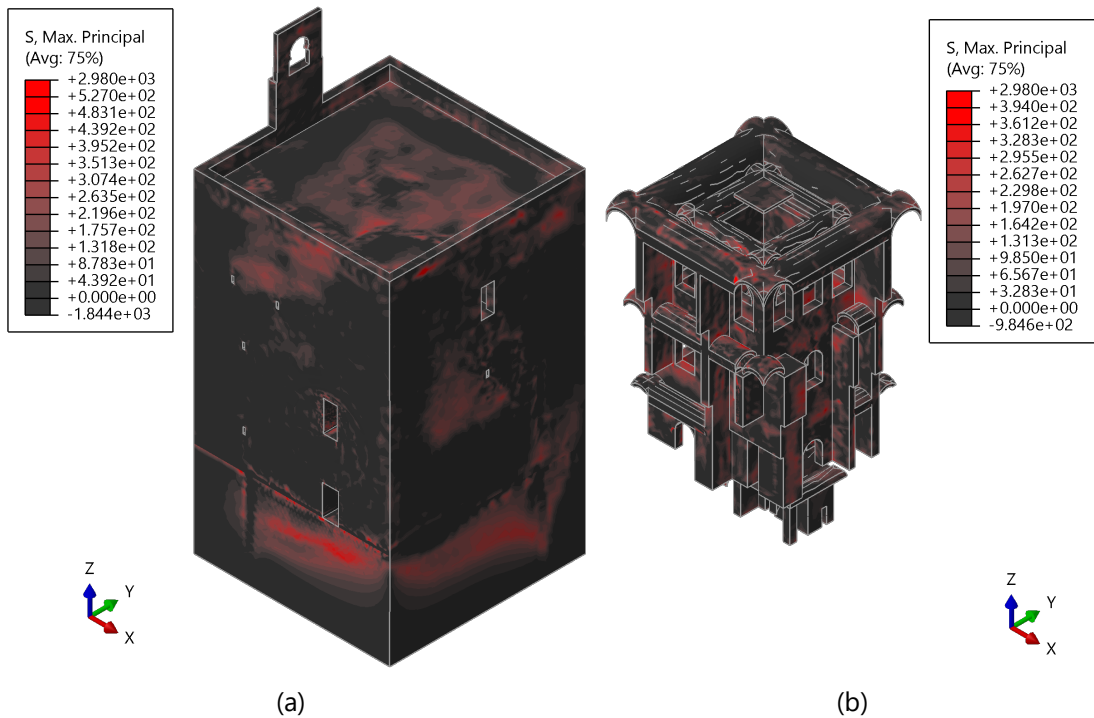


Figure 48. Tensile stress at 0.62 s: (a) Rammed earth exterior; (b) Brick masonry.

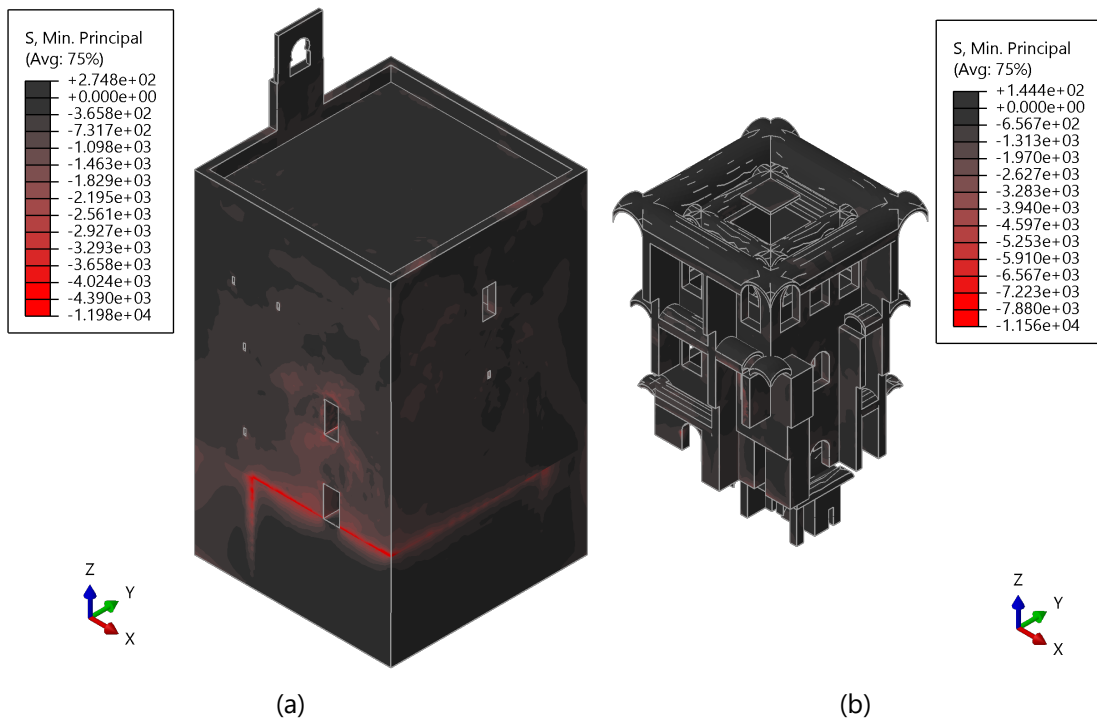


Figure 49. Compressive stress at 0.62 s: (a) Rammed earth exterior; (b) Brick masonry.

Since the compressive stress at the end of the analysis is so low, it is worth observing the compressive stress at critical points during the analysis. The magnitude of the displacement time history was plotted at the top of the entrance on Level 3 (Figure 50), which is the location where the blast load is applied. Critical points during the time history were chosen, as seen in the dots in Figure 50. The contour plots of the stresses at these critical points were plotted to better visualize the stresses occurring at these instances (Figure 51). The highest stresses initially occur around the location of the blast load (Figure 51a). While the building is oscillating, the highest locations of stress occur at the supports above Level 1 (Figure 51c).

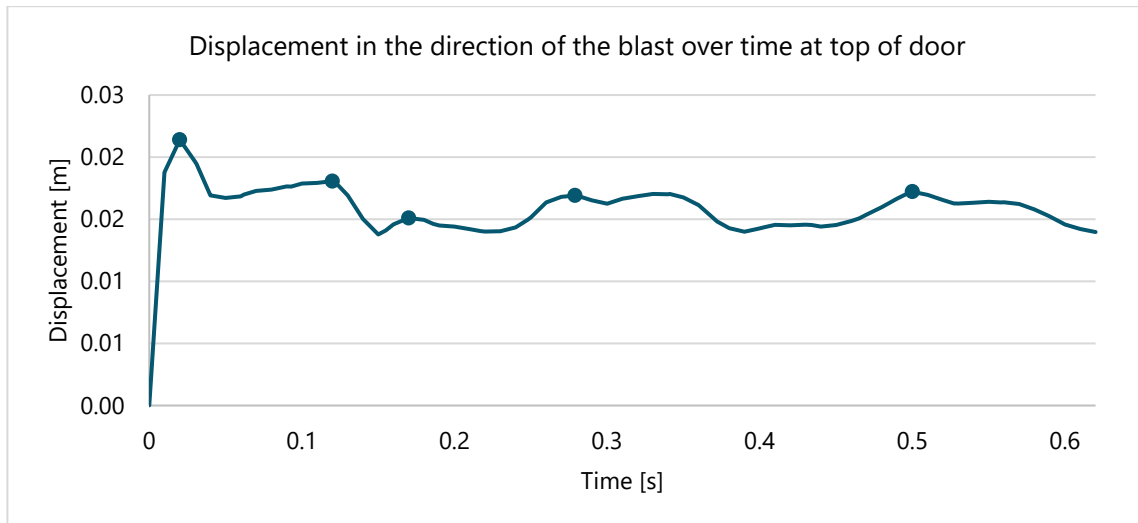


Figure 50. Time history of the displacement at the top of the entrance.

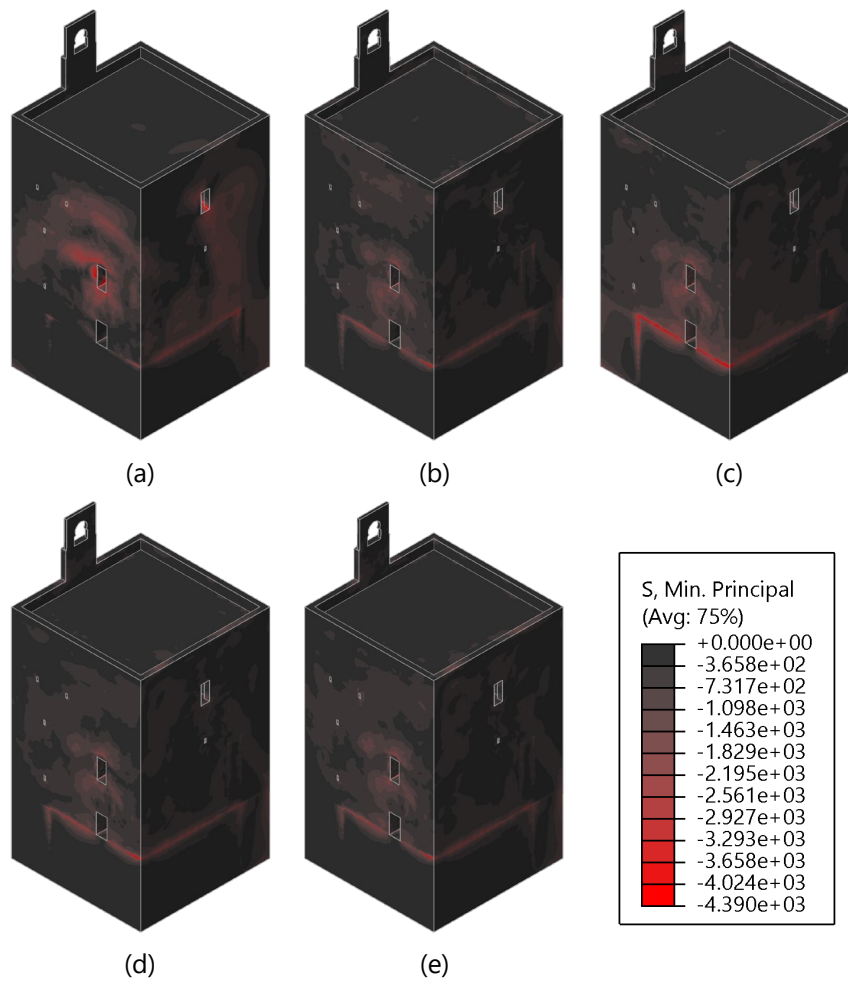


Figure 51. Compressive stress at different instances of the displacement history at the top of the entrance opening.

The tensile and compressive strains in the structure are presented to better understand which areas of the building may experience cracking or crushing. The tensile strains in the building are plotted, as seen in Figure 52a, for the exterior of the building and Figure 52b for the interior of the building. Cracking can be found around the entrance on Level 3, where the blast load is being applied. Some diagonal cracks can also be observed on the East façade, connected to a crack on the roof perpendicular to the blast. Additionally, significant cracking is present at the bell gable, which indicates a local failure. With respect to the interior of the building, shear cracks can be observed on the South vaults on Level 4, and radial cracking on the East vaults. These cracks correspond to the exterior cracks on the roof and the East façade. The outer brick masonry walls closest to the entrance of the building also show signs of cracking. The compressive strains in the building can be seen in Figure 53a, for the exterior of the building and Figure 53b for the interior of the building. Some crushing can be observed around the door where the blast load is being applied. On the interior of the building, crushing is also observable on the bell gable and at the base of the East vault on Level 4.

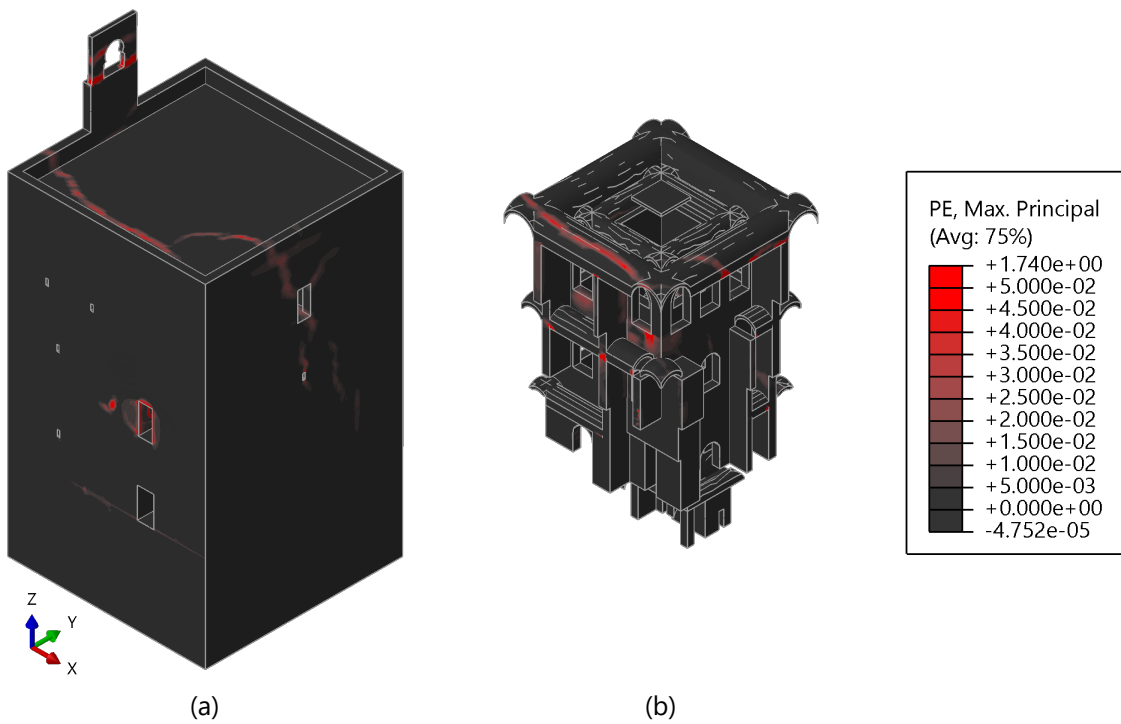


Figure 52. Tensile strain at 0.62 s: (a) exterior of the building; (b) interior of the building.

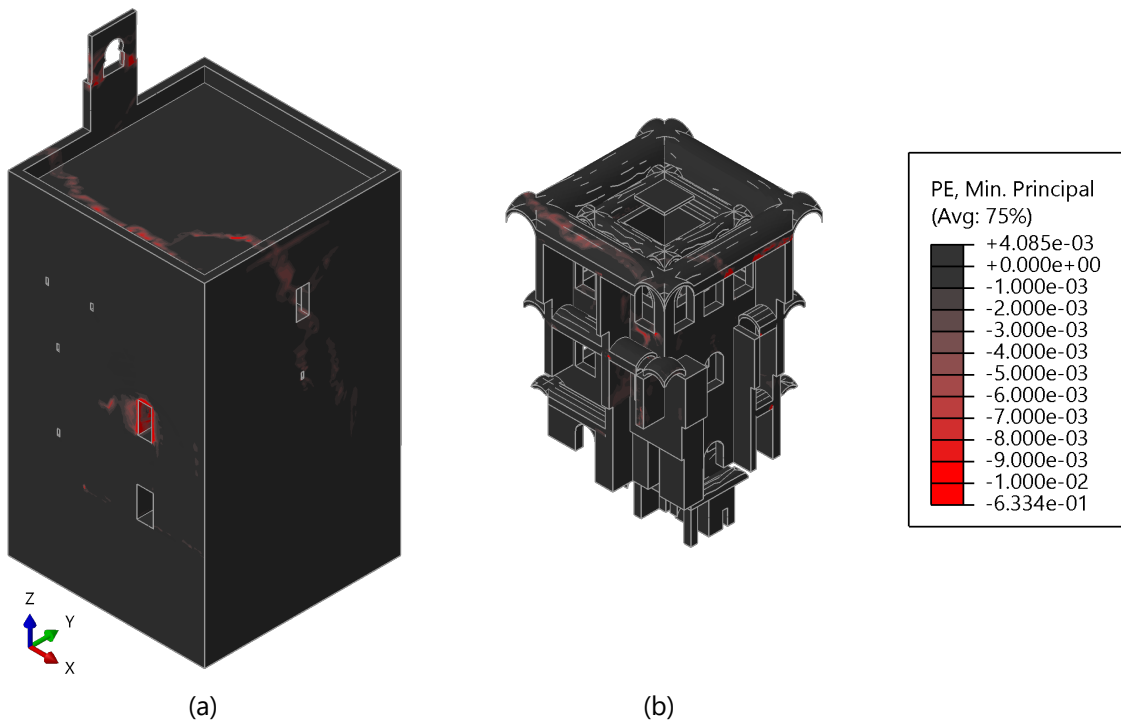


Figure 53. Compressive strain at 0.62 s: (a) exterior of the building; (b) interior of the building.

Due to the low slenderness of the walls resulting from their thickness, the damage defined by UFC (UFC 3-340-02, 2008), based on the maximum rotation at the supports, is not possible to use in this case study. Another approach had to be considered to understand the damage occurring in the building. Hoveidae et al. (2021) compared various damage indexes on an earthen masonry structure to

understand the damage state of the building and concluded that the most accurate damage index was the Failure Volume Index. The damage index based on the failure volume can be calculated as follows (Hoveidae et al., 2021):

$$DI = \frac{V_{fail}}{V_{total}} \times 100 \quad \text{Equation 43}$$

where V_{fail} represents the volume of elements with damage exceeding a certain threshold, and V_{total} represents the volume of all the elements in the structure.

The damage levels and damage indexes can be defined in Table 1, according to Asteris et al. (2014). Here, SD indicates Small Damage, MD indicates Medium Damage and HD indicates High Damage. For the *Torre de la Vela*, a damage threshold of 0.77 was selected, based on Hoveidae et al. (2021). The locations with damage greater than 0.77 are plotted in Figure 54. In the building, a total volume of 5087 m³ existed, with 76.8 m³ of damaged elements. Using the damage index calculation in Equation 43, the estimated damage index in the tower is 1.51% (Table 16). To conclude, the damage level in the *Torre de la Vela* is small for an explosive of 110 kg of TNT at 4 m from the building.

Table 15. Damage levels for the failure volume index (Asteris et al., 2014).

Description	Damage Level	DI Value
Minor cracking of veneers, no observable out-of-plane displacements	SD	DI < 10%
Extensive cracking, noticeable in-plane displacements, minor out-of-plane displacement	MD	10% < DI < 20%
Extensive cracking, noticeable in-plane and out-of-plane displacement. The building is near collapse	HD	DI > 20%

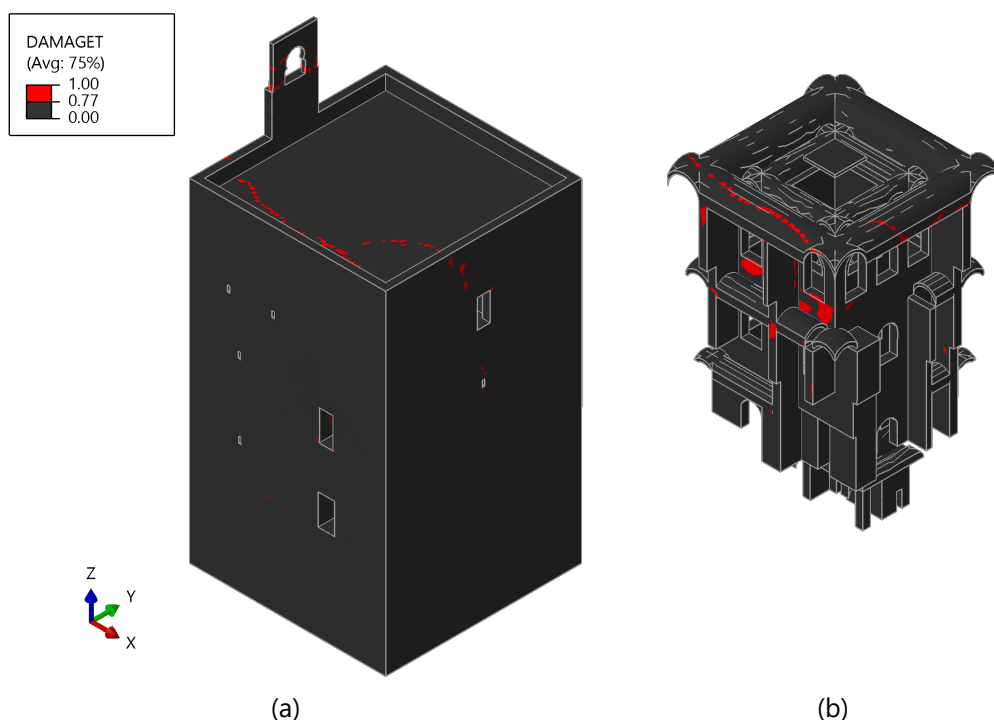


Figure 54. Damage in tension greater than 0.77.

Table 16. Estimated damage level, damage index, and volume of failed elements.

Damage level	Damage Index	V_{fail} [m ³]	V_{total} [m ³]
SD	0.86%	43.8	5087.7

5.1.3 Exterior Blast Results on Single Wall

Since the South façade was the location where the pressure from the explosion is the highest, it was interesting to better understand the behaviour of that façade. First, the wall was modelled separately from the rest of the building using a combined micro-macro modelling approach. Later, the wall was modelled separately using continuum elements. Springs were used to simulate the stiffness of the building portions being neglected (Figure 55). This wall was calibrated against the full model by changing the spring stiffness in the wall and comparing the displacement pattern in the building. When the displacement patterns at the end of the analysis were considered sufficiently close, the model of the single façade was considered as calibrated to the whole building model (Figure 56). To reduce the calibration time, only lateral loads without self-weight were used to cause the displacement in the models. However, the results of the whole building model and the single façade model presented later include the self-weight of the model.

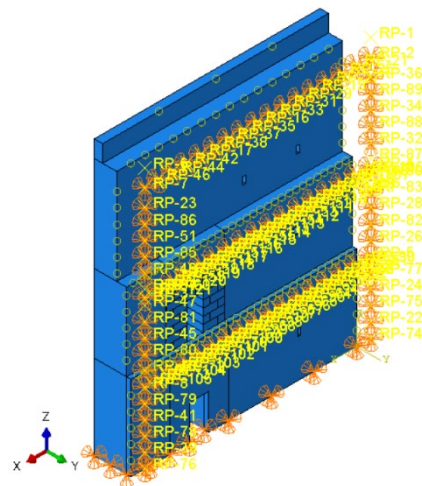


Figure 55. Boundary conditions on the south wall.

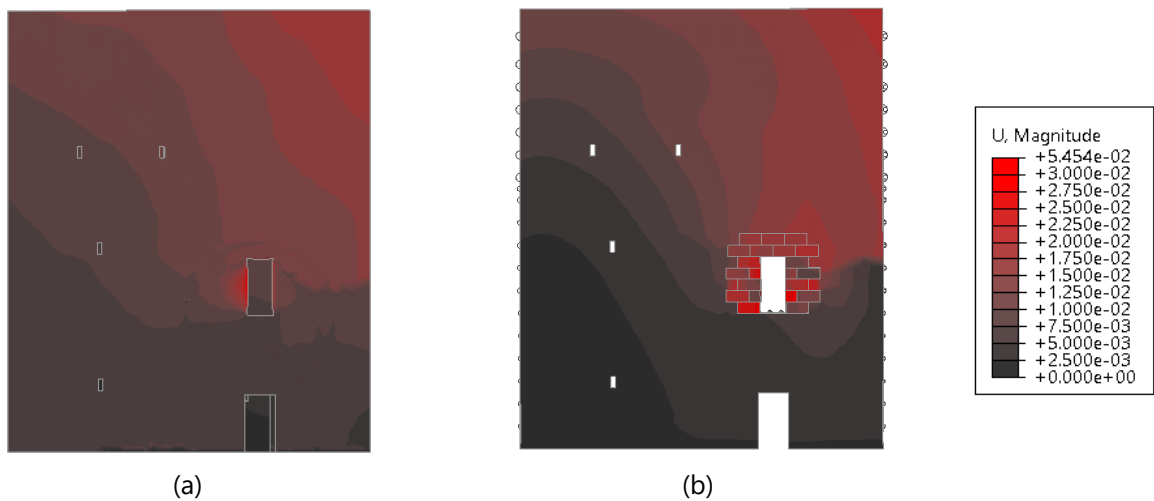


Figure 56. Comparison between the displacement at the front façade upon blast loading: (a) whole building model; (b) front façade model with springs.

The front façade of the *Torre de la Vela* was modelled using contact elements around the entrance of Level 3, corresponding to the location of maximum displacements on the façade. The purpose of using contact elements in this region was to see their effect on the displacement occurring around the opening where the blast load is being applied. Furthermore, the effect of contact elements on the overall stress and strain distribution can also be studied. The contact properties were modelled using “General Contact” in Abaqus. The interaction properties used to model the contact elements were discussed in Chapter 4. The maximum displacement in the direction of the blast in the contact model is 2.55 cm. When observing the contours in Figure 57a, the largest displacements occur on the lower portion surrounding the door. Displacement in the North-South direction can also be observed growing radially from the door throughout the whole façade. Most of the displacement occurs above the base of the door, and not below, as the pressure profile from the blast is not applied in that location due to the presence of the bridge.

When comparing the displacement between the full-building model and the model of the single exterior wall, more locations have significant displacements in the contact model, particularly around the lower portions of the door (Figure 57). Overall, the displacements on the façade of the whole building model are mostly localised above and around the door, which is a large contrast to the contact model with displacements throughout the façade. However, when comparing the values of the displacement in the North-South direction, the whole building model has displacement of 3.81 cm around the door, which is greater than the previously mentioned 2.55 cm in the contact model. The displacements at the supports, the sides of the wall, and the top of the wall are very similar between the two models (Figure 56). One of the reasons for the difference between these displacements could be due to the difference between the distribution of self-weight in the simplified model when compared to the full-building model. As the single wall model is a simplification, the distribution of the self-weight is different and consequently may allow for greater displacement in the direction of the blast.

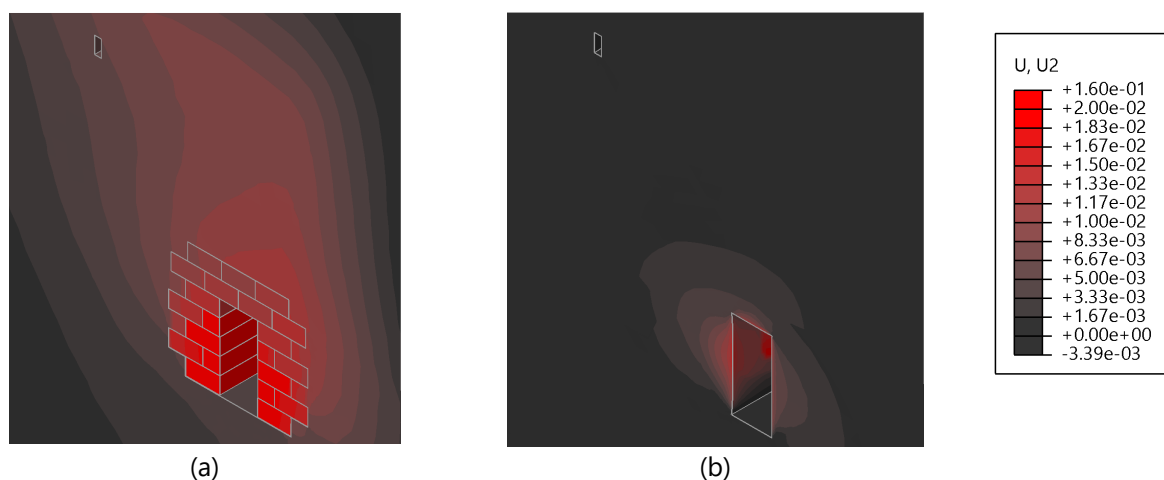


Figure 57. Displacement in the direction of the blast: (a) single exterior wall; (b) whole building model.

Next, the stress distributions in the façade of the contact model can be observed. The tensile stresses in the contact model can be seen Figure 58a, where the maximum tensile stress on the scale is 527 kN/m², corresponding to the tensile strength of the rammed earth. Tensile stresses on the contact model are distributed throughout the façade, with no tensile stress at the base of the wall and at the upper corners of the façade. The highest values of tensile stresses occur above the door, in the region where continuum elements are used. The tensile stresses of the whole building model have been plotted in Figure 58b to compare. In the contact model, the tensile stresses do not exceed the tensile strength of the rammed earth due to extrapolation of results to the nodes. However, the distribution of tensile stresses is quite different between the two models, due to sliding of the blocks. Overall, the whole building model has lower tensile stresses in the entire façade, with the highest concentrations of tensile stress being located at the top of the South façade. This is in contrast to the contact model, where the highest concentrations of tensile stress are located in the centre of the façade. The compressive stresses in the contact model can be seen in Figure 59a, where the minimum compressive stress on the scale is 4390 kN/m², corresponding to the compressive strength of the rammed earth. The compressive stresses on the contact model are very low, with the majority of compressive stresses

concentrated at the base of the wall near the supports. Low values of compressive stress are also located around the door, at the same locations where macro-modelling has been applied. The compressive stresses of the whole building have been plotted in Figure 59b to be compared with the contact model. As with the contact model, the highest concentrations of compressive stress are observed at the base of the wall where the supports are located, and gradually decrease through the height of the façade. The level of compressive stress is much greater in the whole building model than in the contact model, which, again, allows sliding of the blocks. Additionally, the compressive stress in the whole model at the base of the wall exceeds the compressive strength of the material, meaning crushing damage is expected in this region.

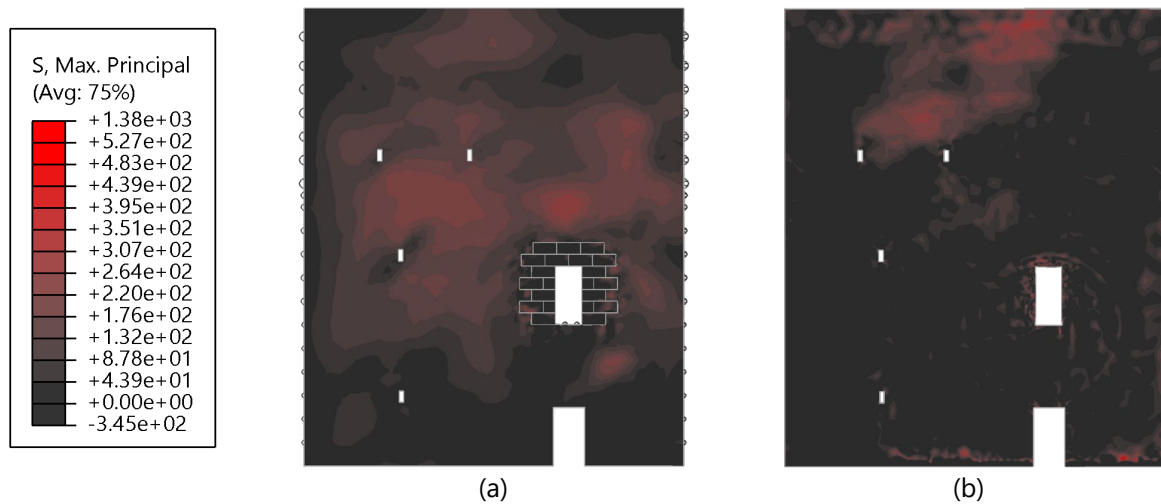


Figure 58. Tensile stresses in the front façade: (a) contact model; (b) whole building model.

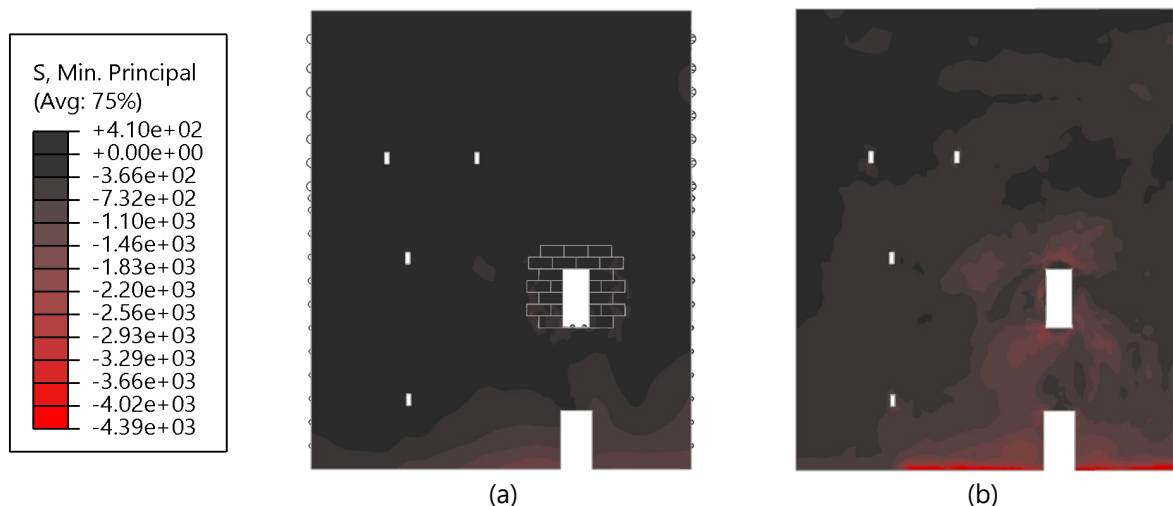


Figure 59. Compressive stresses in the front façade: (a) contact model; (b) whole building model.

The plastic strains can be observed for the contact model, but only in the locations of macro-modelling as the contact blocks are not strain-based. Nevertheless, the plastic strains still allow an understanding of the overall distribution of strains in the façade. Figure 60a shows the tensile strains in the contact model, plotted with a maximum tensile strain of 1%. Here, very high values of tensile strain

can be observed around the door, between the blocks where the continuum elements meet the contact blocks. Low values of tensile strain can also be observed at the base of the wall. When comparing the tensile strains in the contact model to those in the whole building model (Figure 60b), it is obvious that the tensile strains in the whole building model are much greater, particularly around the door. In the whole building model, some locations of tensile strain can also be noted at the base of the wall, and around the windows, which is greater than the strains observed in the contact model. The compressive strains in the contact model can be seen in Figure 61a, plotted with a minimum compressive strain of 1%. Here, the compressive strains in the façade are almost negligible, with only a few locations of compressive strain around the macro blocks. In contrast, the whole building model has high values of compressive strain around the door's opening, and around the door (Figure 61b). Evidently, the use of contact elements around the doors significantly reduces the overall strain in the façade when comparing the two plots.

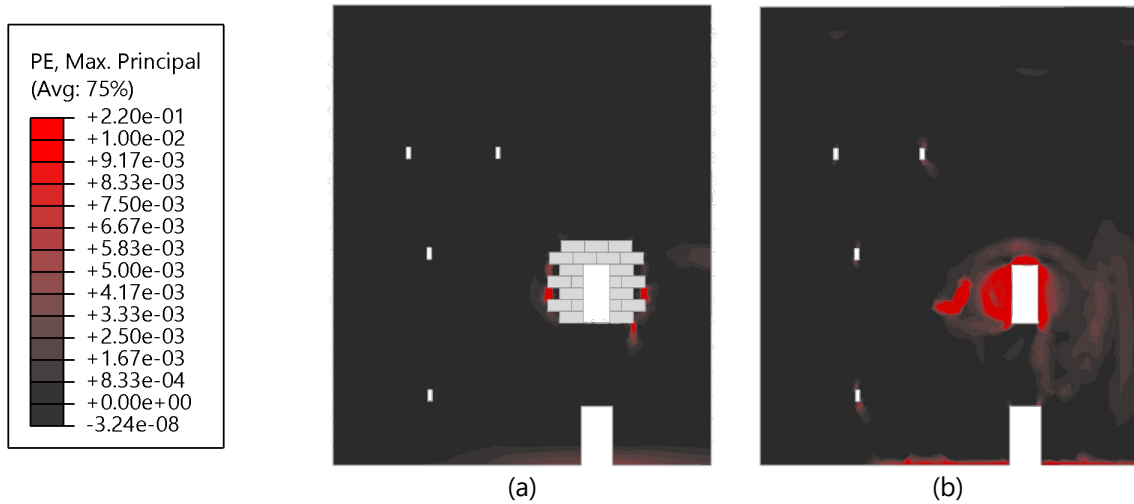


Figure 60. Tensile strains in the front façade: (a) contact model; (b) whole building model.

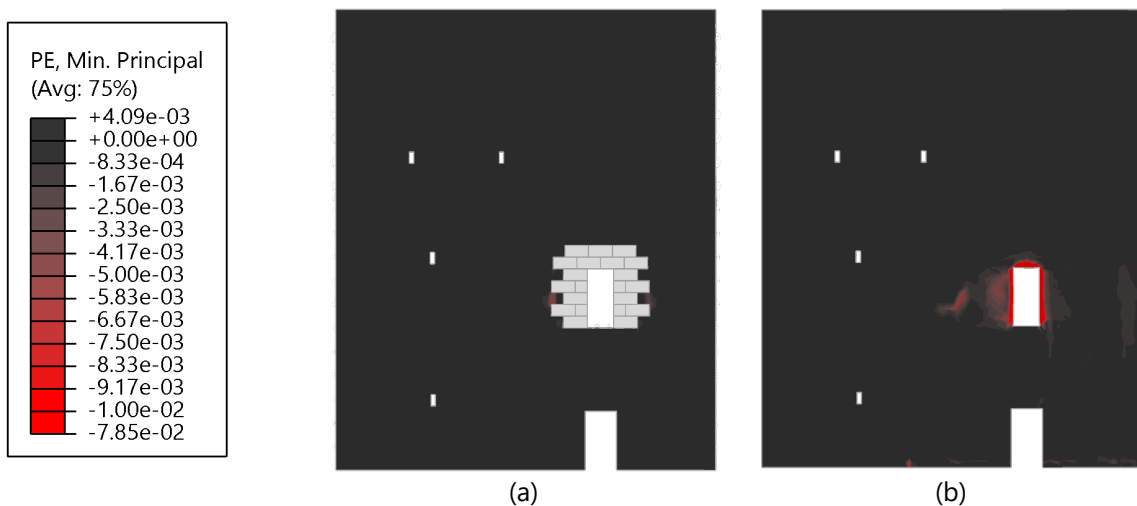


Figure 61. Compressive strains in the front façade: (a) contact model; (b) whole building model.

A final result is given considering the South façade modelled using only continuum elements, but with a feature available in Abaqus – removal of damaged elements. The elements which reach maximum

degradation can be removed from the model during the analysis. In Abaqus/Explicit, the element is removed from the mesh if the degradation reaches the maximum degradation at any single integration point in the element. This option allows to better understand what occurs at failure when the model is subjected to severe damage (ABAQUS, 2010). The advantage of this method is that highly distorted elements are removed from the calculation. In deleting damaged elements from the model during analysis, mass and energy is also removed from the system. Thus, in the case of substantial element deletion, the accuracy of the simulation will decrease. When using continuum elements, elements which exceeded a damage of 0.77 were removed from the model during the analysis, based on the damage criterion define by Hoveidae et al. (2021). As seen in Figure 62, damage is occurring around the opening where the blast is being applied, causing a hole in a circular pattern. Only the elements closest to the opening have exceeded the allowed damage, creating the appearance of a hole. Note that the damaged elements do not go through the entire thickness of the external wall. The distribution of tensile stresses on the façade were also plotted for the continuum model with damaged elements, as seen in Figure 63a. This stress distribution resembles that of the whole building model, seen in Figure 58a, where in both cases the highest values of tensile stress are located at the top of the façade. In the case of the simplified continuum model, the values of tensile stress overall are lower than that of the whole building model. With respect to the distribution of compressive stresses in the simplified continuum model, higher values of compressive stress are seen at the base of the wall, near the supports, and around the door (Figure 63b). This distribution is slightly different from those seen in the contact model (Figure 59a) and the whole building model (Figure 59b), but more closely resembles the distribution seen in the whole building model as compressive stresses are present around the door opening. The tensile and compressive strains in the simplified continuum model with damaged elements removed are negligible and are not displayed.



Figure 62. Front façade using continuum element, where elements exceeding the damage threshold have been removed.

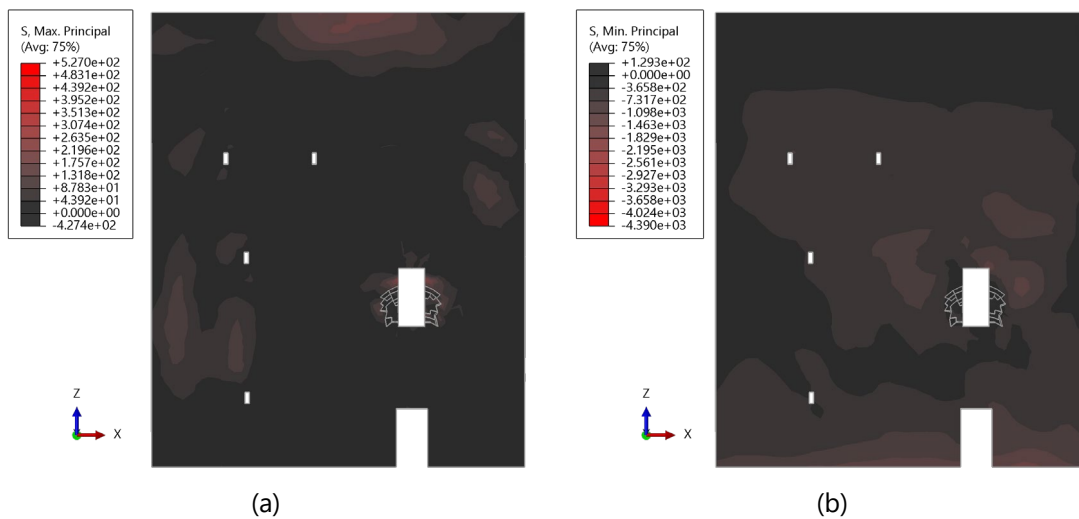


Figure 63. South façade of the simplified continuum model: (a) tensile stress; (b) compressive stress.

5.2 Internal Blast Loading

The loading scenario in this analysis corresponded to a quarter barrel of black powder (6.8 kg TNT). This explosive was placed in the North room on Level 2, close to the exterior wall. This location was assumed as an appropriate location for the storage of gunpowder, as the room is on the same level as one of the entrances, thus not requiring to be brought up a flight of stairs. The size of the barrel of gunpowder was selected based on standard sizes from historical documents (Griffiths, 1856). As with the previous scenario, the blast loading was defined as pressure profiles calculated by the position and mass of the explosive. The model of the *Torre de la Vela* was simplified to a single floor for the internal blast loading scenario to reduce the computation time of the analysis and because the damage is expected to be contained locally (Figure 64).

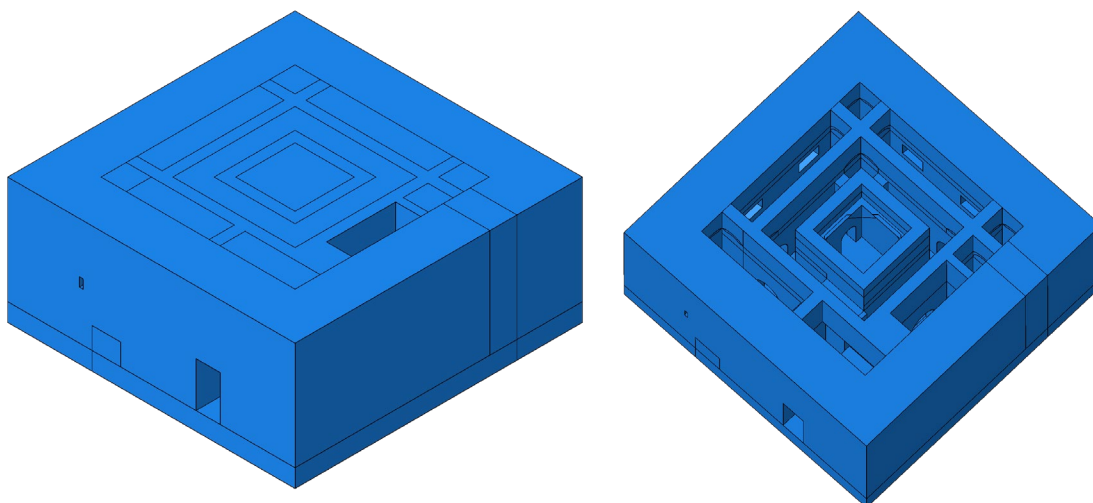


Figure 64. Simplified model of Level 2.

5.2.1 Loading Definition

The location of the explosive in the North room of the building can be seen in red dot in Figure 65. This location corresponds to the centre of the room at a distance of 0.4 m from the wall and 0.2 m above the ground. The plan of the *Torre de la Vela* had to be divided into different zones (Figure 65) to define the loading profiles. Only three zones were specified along the trajectory of the blast wave to simplify the problem, as the blast effects in other regions of the plan were assumed to be negligible. Within each zone, the surfaces on which the blast is acting were defined as: top, North, South, East, and West. The nomenclature of these surfaces can be seen in Figure 65. The loads acting on the floor were neglected as the base of the model was pinned in the vertical direction in the simplified model. Therefore, it was assumed that displacement in the vertical direction caused by blast loads acting on the floor would not occur. The distance between the centroid of each surface and the location of the explosive was used as the standoff distance. The equations used to calculate the peak side-on overpressure (Equation 10), reflected pressure (Equation 18), arrival time (Equation 20), and duration (Equation 22), can be seen in Chapter 3. The pressure profiles on the walls were calculated with the reflected pressure, which can be seen in Figure 66 per zone for this loading scenario. Since the blast is located internally, the reverberation effects needed to be taken into consideration. Previous studies have suggested that three pressure peaks be used per surface when accounting for these reverberation effects (Baker et al., 1980) (Cormie et al., 2011).

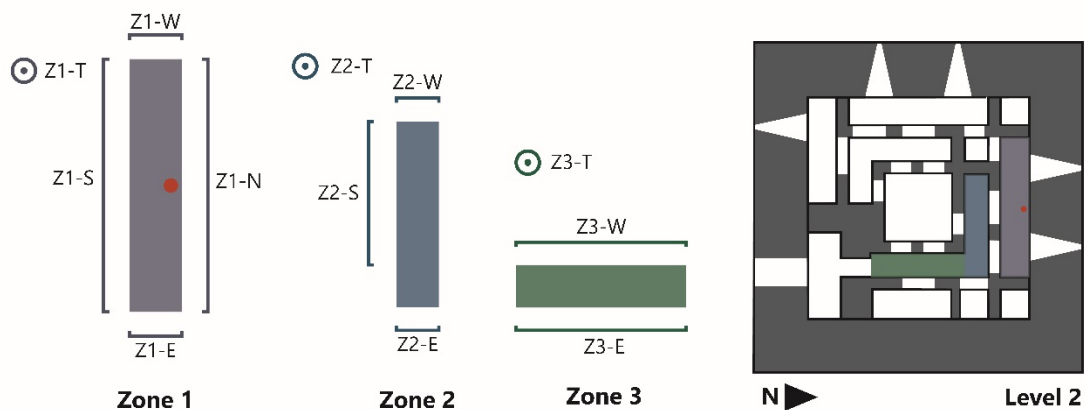
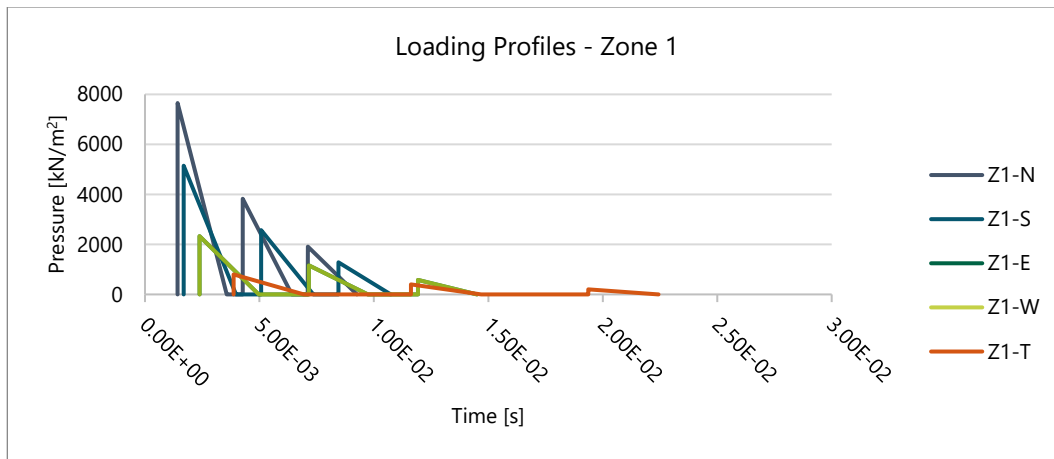
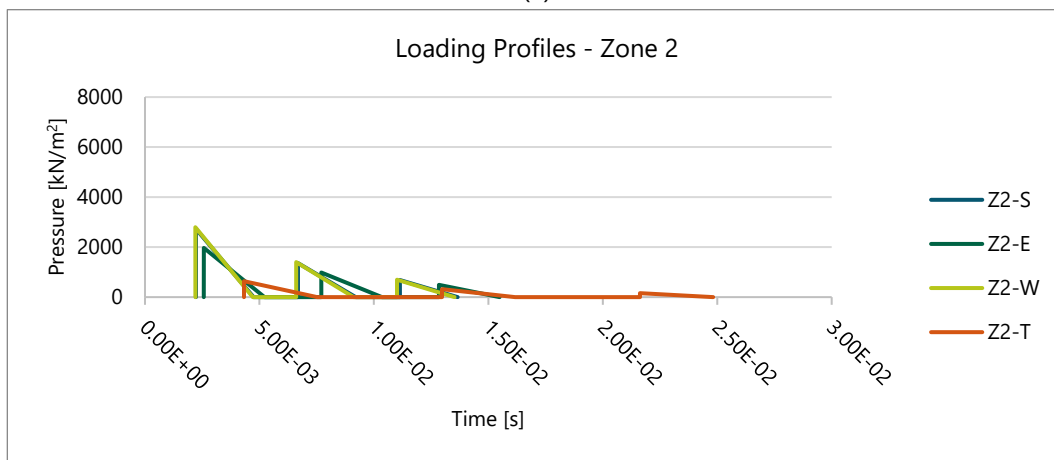


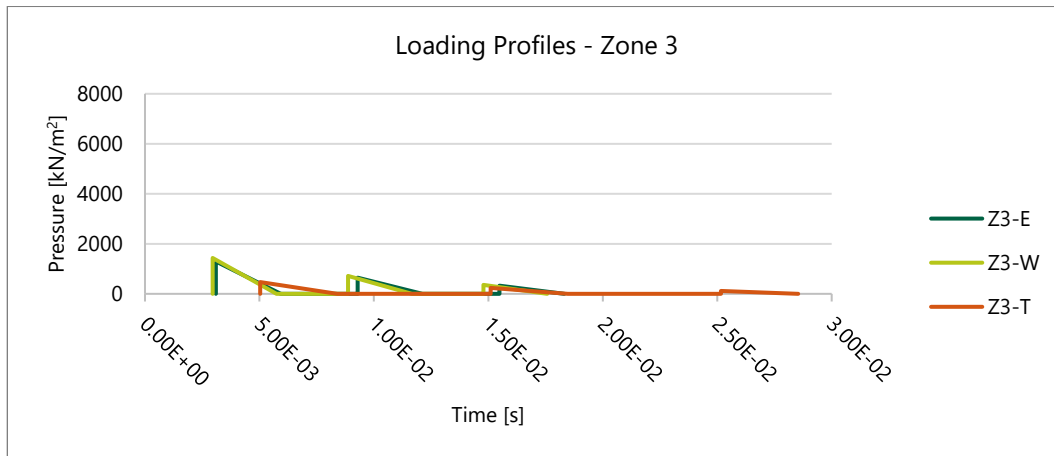
Figure 65. Zone locations for the interior blast.



(a)



(b)



(c)

Figure 66. Loading Profiles for: (a) Zone 1; (b) Zone 2; and (c) Zone 3.

5.2.2 Interior Blast Loading Results on Level 2

The nonlinear analysis in Abaqus/Explicit allows the viewing of results for displacement, stresses, and strains. The damage to the whole model and individual structural elements could also be determined using various methods. The displacement on wall Z1-S on Level 2 is excessive, with a deflection of

2.4 m at the end of the analysis (Figure 67). For this reason, the wall will be neglected when viewing the stresses and the strains on the model as it is assumed to be collapsed.

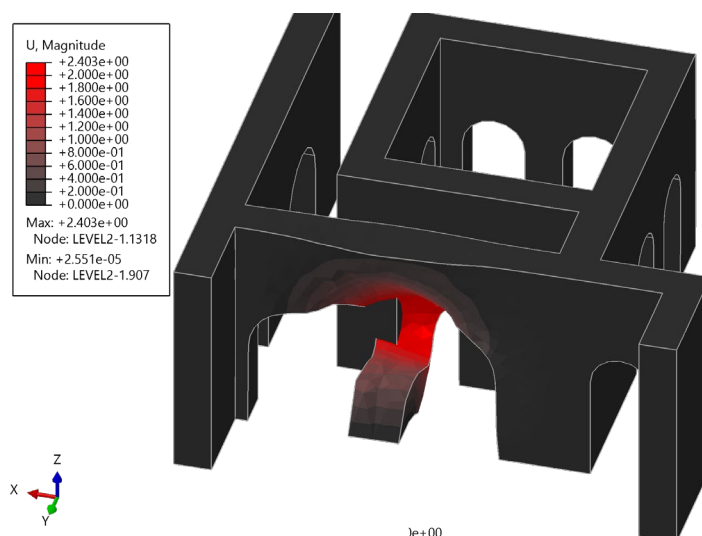


Figure 67. Excessive displacement on the wall.

The tensile stresses in the regions on which the blast is being applied can be seen in Figure 68, allowing the tensile failure of the material to be checked. These were plotted at the end of the analysis to allow for the dissipation of energy. For (a), (b), and (c), the maximum tensile stress (maximum principal stress) on the scale is 394 MPa, corresponding to the tensile strength of the brick masonry. For (e), the maximum tensile stress on the scale is 527 MPa, corresponding to the tensile strength of rammed earth. In the brick masonry structural components, the locations with highest tensile stress are on wall Z1-S, and in the rammed earth, the tensile stress forms a circular pattern on the outside wall. At the end of the analysis, none of the selected regions have tensile stresses greater than the tensile strength of their materials. The compressive stresses (minimum principal stress) in the regions on which the blast is being applied can be seen in Figure 69. This allows the regions which may have compressive failure in the material to be identified. For (a), (b), and (c), the minimum stress on the scale is 7880 MPa, corresponding to the compressive strength of the brick masonry. For (e), the minimum stress on the scale is 4389 MPa, corresponding to the compressive strength of rammed earth. Some regions of higher compressive stresses are seen around the windows on the outside wall (Figure 69d). The vaults and the brick masonry walls in Zone 2 also have higher values of compressive stress than the other regions. Nevertheless, the compressive stress in any of the materials in Figure 69 does not exceed the respective compressive strength.

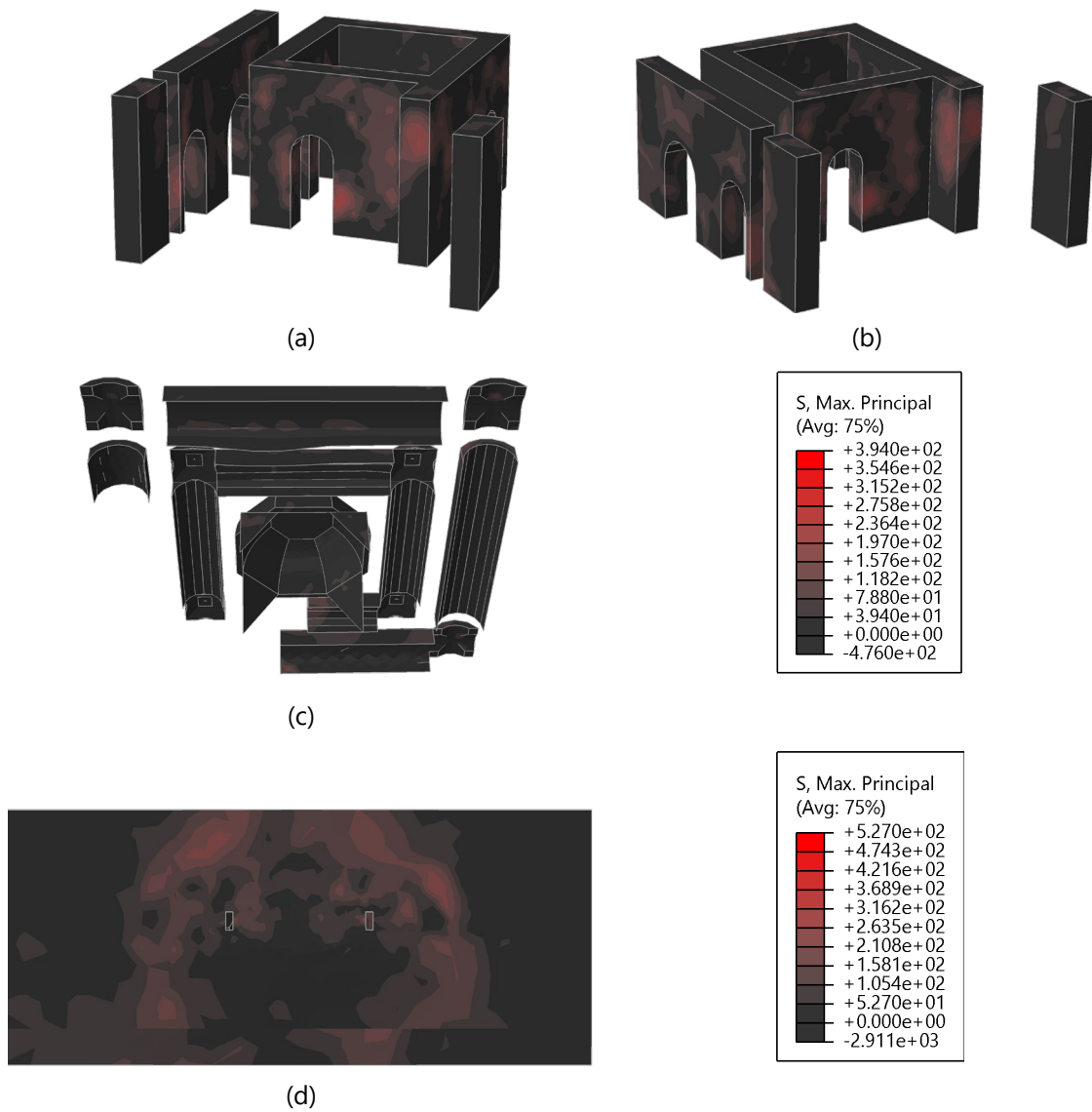


Figure 68. Tensile stresses: (a) inner walls facing East; (b) inner walls facing West; (c) vaults; and (d) exterior north wall facing South.

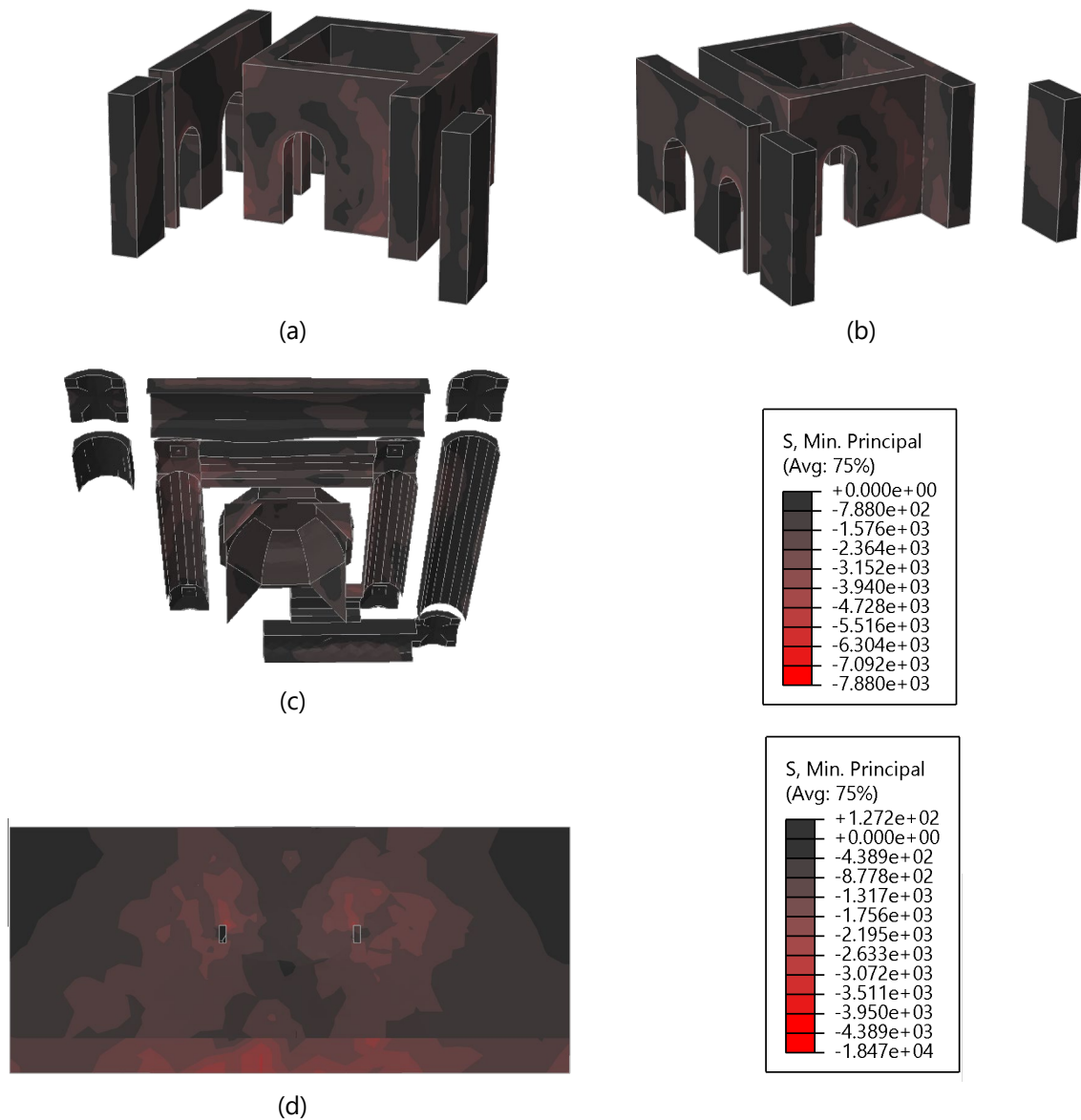


Figure 69. Compressive stresses: (a) inner walls facing East; (b) inner walls facing West; (c) vaults; (d) exterior north wall facing South.

The tensile strains show which areas in the building may experience cracking. The tensile strain (maximum principal strain) in the regions where the blast load is applied can be seen in Figure 70, where the maximum tensile strain on the scale corresponds to a value of 5%. Some tensile strains can be noted around the arch at the inner nave and at the base of the inner nave (Figure 70a). Concentrations of tensile strains can also be noted at the East and West walls in Zones 1 and 2, at the corners where the walls would intersect the collapsed wall, wall Z1-S (Figure 70a and b). Extremely high concentrations of strain can be seen at the base of the vaults (Figure 70c), which are defined as the locations where the vaults meet the collapsed inner wall (Z1-S) and where the vault meets the exterior rammed earth walls. The compressive strain allows the determination of locations where crushing of the masonry or the rammed earth is possible. The minimum compressive strain on the scale corresponds to a value of 2%. Figure 71a and b show a high concentration of compressive strains at

the right side of the inner nave. A significant concentration of strain is also seen at the base the vaults which surround the most damaged wall (Figure 71c). In the remaining locations where the blast load was applied, no significant compressive strain concentrations could be noted.

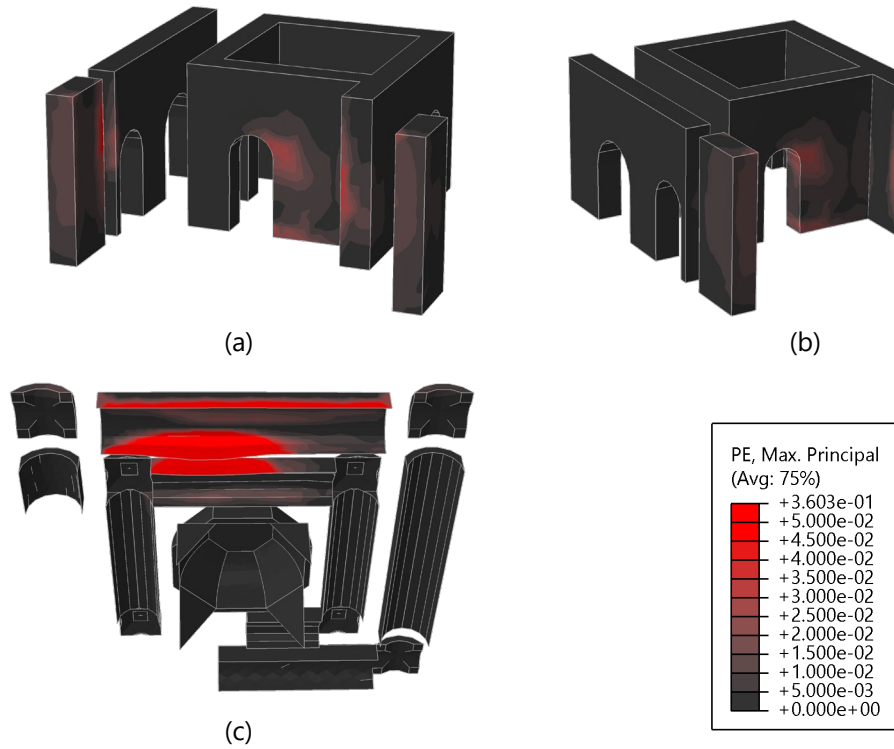


Figure 70. Tension strains: (a) inner walls facing East; (b) inner walls facing West; (c) vaults.

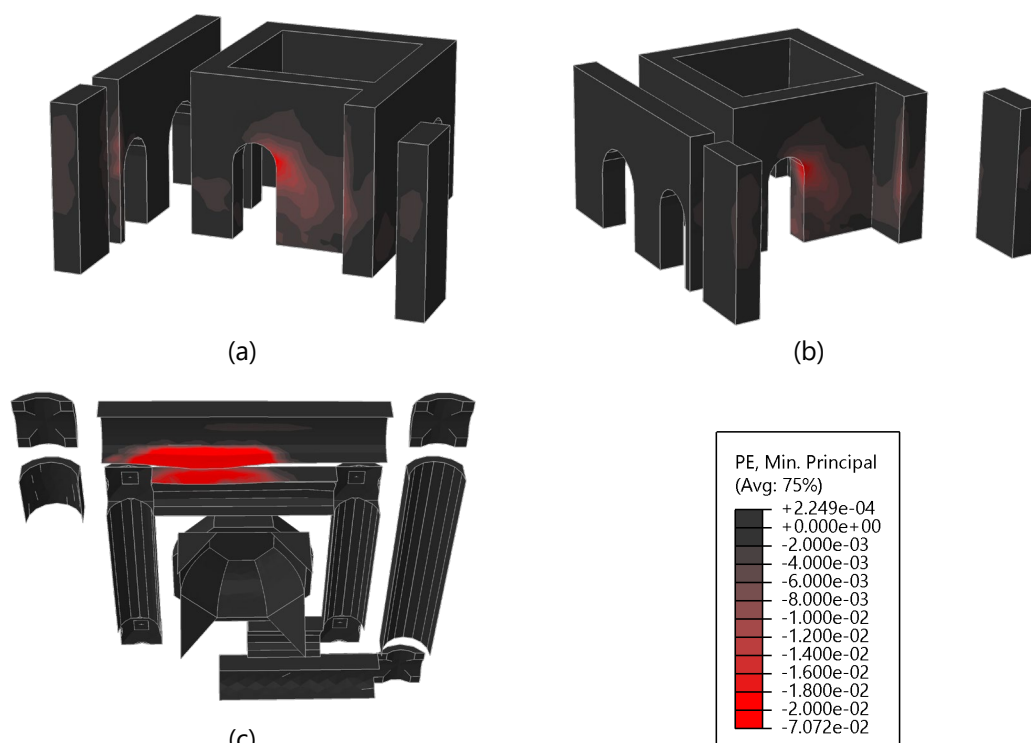


Figure 71. Compression strains: (a) inner walls facing East; (b) inner walls facing West; (c) vaults.

The tensile damage in the regions on which the blast is being applied can be seen in Figure 72. As with the previous loading scenario, a value of 0.77 was selected as the damage threshold according to Hoveidae et al. (2021). When looking at the damage evolution, significant damage is noted on the wall Z1-S, just when the load is being applied. Employing the failure volume index previously used (Hoveidae et al., 2021), the damage index and damage level were calculated for the whole Level 2 and for individual regions in the model (Table 17). Note that, as stated, HD indicates High Damage and SD indicates Small Damage. Overall, the whole Level 2 has a damage level of small, meaning minor cracking and no out-of-plane damage. However, when looking at individual structural elements, Wall Z1-S has a high damage level, which is expected due to the noticeable out-of-plane displacement in the wall. When looking at the other structural components individually, they all have small damage levels. Although the damage index suggested by Hoveidae et al. (2021) may be appropriate when assessing the damage caused by seismic events, its use when analyzing the effects of localised loading conditions such as blast loading may not be appropriate, or at least some caution should be had when trying to apply these.

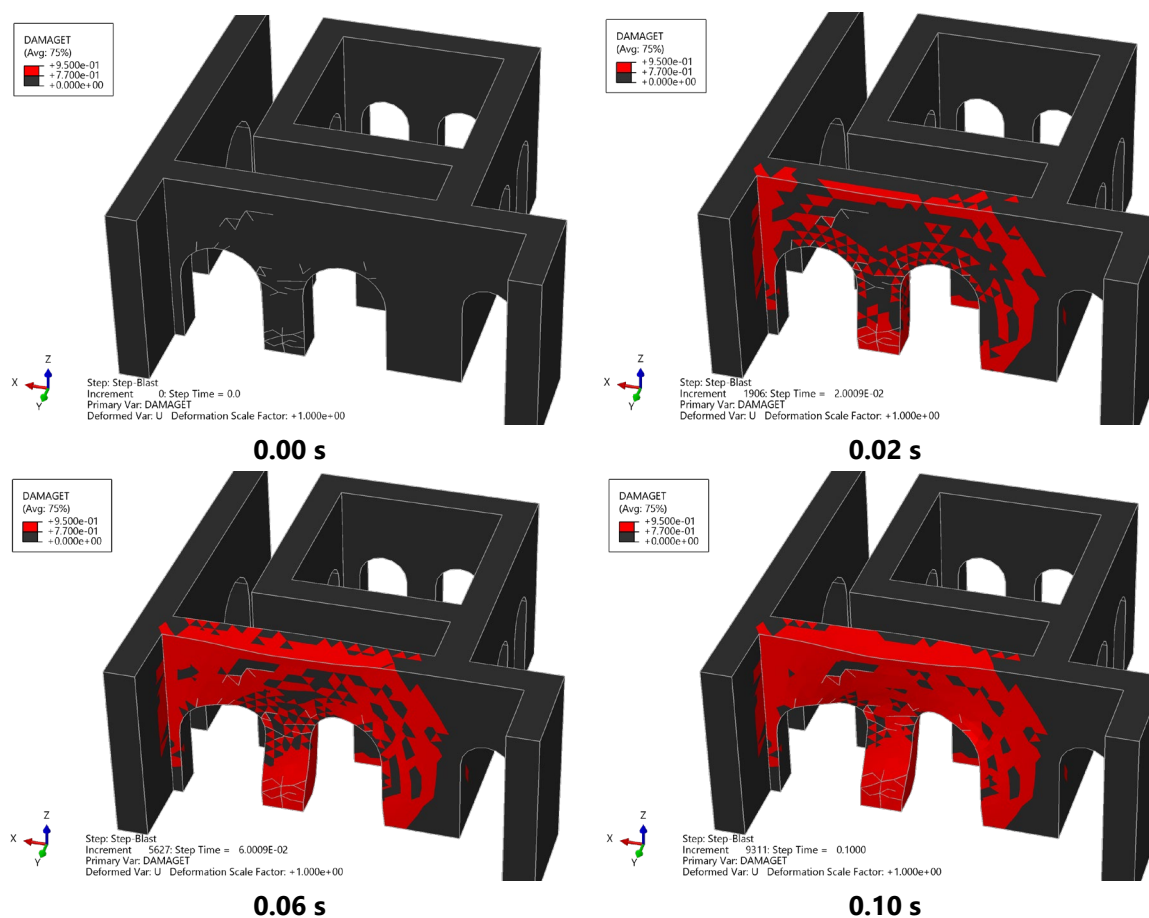


Figure 72. Time history of the damage to the interior walls of the building.

Table 17. Total volume, volume of damaged elements, damage index, and damage level for different structural components.

	Volume [m ³]	Damaged Volume (D>0.77) [m ³]	Damage Index	Damage Level
Main Wall	1.22E+01	6.49E+00	53.14%	HD
Zone 1 Wall Left	3.02E+00	6.92E-02	2.29%	SD
Zone 1 Wall Right	3.02E+00	0.00E+00	0.00%	SD
Zone 23 Wall Left	8.88E+00	0.00E+00	0.00%	SD
Zone 23 Inner Walls	2.76E+01	4.46E-01	1.61%	SD
Vaults Zones 1 2 3	5.27E+00	4.76E-01	9.04%	SD
Outer Wall near Blast	1.72E+02	1.37E+01	7.98%	SD
Whole Level 2	1.43E+03	3.34E+01	2.33%	SD

5.2.3 Interior Blast Loading Results on Single Wall

The wall with the most damage in the previous analysis was modelled on its own to better understand the effect of the mesh size on the damage. Boundary conditions on this wall were selected so that the deformed shape of the wall matched the wall in the previous analysis. Additionally, this wall was modelled using three different element sizes to understand if this had an impact on the damage in the wall. The wall with the three different element sizes can be seen in Figure 73.

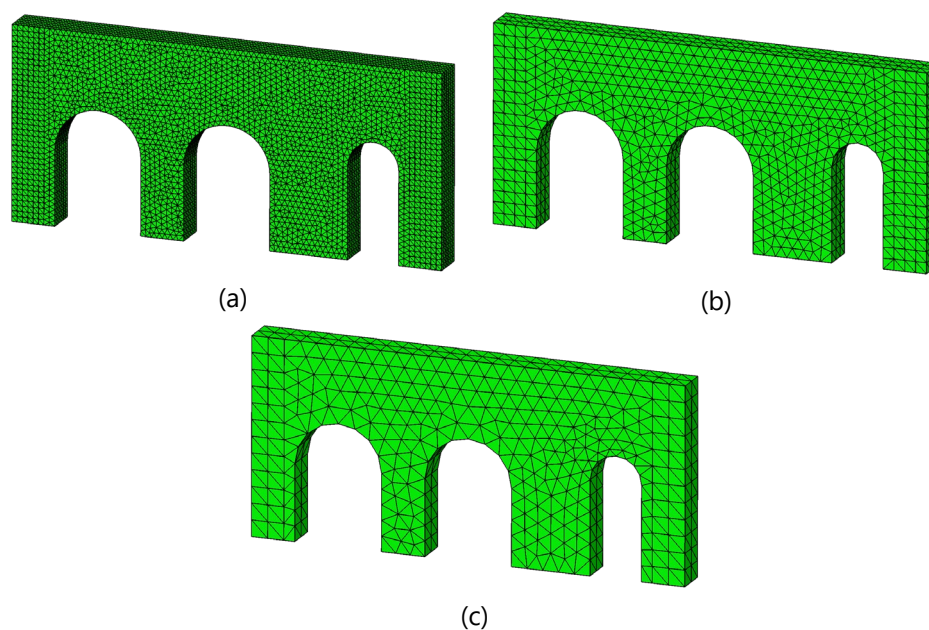


Figure 73. Mesh sizes: (a) 0.1 m; (b) 0.2 m; (c) 0.3 m.

Three different parameters were considered, the first being the displacement, the second being the rotation, and the third being the failure volume index. Some authors have defined the failure of a wall under blast loading as the point at which the wall reaches a displacement equal to its thickness (Doherty et al., 2002; Zapata & Weggel, 2008). The wall being studied has a thickness of 0.6 m. For mesh sizes of 0.1 m and 0.2 m, the maximum displacement reached the wall thickness at 0.06 s (Figure 74). The wall with a mesh size of 0.3 m has a lower displacement and does not reach a maximum value of 0.6 m at the same time as the other two walls, thus not reaching failure at the same moment. However, the wall with a mesh size of 0.3 m does eventually reach failure. The effect of the mesh size over time on the failure based on the displacement is further visualized in Figure 75. In general, the results are too different and not converging upon mesh refinement, so the subject requires more attention. In this particular scenario, using a larger mesh seems to cause the underestimation of the damage in the wall. Thus, using the displacement method to characterize the damage occurring due to blast loading seems to be mesh dependant. According to UFC (UFC 3-340-02, 2008), the failure of a two-way masonry wall under blast loading can be defined as reusable if the rotation at the supports is exceeding a value of 0.5° and non-reusable if exceeding a value of 2.0° . Using this criterion, the wall fails very early in the application of the load, for all sizes of mesh (Figure 76). The rotation of the wall at a later point in time also decreases as the mesh size decreases. Once again, this requires further attention in future works. The rotation is calculated as a function of the displacement, so the same trends in the damage due to the displacement are expected in the damage due to the rotation with respect to the influence of the mesh size. It should be noted that the displacement results are expected to converge, though some differences may be justified when operating outside the assumption of small displacements. Consequently, this comparison between the effect of the mesh size on the damage requires further investigation.

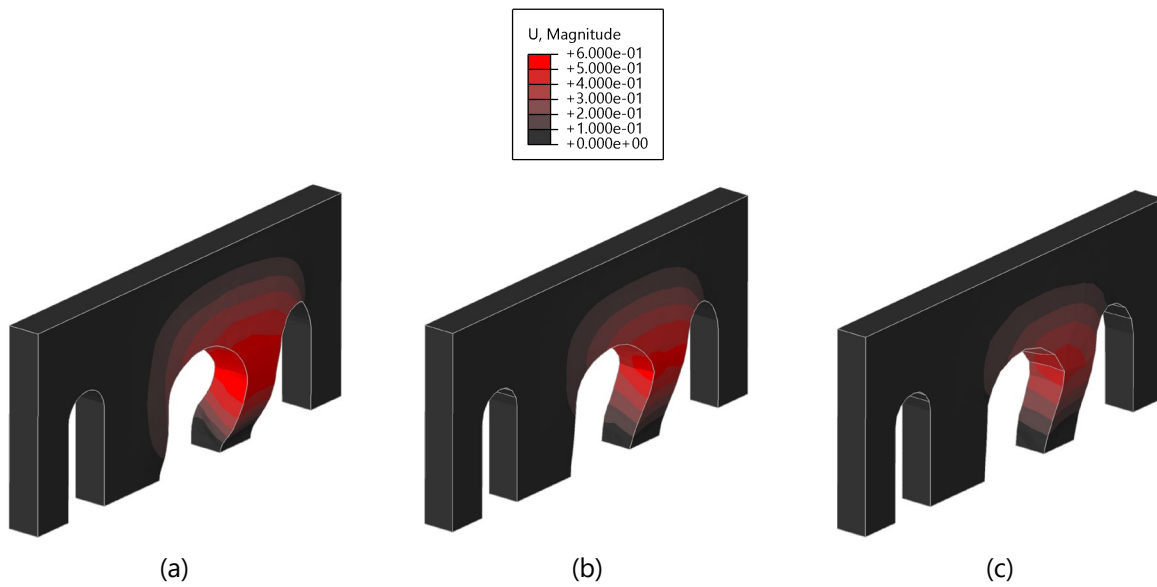


Figure 74. Displacement at 0.06 s for different sized meshes: (a) 0.1 m; (b) 0.2 m; (c) 0.3 m.

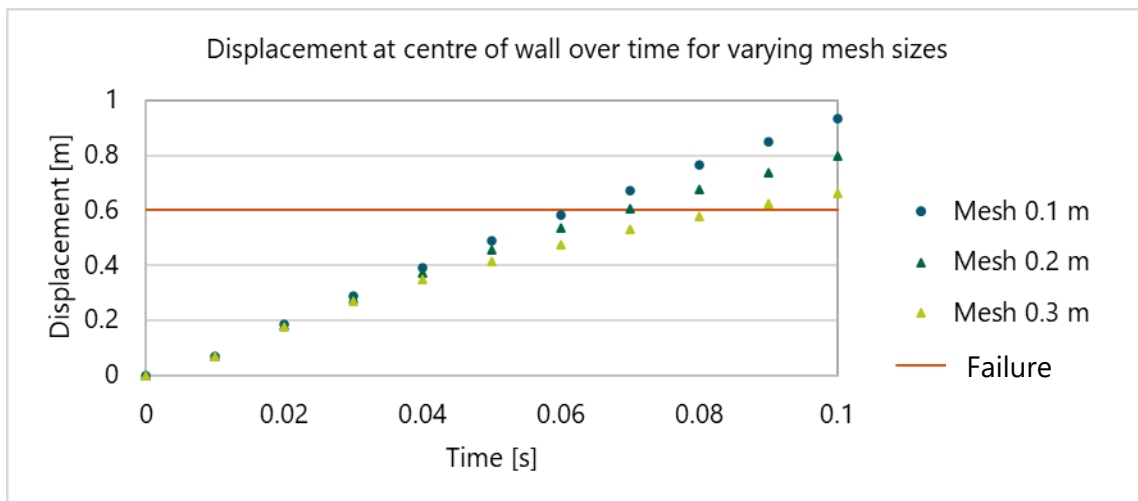


Figure 75. Displacement at the centre of the wall over time.

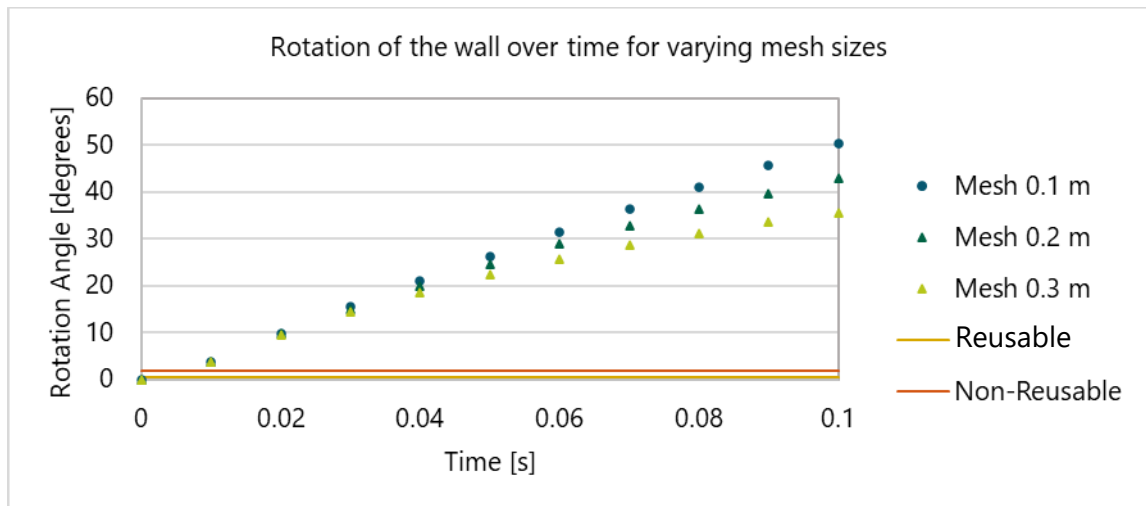


Figure 76. Time history of the rotation of the wall for different mesh sizes.

The failure volume index, which uses the tension damage available as a field output in Abaqus, seems to be the best approach to compare the damage in the wall between models of different element sizes. By observing Figure 77, the models of different mesh sizes have the same damage distribution. A high concentration of damage is visible at the top of the wall and around the middle and right arches. Some damage is also located at the top of the left arch. As the damage to the wall is significant, the actual impact of the mesh size on the damage distribution is difficult to identify. Figure 78 further confirms the minimal influence the mesh size has on the damage index. When the load is first applied, the walls with mesh sizes of 0.1 m and 0.3 m both have a medium damage level, while the wall with a mesh size of 0.2 m has a damage level of small. After that point, all the walls experience high damage. In sum, this wall will fail when exposed to a device of 6.8 kg of TNT in the North room.

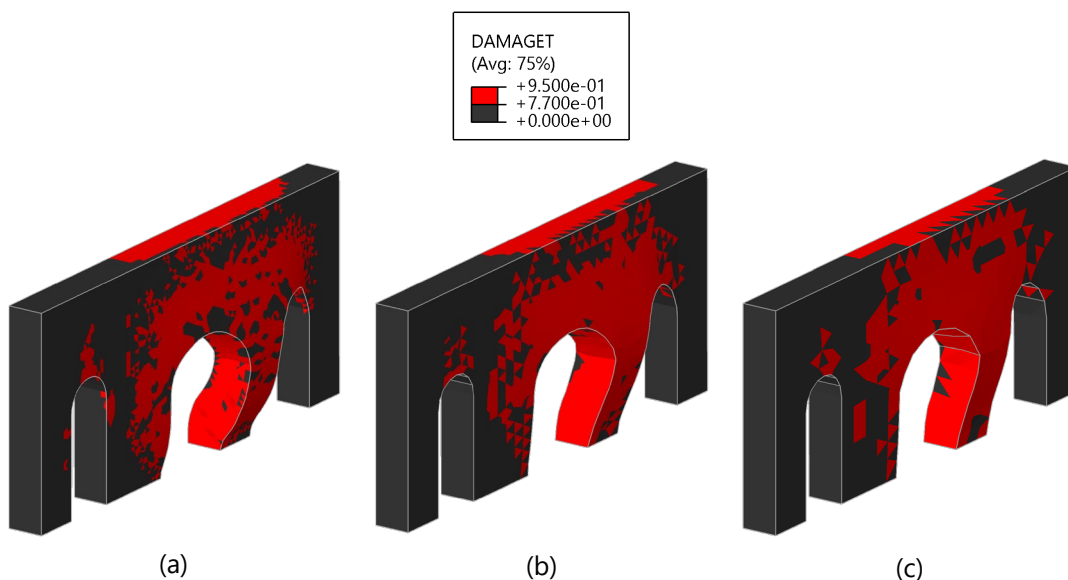


Figure 77. Tensile damage at 0.06 s: (a) 0.1 m; (b) 0.2 m; (c) 0.3 m.

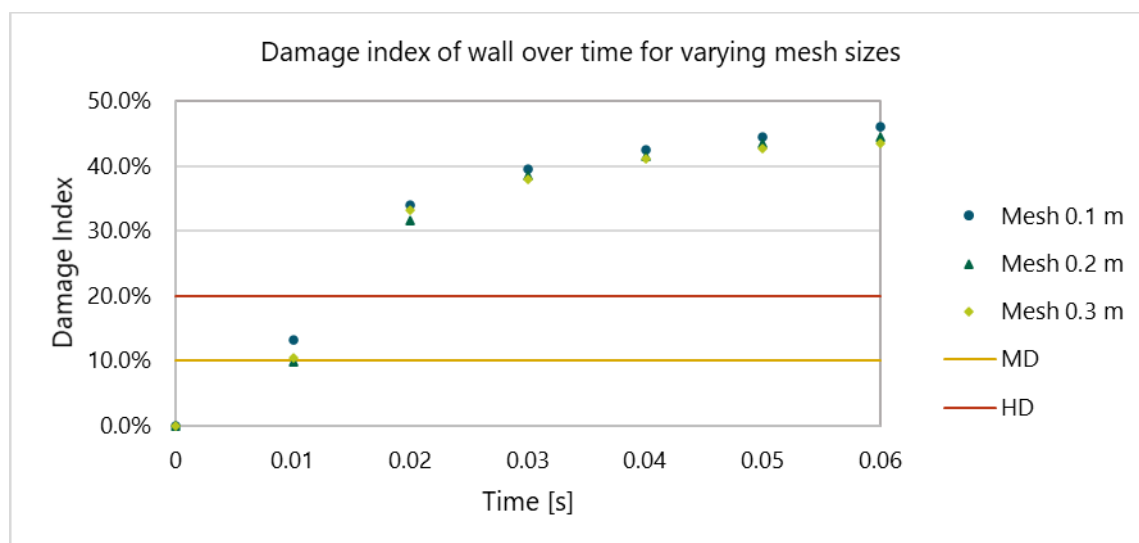


Figure 78. Damage index of the wall over time.

The use of a 6.8 kg of TNT explosive device in the North room of Level 2 in the tower was too high to properly compare the resulting damage between mesh sizes. As such, an explosive device of 2.5 kg of TNT was selected to make this comparison. To do this comparison, continuum models with and without removal of damaged elements were created. Evidently, the size of the mesh has an effect on the damage distribution of wall Z1-S (Figure 79). In all three walls, the top of the column between the two largest arches is completely damaged, as no elements remain to connect the base of the column to the rest of the wall. Similarly, all three walls show damage at the top of the wall, but the number of damaged elements decreases as the mesh size increases. In the walls with mesh sizes of 0.1 m and 0.2 m, significant damage is noted above the left arch, but this damage pattern is not visible in the wall with a mesh size of 0.3 m. In the model with a mesh size of 0.1 m, circular cracks can be observed between the two rightmost arches, starting above the left arch and continuing to the top of the wall. Thus, the mesh size has an impact on the damage seen in walls under blast loading. Since the removed elements occur when the degradation reaches the maximum degradation at a single integration point, the walls with removed elements are more likely to show more extensive damage patterns than the walls using banded contour plots to show the damage. This occurs because the values of damage are extrapolated from the integration points to the nodes. Nevertheless, the distribution between the damage patterns is similar. This similarity can especially be noted in Figure 79a, and Figure 79b, with the radial crack present between the centre and right arches. In all the walls in Figure 79, damage is present at the base of the wall between the left and centre arch. Interestingly, the walls with damage plotted using contours show damage at the top of the wall, but at the front, whereas the removed damage elements at the top of the wall occur at the back. As the damage plotted in red is extrapolated from the integration point to the node, the contours represent locations where the node exceeds the given threshold of damage. However, the elements are removed when a single integration point exceeds the damage threshold. Consequently, the difference between the locations of damage is likely caused by the way the data is interpreted in these locations.

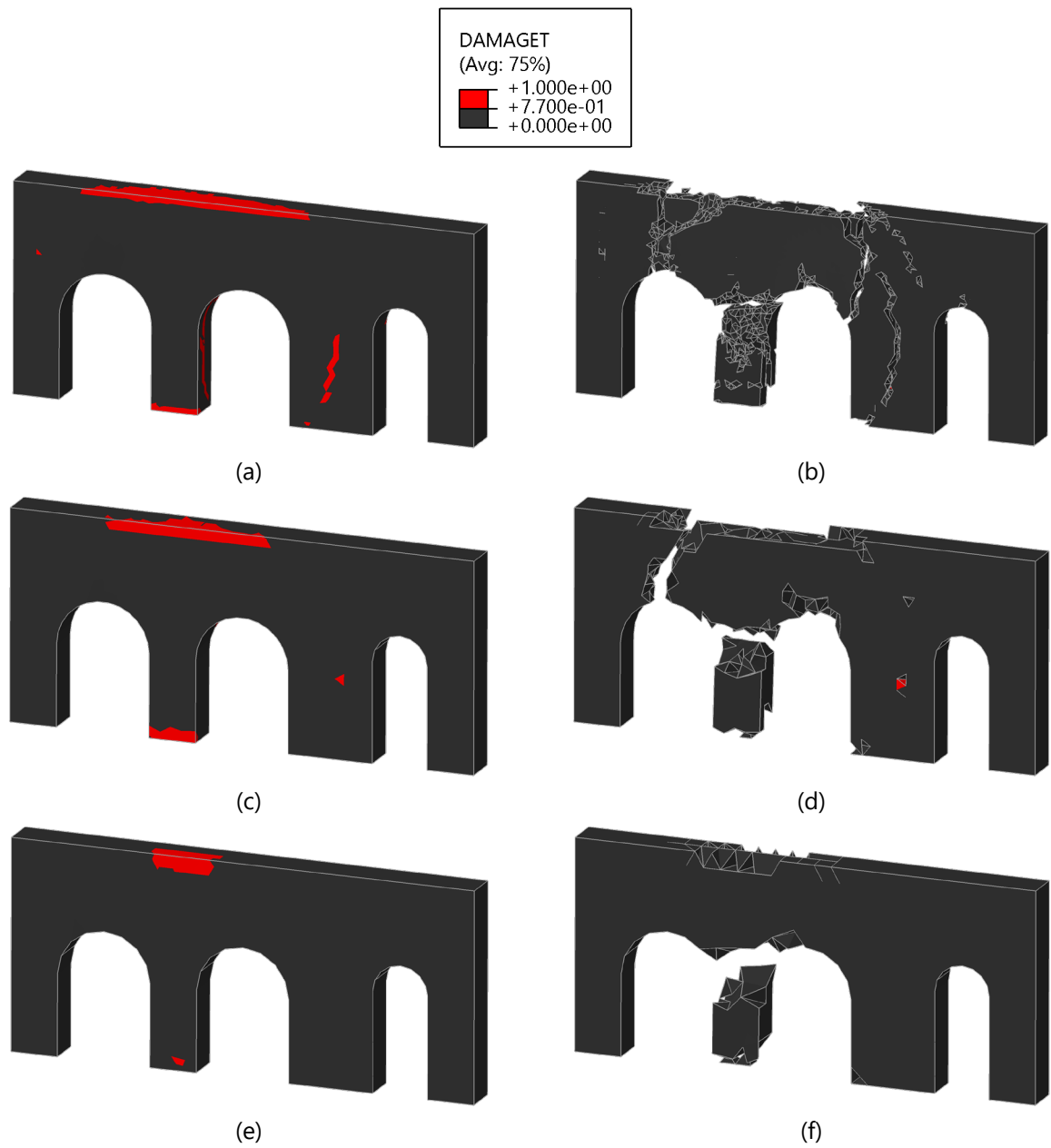


Figure 79. Tension damage to wall Z1-S at 0.1 s: (a) 0.1 m mesh; (b) 0.1 m mesh with removed damaged elements; (c) 0.2 m mesh; (d) 0.2 m mesh with removed elements; (e) 0.3 m mesh; (f) 0.3 m mesh with removed elements.

CHAPTER 6

6 IMPACT LOADING

Impact loading analysis plays an important role in structural engineering, whether that being historical or modern-day warfare, terrorist attacks, or accidental vehicle crashes. The properties of the impactor have a direct effect on whether the structure will exhibit a global or local response or failure. This chapter will present the loading conditions and the results for a portion of the wall in the *Torre de la Vela* under impact loading defined by a historical cannon ball. The local response of the building in the region of the impact will be investigated. The use of continuum elements with and without removal of damaged elements, and the use of contact elements will be compared. Finally, a hypothetical impactor was modelled to better understand the local behaviour of the continuum model under impact loading.

6.1 16th and 17th Century Cannonballs

The loading scenario studied in this analysis corresponded to a cannon ball for the culverin cannon, found in sixteenth-century Spanish artillery (Manucy, 1949). Based on Hall (1952), this cannon had sufficient range to strike the *Torre de la Vela* considering the geographical locations of the fortifications of the Alhambra. The properties of the cannon balls used in the culverin have been discussed in Section 3.3.2, and the material properties of cast iron were obtained from Angus (1976). All this information is summarized in Table 18. The fourth level on the South façade was selected as the location where the impactor would strike. The size of the impactor is negligible compared to the thickness of the wall and, therefore, only the upper portion was modelled as a local response was expected. Three different models were created: a continuum model with and without removal of damaged elements (Figure 80a), and a contact model (Figure 80b). The impactor was modelled as a soft body, at an initial distance of 0.02 m from the wall to reduce computational time (Figure 80c). The interaction between the impactor and the wall was defined by general contact, using hard contact as the normal behaviour contact property. Separation was allowed after contact. The translational velocity of the impactor was defined using a predefined field in the load module in Abaqus. For the continuum element model, the mesh was refined around the location of impact (Figure 81). The contact elements model used the same interaction properties as defined in Section 5.1.3.

Table 18. Properties of the impactor.

Diameter	Density	Velocity	Young's Modulus	Poisson's Ratio
13 cm	6.31 T/m ³	408 m/s ²	165 × 10 ⁶ kN/m ²	0.27

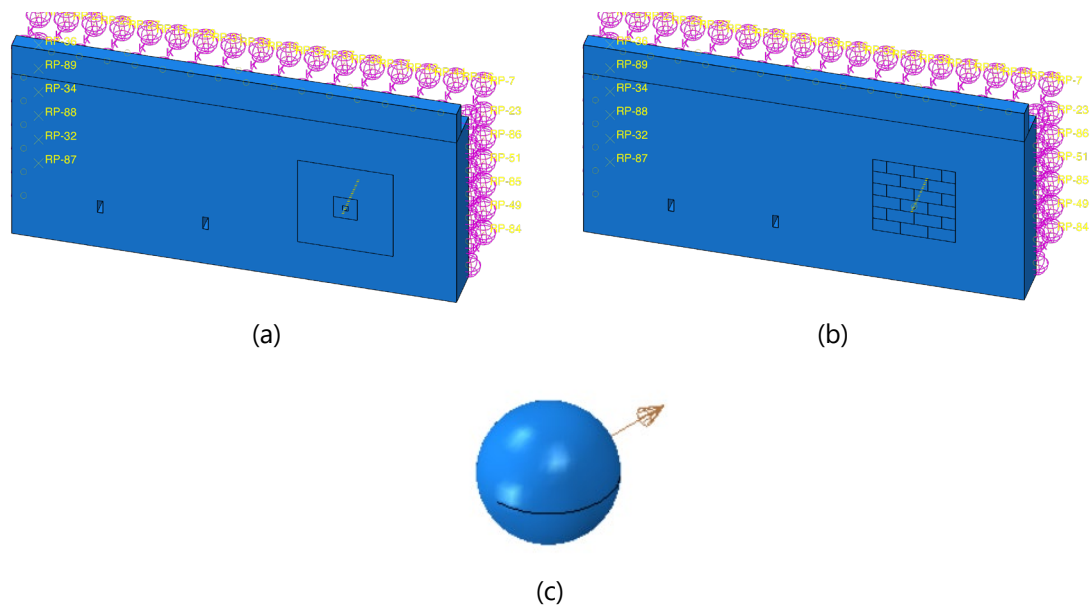


Figure 80. Loading definition: (a) continuum model; (b) contact element model; (c) impactor.

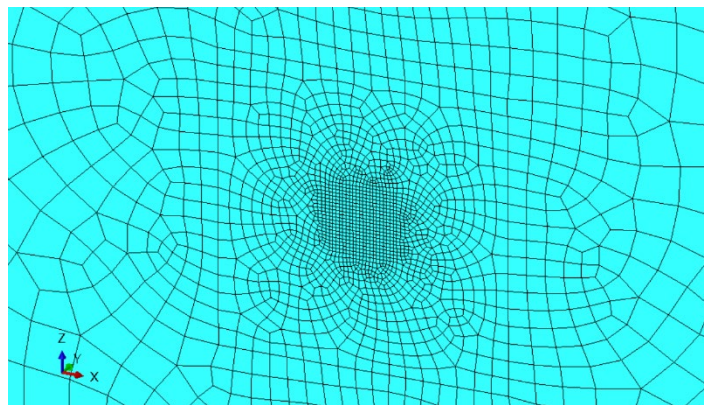


Figure 81. Refined mesh around the location of impact.

The strain rate for the impact loading scenarios was expected to be lower than the one previously stated in Chapter 4 for blast loading. As such, new dynamic increase factors had to be selected based on the strain rate in the system. A strain rate of 10^0 s^{-1} , associated to impact loading (Ngo et al., 2007) was selected. Using the equations for DIFs according to Pereira (2014), the DIFs for the compressive strength, σ_c , and the Young's Modulus, E , were determine as 1.0 for rammed earth. Consequently, the mechanical properties used for these analyses are the ones presented in Table 9.

After processing the results, negligible damage in the continuum models was noticed. Similarly, the stress distributions between both continuum models were identical. As such, the results from the continuum model with removable damaged elements will not be presented. Only the stresses on the wall were plotted on the wall, as the displacements and the strains in the wall were negligible. The time history of the compressive stresses after impact can be seen at the front of the wall in Figure 82. Note that the time has been normalized such that the moment of impact is considered at 0.0 s. Here, the lower bound of the compressive stress is 100 kN/m^2 , which is much lower than the actual compressive

strength of the rammed earth. Although the impactor does not cause any compression damage on the wall, the distribution of stresses in the wall is still worth noting. In Figure 82, the contact model dissipates energy faster than in the continuum model. This is particularly noticeable at time 0.006 s as a high concentration of compression stresses is found at the location of impact in the continuum model but not in the contact model. In the contact model specifically, the compressive stresses appear to be mostly confined to the contact block being struck at first. As the energy dissipates, it can be seen that the contact block being struck is applying compressive stresses on the blocks horizontally adjacent to it. Another interesting difference between the continuum model and the contact model is the compressive stresses at the rear of the wall (Figure 83). In the continuum model, the stresses have been transferred from the front to the back of the wall, but in the contact model, negligible stresses have been transferred to the other side of the wall.

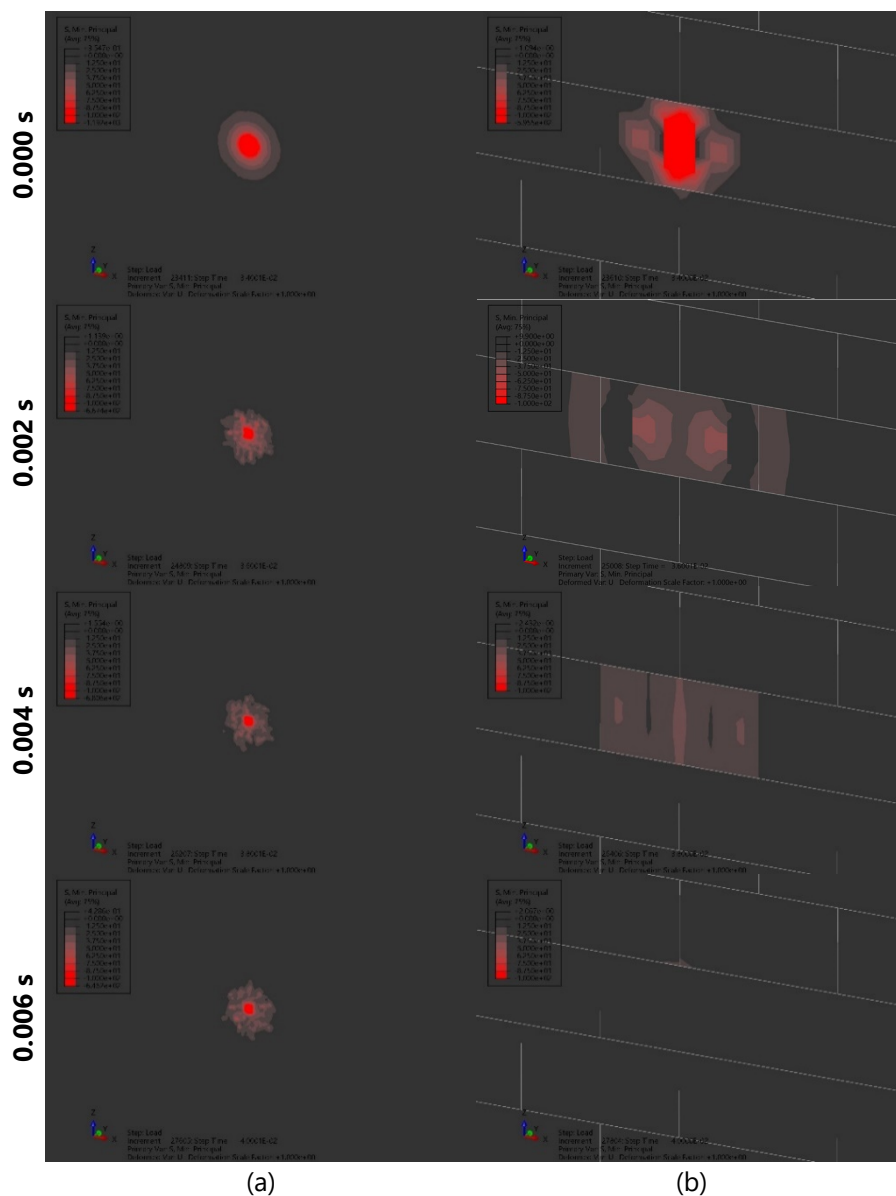


Figure 82. Time history of compression stresses immediately after impact on the front of the wall: (a) continuum model; (b) contact model.

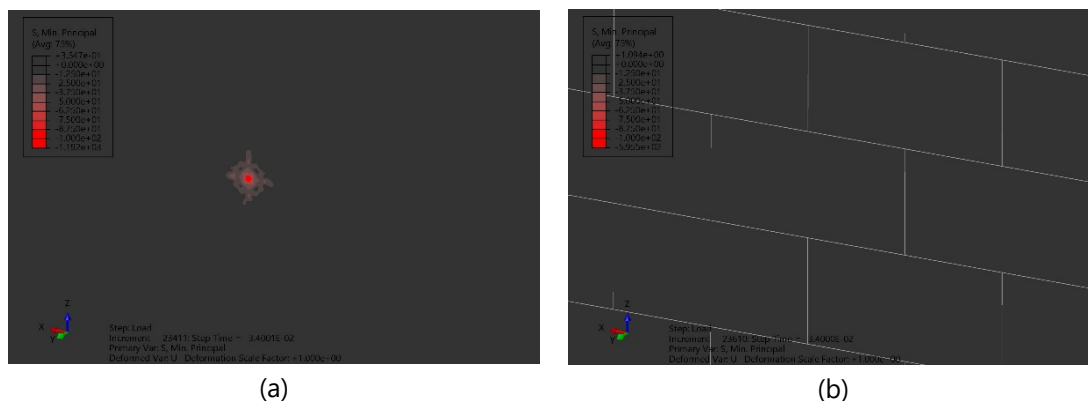


Figure 83. Compression stresses in the back of the models after impact: (a) continuum model; (b) contact element model.

The time history of the tensile stresses after impact can be seen for the front of the wall in Figure 84. In these plots, the upper bound of the tensile stress is 100 kN/m^2 . The impactor does not cause any tensile damage in the rammed earth since the tensile strength of the rammed earth is 527 kN/m^2 . However, the tensile stress distribution in the material is still of interest. At impact (Figure 84), the tensile stresses are much lower in the continuum model than in the contact model. At the location where the impactor strikes the wall in the contact model, no tensile stresses are present, likely due to the compressive stresses at that location. However, in the continuum model, a high concentration of tensile stresses is still present at the location of impact. This is likely due to the extrapolation of the tensile stresses to the nodes in that location. As with the compressive stresses, the tensile stresses in the material dissipate much faster in the contact model than in the continuum model. In the continuum model, the tensile stress expands radially from the central location of impact. However, in the contact model, the tensile stresses are confined to the single contact element where the impactor is hitting, with some tensile stresses following the joint pattern in the vertical direction. A stress concentration is still visible at the back of the wall in the continuum model (Figure 85a), whereas no residual tensile stresses reach the back of the wall in the contact model (Figure 85b). Overall, the behaviour of the two models is much more similar on the front façade of the wall than on the back of the façade.

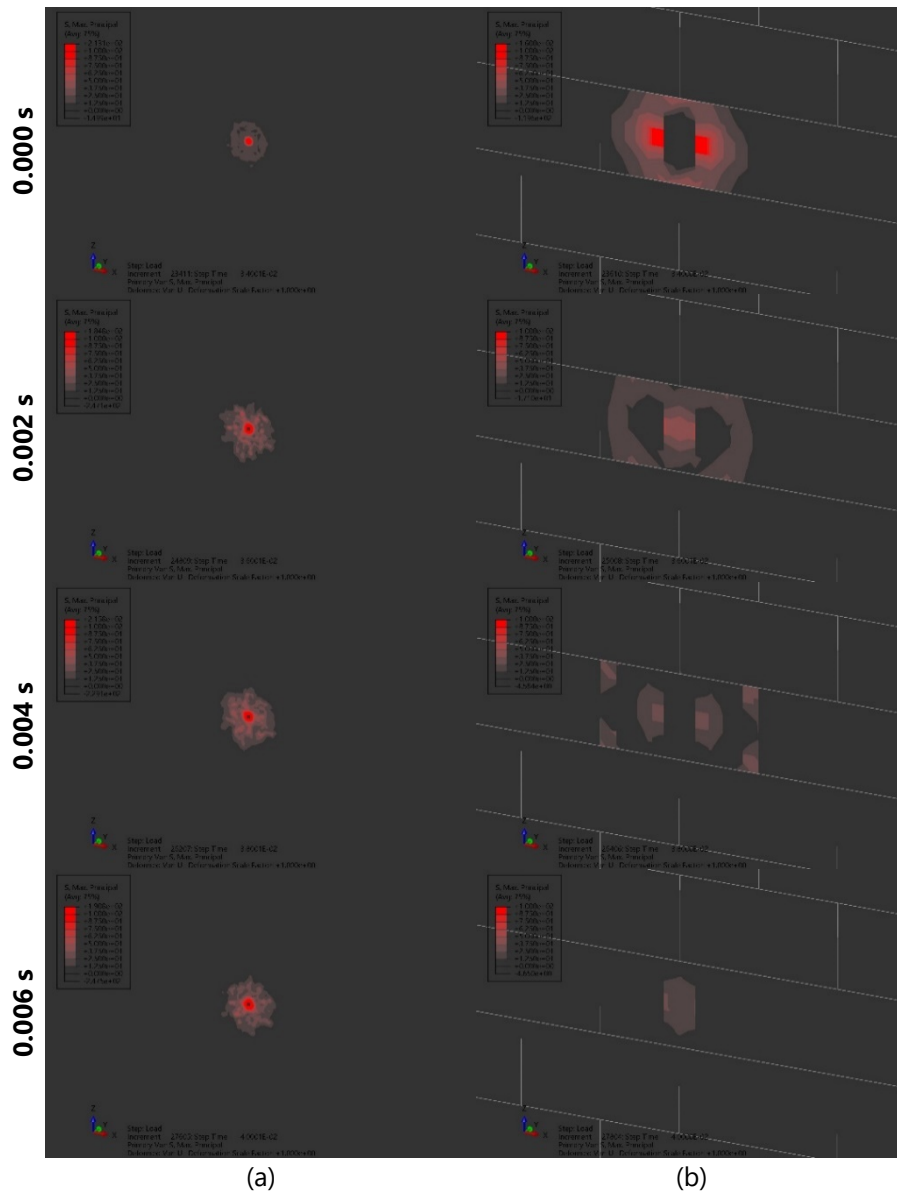


Figure 84. Time history of tensile stresses immediately after impact on the front of the wall: (a) continuum model; (b) contact model.

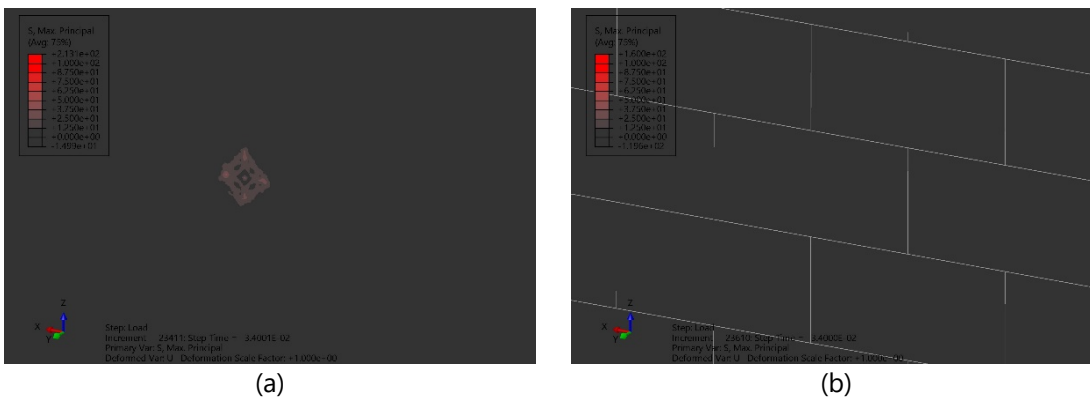


Figure 85. Tensile stresses in the back of the models after impact: (a) continuum model; (b) contact element model.

Although the displacements were not plotted as contours, the displacements at the impacted node over time can be viewed. The displacement from the continuum model is much greater than the contact model, despite both these models showing very similar trends with respect to the behaviour after impact (Figure 86). Despite the displacement from the continuum model being much greater, both their displacements are negligible. This difference in the displacements between the two models could be caused by a difference in the energy that remains in the system after the impact. In fact, Figure 87 shows the total energy in the output set, obtained from Abaqus, for the wall assembly. After impact, the energy in the continuum model system (blue) remains the same, whereas a sharp increase followed by a sharp decrease exists in the contact model (yellow). Additionally, less energy is present in the contact model system immediately after impact.

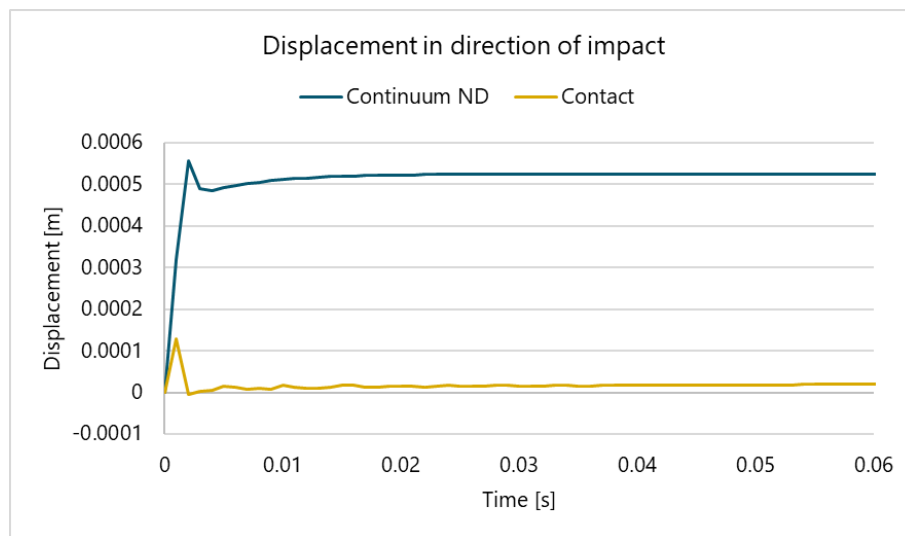


Figure 86. Displacement at the impacted node in the direction of the load.

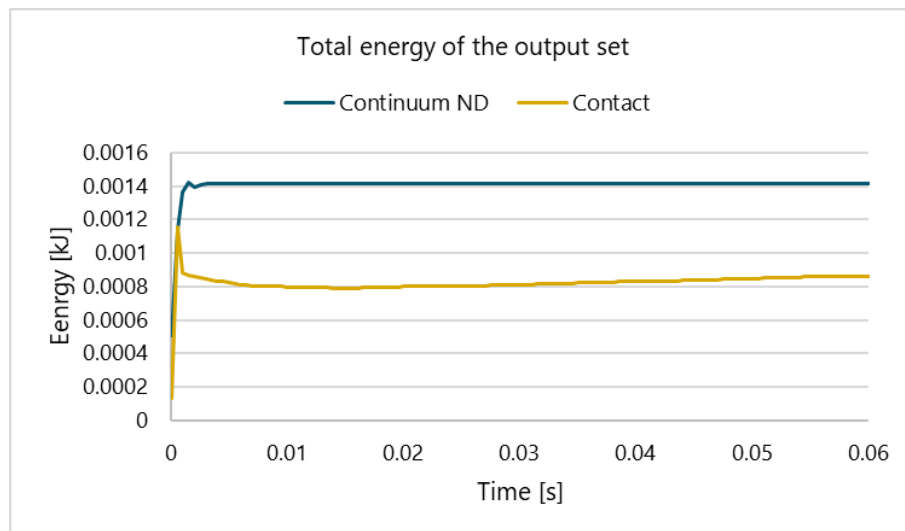


Figure 87. Total energy of the output set.

The use of contact elements in the model seems to dissipate the energy from the impact differently than in the continuum model. The *Torre de la Vela* would not have any damage caused by the impact of a cannon ball from a 16th-century Spanish culverin based on this analysis.

6.2 Hypothetical Impactor

In Section 6.1, the impactor did not cause any damage to the model. For this reason, a hypothetical impactor was modelled to analyse how the continuum model using Abaqus feature involving the removal of damaged elements would behave under impact loading. The continuum model with the removal of damaged elements defined in Section 6.1 was used for this analysis using a hypothetical impactor. The size of the impactor and the impactor's velocity were increased to try and cause damage in the wall. The properties used for the hypothetical impactor can be seen in Table 19, where the diameter and the velocity of the hypothetical impactor have been changed.

Table 19. Properties of the hypothetical impactor.

Diameter	Density	Velocity	Young's Modulus	Poisson's Ratio
50 cm	6.31 T/m ³	600 m/s ²	165 × 10 ⁶ kN/m ²	0.27

After processing the results, minor damage to the surface of the wall was observed. This is characterized by the removed elements at the surface of the model (Figure 88). Here, the lower bound of the compressive stress is plotted as 100 kN/m², which is much lower than the actual compressive strength of the rammed earth, which is 4390 kN/m². Between 0.0 s and 0.2 s, the damage in the wall increases significantly, but the change in damage between 0.4 s and 0.6 s is minimal. Although many elements have been removed, the compressive stress in the wall is still well below the compressive strength of the wall for the remaining elements. The stress distribution in the wall is very localized, with high values of stress only in the area surrounding the damage caused by the impactor. The higher values of compressive stress are located inside the hole caused by the impactor, in the area where compression would be expected. The stress distribution at the location of impact does not change significantly between 0.4 s and 0.6 s. Similarly, the tensile stresses in the wall over time following the impact could be observed (Figure 89). In these plots, the upper bound of the tensile stresses is plotted as 200 kN/m², which is also lower than the tensile strength of the rammed earth which is 527 kN/m². As with the compression stresses, the stresses are mostly located around the damaged area. The higher values of tensile stress are in the regions surrounding the hole caused by the impactor, but not inside the hole itself.

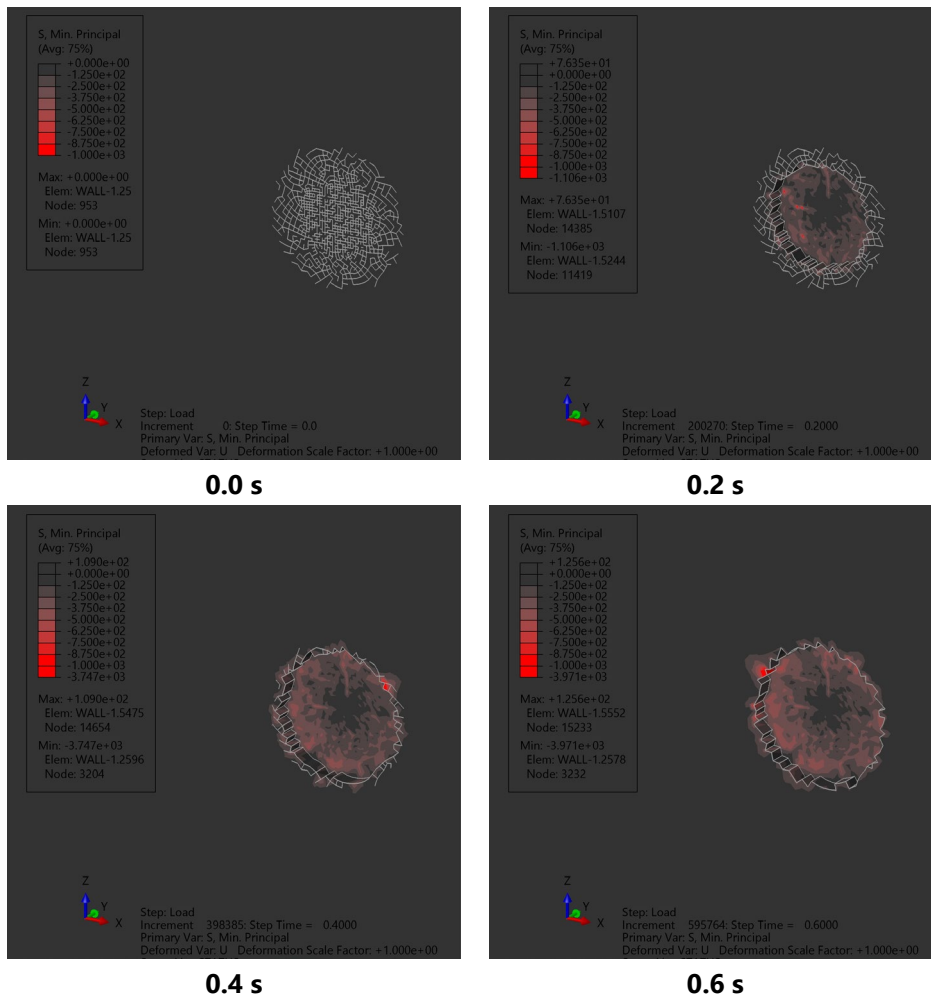


Figure 88. Time history of compression stresses.

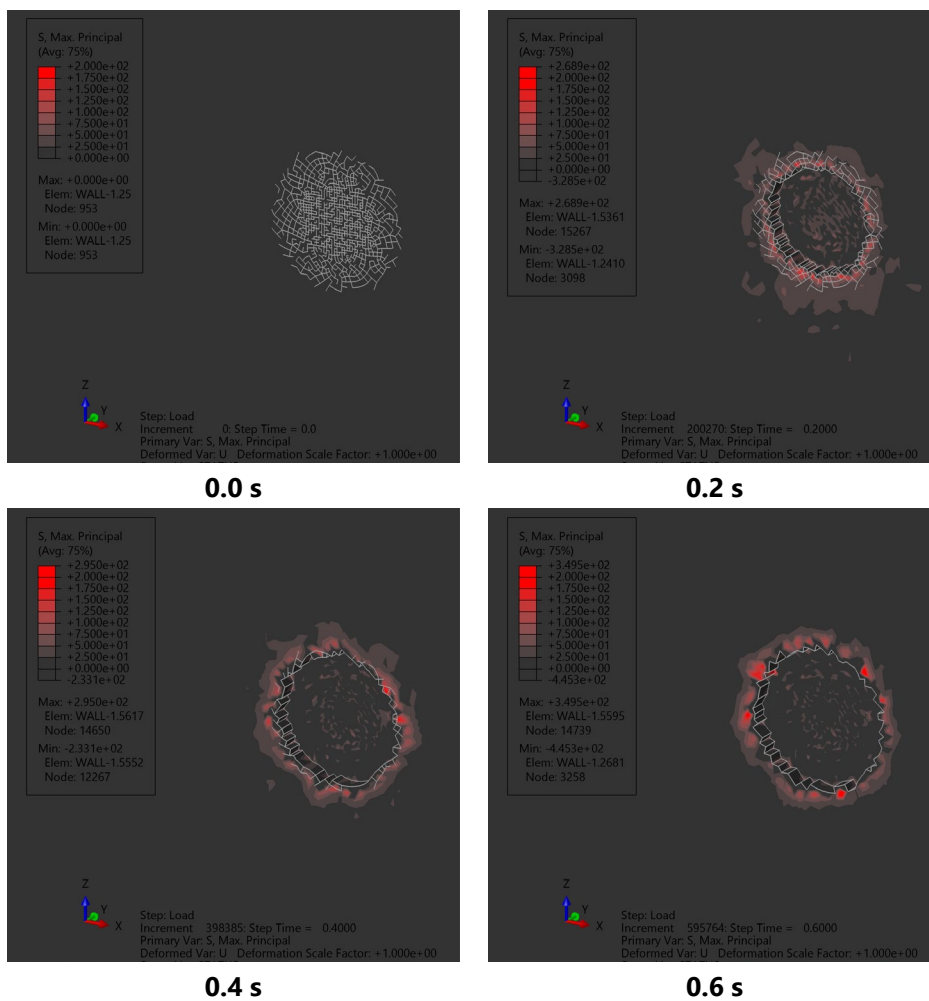


Figure 89. Tensile stresses in the wall caused by the impactor over time.

The diameter of the hole caused by the impactor over time can be seen in Figure 90. This data shows that the trend for the diameter of the hole is logarithmic. At the end of the analysis, the size of the hole remains constant. The maximum diameter of the hole is 53 cm, slightly greater than the diameter of the impactor, indicating that the maximum possible diameter of the hole is approximately the same size as the impactor. During this analysis, the depth of the hole caused by the impactor was approximately 6.2 cm over the entire area of the hole and did not change over time. A further inspection of the mesh shows that the depth of the hole is in fact equivalent to the depth of the first layer of elements in this location. As previously stated in Chapter 5, the damaged elements in Abaqus are removed when a single integration point in the element reaches the damage threshold. This means the depth of the hole caused by the impactor is mesh-dependent. Consequently, the mesh should be significantly refined in this area, which would allow to understand the true depth of the hole caused by the impactor. Based on the results obtained, it is not possible to determine if the analysis has been run for a sufficient time. Although the graph presented in Figure 90 suggests the wall has stopped responding, the results obtained from the depth of the hole are inconclusive. Thus, three hypotheses for the behaviour of the cannonball following impact still remain: 1) the cannon could rebound off the wall and continue displacing in the opposite direction; 2) the cannon could become embedded into the wall and its movement would stop; and 3) the cannon could continue moving through the wall at a

certain velocity, causing further damage. This is a much interesting aspect but out of scope for the present work, given the time limitations.

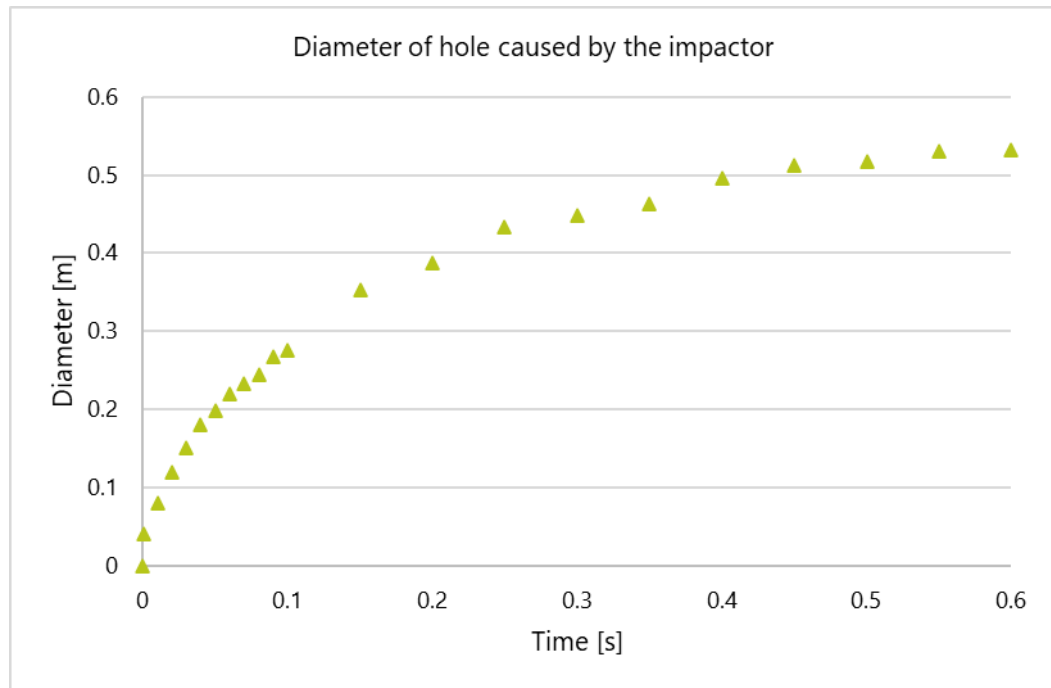


Figure 90. Time history of the diameter of the hole.

CHAPTER 7

7 CONCLUSIONS AND FUTURE WORK

The aim of this thesis was to evaluate the structural response of the *Torre de la Vela* under blast and impact loading. This work involved a review of the historical documentation available on the *Torre de la Vela*, a literature review of the available concepts and theories related to blast and impact loading, a literature review of the available numerical models, the preparation and validation of the model, and the structural analysis of the tower under blast and impact loading.

The structural analysis of the *Torre de la Vela* under blast loading was conducted for an exterior blast scenario and an interior blast scenario. Initially, 110 kg of TNT, corresponding to four barrels of gunpowder, was applied to the exterior entrance of the tower. Under these loading conditions, the building was determined to have suffered a small level of damage, according to the damage index based on the failure volume. A simplified model of the South façade of the tower was created using contact elements to better understand the displacement occurring around the door opening, being the contact elements used around the door. Springs were used to account for the remaining portions of the building. This allowed to determine that the displacements around the door using the contact model approach was very similar to those obtained in the whole building model. However, the stress and strain distributions on the façade varied between the contact model and the whole building model. Another simplified model of the South façade of the tower was created using only continuum elements, with the removal of damaged elements feature in Abaqus activated. This resulted in a large portion of damaged elements being removed around the door opening, corresponding to the location where high levels of displacement were previously seen.

For the interior blast, only a single level of the *Torre de la Vela* was modelled. An explosive device of 6.8 kg of TNT, corresponding to a quarter barrel of gunpowder, was placed in an interior room of the tower. This analysis concluded that a total failure of an interior wall next to the position of the explosive device would occur. However, the remaining structural elements would have small or medium damage due to the blast. These findings led to further investigations of the single interior wall which failed under blast loading. During the analysis of a single interior wall under blast loading, three methods of characterizing damage were assessed, and their mesh dependency was compared. For all methods, the models with a larger mesh size exhibited less damage than those with a more refined mesh. Consequently, the methods to characterize failure due to the displacement of the wall and failure due to the rotation of the support of the wall were both considered to be very mesh-dependent. The damage index based on the failure volume was determined to be mesh-independent, based on the results obtained from applying blast loading on a single interior wall in the building. However, when using the damage index based on the failure volume, caution should be exercised as this method does not account for localized failure of structural elements, but rather the global behaviour of the structure. The results using the Abaqus feature of removing elements when the damage exceeded a given threshold was compared to the results obtained from viewing the Concrete Tension Damage. Both methods resulted in very similar damage patterns, with the removal of damaged elements method indicating greater damage patterns.

A historical cannonball dating from the 16th and 17th centuries was modelled as an impactor on the *Torre de la Vela*. For this analysis, three models of a wall section of the tower were created: a continuum model, a continuum model with removal of damaged elements, and a contact model. For all these models, no damage was caused by the impactor. Differences in displacement between the continuum models and the contact model existed and were likely a result of the energy dissipation in the structure following impact. Future work should consider a more refined mesh in the region of impact to replicate potential damage on the surface of the wall. To better understand the damage in the continuum model caused by an impactor, a larger hypothetical impactor was modelled. This resulted in localized damage on the surface of the wall, where the diameter of the damage was slightly greater than the diameter of the impactor, and the depth of the damage corresponded to the size of the mesh elements.

Finally, some recommendations for future works on the numerical analysis of the *Torre de la Vela* under blast and impact loading are presented, which aim to improve and validate the conclusions obtained from this work. These recommendations are as follows:

- The analysis of the structural response of the building subjected to internal blast loading should be done for the whole structure. This would allow a better understanding of the global response of the structure when the loading on the structure is localized. Specially considering the slabs which were not considered in this work for the internal blast.
- The global response of the whole structure subjected to both external and internal blast loading should be investigated using the removal of damaged elements. This would give a better understanding of the response without the need to consider excessive deformation.
- A damage level threshold for rammed earth under compression should be investigated. As blast and impact loads add compressive force to the structure, this would allow for a better understanding of the crushing caused by these loading conditions.

REFERENCES

- ABAQUS. (2010). *ABAQUS User's Manual*. Dassault Systèmes.
- Abdelmoneim Elamin Mohamad, A.-B., & Chen, Z. (2016). Experimental and Numerical Analysis of the Compressive and Shear Behavior for a New Type of Self-Insulating Concrete Masonry System. *Applied Sciences*, 6(9), 245. <https://doi.org/10.3390/app6090245>
- Abdulla, K., Cunningham, L., & Gillie, M. (2017). *Non-linear simulation of masonry behaviour under cyclic loads*. 4.
- Altaee, M., Kadhim, M., Altayee, S., & Adheem, A. (2020). Employment of damage plasticity constitutive model for concrete members subjected to high strain-rate. *Proceedings of the 1st International Multi-Disciplinary Conference Theme: Sustainable Development and Smart Planning, IMDC-SDSP 2020, Cyberspace, 28-30 June 2020*. <https://doi.org/10.4108/eai.28-6-2020.2298164>
- Andrade, T. (2016). *The gunpowder age: China, military innovation, and the rise of the west in world history*. Princeton University Press.
- Angus, H. T. (1976). *Cast iron: Physical and engineering properties* (2d ed). Butterworths.
- Asprone, D., Cadoni, E., Prota, A., & Manfredi, G. (2009). Dynamic behavior of a Mediterranean natural stone under tensile loading. *International Journal of Rock Mechanics and Mining Sciences*, 46(3), 514–520. <https://doi.org/10.1016/j.ijrmms.2008.09.010>
- Asteris, P. G., Chronopoulos, M. P., Chrysostomou, C. Z., Varum, H., Plevris, V., Kyriakides, N., & Silva, V. (2014). Seismic vulnerability assessment of historical masonry structural systems. *Engineering Structures*, 62–63, 118–134. <https://doi.org/10.1016/j.engstruct.2014.01.031>
- Baker, W. E., Kulesz, P. S., Wilbeck, J. S., & Cox, P. A. (1980). *A Manual for the Prediction of Blast and Fragment Loadings on Structures* (DOE/TIC-11268; p. 766). US Department of Energy.
- Bangash, M. Y. H., & Bangash, T. (2006). *Explosion-resistant buildings: Design, analysis, and case studies*. Springer.
- Basco, A., Cammarota, F., & Salzano, E. (2010). The risk of storage plant of pyrotechnics. *Chemical Engineering Transactions*, 19, 231–236. <https://doi.org/10.3303/CET1019038>
- Bermudez Lopez, J., Metropolitan Museum of Art (New York, N. Y.), & Patronato de la Alhambra y Generalife (Granada, S. (1992). The City Plan of the Alhambra. In *Al-Andalus: The art of Islamic Spain*. Metropolitan Museum of Art: Distributed by H.N. Abrams.
- Bhosale, S. D., & Desai, A. K. (2019). Simulation of Masonry Wall using Concrete Damage Plasticity Model. *International Journal of Innovative Technology and Exploring Engineering*, 8(9S3), 1241–1244. <https://doi.org/10.35940/ijitee.I3274.0789S319>
- Britannica, T. E. of E. (2019). Alhambra. In *Encyclopedia Britannica*. <https://www.britannica.com/topic/Alhambra-fortress-Granada-Spain>
- Brode, H. L. (1955). Numerical Solutions of Spherical Blast Waves. *Journal of Applied Physics*, 26(6), 766–775. <https://doi.org/10.1063/1.1722085>
- Bui, Q.-B., Bui, T.-T., Tran, M.-P., Bui, T.-L., & Le, H.-A. (2019). Assessing the Seismic Behavior of Rammed Earth Walls with an L-Form Cross-Section. *Sustainability*, 11(5), 1296. <https://doi.org/10.3390/su11051296>
- Bui, Q.-B., Tran, M.-P., & Le, H.-A. (2019). Assessing the Seismic Behavior of Rammed Earth Walls with an L-Form Cross-Section. *Sustainability*, 11(5), 1296. <https://doi.org/10.3390/su11051296>
- Bui, T.-L., Bui, T.-T., Bui, Q.-B., Nguyen, X.-H., & Limam, A. (2020). Out-of-plane behavior of rammed earth walls under seismic loading: Finite element simulation. *Structures*, 24, 191–208. <https://doi.org/10.1016/j.istruc.2020.01.009>
- Burnett, S., Gilbert, M., Molyneaux, T., Tyas, A., Hobbs, B., & Beattie, G. (2007). The response of masonry joints to dynamic tensile loading. *Materials and Structures*, 40(5), 517–527. <https://doi.org/10.1617/s11527-006-9160-6>
- Cannon. (2021). In *Wikipedia*. <https://en.wikipedia.org/wiki/Cannon>
- CEN. (2003). *Eurocode 1: Actions on structures*. European Committee for Standardization.

- Chamoso G, R. (2009). *Campana de la Torre de La Vela de la Alcazaba. La Alhambra, Granada* [Photograph].
https://commons.wikimedia.org/wiki/File:Campana_de_la_Torre_de_La_Vela_de_la_Alcazaba._La_Alhambra,_Granada.JPG
- Chan, P. C., & Klein, H. H. (1994). A Study of Blast Effects Inside an Enclosure. *Journal of Fluids Engineering*, 116(3), 450–455. <https://doi.org/10.1115/1.2910297>
- Circolare 21 gennaio 2019 n.7. (2019). *Istruzioni per l'applicazione dell'«Aggiornamento delle "Norme tecniche per le costruzioni"» di cui al decreto ministeriale 17 gennaio 2018* (Vol. 35).
- Cook, W. F. (1993). The Cannon Conquest of Nasrid Spain and the End of the Reconquista. *The Journal of Military History*, 57(1), 43. <https://doi.org/10.2307/2944222>
- Cormie, D., Mays, G., & Smith, P. D. (2011). *Blast effects on buildings*. Thomas Telford Ltd.
<http://app.knovel.com/hotlink/toc/id:kpBEBE0001/blast-effects-on>
- Cranz, C. (1925). *Lehrbuch der ballistik*. Julius Springer.
- de la Torre López, M. J., Sebastián, P. E., & Rodríguez, G. J. (1996). A study of the wall material in the alhambra (Granada, Spain). *Cement and Concrete Research*, 26(6), 825–839.
[https://doi.org/10.1016/0008-8846\(96\)00075-0](https://doi.org/10.1016/0008-8846(96)00075-0)
- DIANA FEA BV. (2020). *Diana User's Manual, Release 10.4*. DIANA FEA BV.
- Discovery Chanel. (2004, October 25). What Sank the Armada? (Season 1 Episode 4). In *Battlefield Detectives*. Discovery Chanel.
- Dodds, J. D., Metropolitan Museum of Art (New York, N. Y.), & Patronato de la Alhambra y Generalife (Granada, S. (1992). *al-Andalus: The art of Islamic Spain*. Metropolitan Museum of Art: Distributed by H.N. Abrams.
- Doherty, K., Griffith, M. C., Lam, N., & Wilson, J. (2002). Displacement-based seismic analysis for out-of-plane bending of unreinforced masonry walls. *Earthquake Engineering & Structural Dynamics*, 31(4), 833–850. <https://doi.org/10.1002/eqe.126>
- Eggleton, L. (2012). History in the Making: The Ornament of the Alhambra and the Past-Facing Present. *The Journal of Art Historiography*, 6(1), 30.
- Ekström, J. (2017). *Blast and impact loaded concrete structures: Numerical and experimental methodologies for reinforced plain and fibre concrete structures*. Chalmers University of Technology.
- El-Nabouch, R., Bui, Q.-B., Plé, O., & Perrotin, P. (2018). Characterizing the shear parameters of rammed earth material by using a full-scale direct shear box. *Construction and Building Materials*, 171, 414–420. <https://doi.org/10.1016/j.conbuildmat.2018.03.142>
- Fujikake, K., Li, B., & Soeun, S. (2009). Impact Response of Reinforced Concrete Beam and Its Analytical Evaluation. *Journal of Structural Engineering*, 135(8), 938–950.
[https://doi.org/10.1061/\(ASCE\)ST.1943-541X.0000039](https://doi.org/10.1061/(ASCE)ST.1943-541X.0000039)
- Garcia-Pulido, L. J. (2013). The Fortifications built in the Surroundings of the Alhambra by Napoleon's Army. *The International Journal of Fortification and Military Architecture*, 41, 28–48.
- Godio, M., Stefanou, I., & Sab, K. (2018). Effects of the dilatancy of joints and of the size of the building blocks on the mechanical behavior of masonry structures. *Meccanica*, 53(7), 1629–1643.
<https://doi.org/10.1007/s11012-017-0688-z>
- Gómez-Moreno Calera, J. M. (2002). *Estructuras defensivas de la Alhambra, I. Cuestiones Generales* (pp. 125–154).
- Gómez-Moreno Martinez, M. (1907). Granada en el siglo XIII. In *Monumentos arquitectónicos de España* (2nd ed.).
- González Limón, T., & Casas Gómez, A. (1997). Estudio de los materiales y de las fábricas de la Torre de Comares de la Alhambra. *Cuad. La Alhambra*, no. 33, 95–104.
- Griffiths, F. A. (1856). *The artillery's manual and British soldier's compendium*. W.H. Allen.

- Gwei-Djen, L., Needham, J., & Chi-Hsing, P. (1988). The Oldest Representation of a Bombard. *Technology and Culture*, 29(3), 594. <https://doi.org/10.2307/3105275>
- Hall, A. R. (1952). *Ballistics in the seventeenth century: A study in the relations of science and war with reference principally to England* (First published 1952, digitally printed version 2009). University Press.
- Hao, H., & Tarasov, B. G. (2008). Experimental Study of Dynamic Material Properties of Clay Brick and Mortar at Different Strain Rates. *Australian Journal of Structural Engineering*, 8(2), 117–132. <https://doi.org/10.1080/13287982.2008.11464992>
- Hopkinson, B. (1915). *British ordinance board minutes 13565*. The National Archives.
- Hoveidae, N., Fathi, A., & Karimzadeh, S. (2021). Seismic damage assessment of a historic masonry building under simulated scenario earthquakes: A case study for Arge-Tabriz. *Soil Dynamics and Earthquake Engineering*, 147, 106732. <https://doi.org/10.1016/j.soildyn.2021.106732>
- Huan, Y., Fang, Q., Chen, L., & Zhang, Y. (2008). Evaluation of blast-resistant performance predicted by damaged plasticity model for concrete. *Transactions of Tianjin University*, 14(6), 414–421. <https://doi.org/10.1007/s12209-008-0071-1>
- Iqbal, J., & Ahmad, S. (2009). Improving safety provisions of structural design of containment against external explosion. *Proc. International Conference on Opportunities and Challenges for Water Cooled Reactors in the 21st Century*. International Atomic Energy Agency (IAEA).
- Jablonski, J., Carlucci, P., Thyagarajan, R., Nandi, B., & Arata, J. (2012). Simulating Underbelly Blast Events using Abaqus/Explicit—CEL. *2012 SIMULIA Customer Conference*, 16.
- Jaquin, P. A. (2008). *Analysis of historic rammed earth construction* [Durham theses, Durham University]. <http://etheses.dur.ac.uk/2169/>
- Jebulon. (2012). *Torre de la Vela Alhambra* [Photograph]. https://commons.wikimedia.org/wiki/File:Torre_de_la_Vela_Alhambra.jpg
- Kam-wing Wong, J. (2005). *Structures under Impact Loading* [Bachelor Thesis]. University of Cambridge.
- Kinard, J. (2007). *Artillery: An illustrated history of its impact*. ABC-Clio.
- Kinney, G. F., & Graham, K. J. (1985). *Explosive shocks in air*. Springer-Verlag.
- Kmiecik, P., & Kamiński, M. (2011). Modelling of reinforced concrete structures and composite structures with concrete strength degradation taken into consideration. *Archives of Civil and Mechanical Engineering*, 11(3), 623–636. [https://doi.org/10.1016/S1644-9665\(12\)60105-8](https://doi.org/10.1016/S1644-9665(12)60105-8)
- Lancaster, L. C. (2009). Early Examples of So-Called Pitched Brick Barrel Vaulting in Roman Greece and Asia Minor: A Question of Origin and Intention. In M. Bachmann & Deutsches Archäologisches Institut (Eds.), *Bautechnik im antiken und vorantiken Kleinasien: Internationale Konferenz*. Zero Prod. Ltd.
- Lee, J., & Fenves, G. L. (1998). Plastic-Damage Model for Cyclic Loading of Concrete Structures. *Journal of Engineering Mechanics*, 124(8), 892–900. [https://doi.org/10.1061/\(ASCE\)0733-9399\(1998\)124:8\(892\)](https://doi.org/10.1061/(ASCE)0733-9399(1998)124:8(892))
- Liepmann, H. W., & Roshko, A. (1957). *Elements of Gas Dynamics*. Wiley.
- Liu, J., Yan, Q., & Wu, J. (2008). Analysis of blast wave propagation inside tunnel. *Transactions of Tianjin University*, 14(5), 358–362. <https://doi.org/10.1007/s12209-008-0061-3>
- López Bueno, M., & Torres Balbás, L. (1923). *Torre de la Vela*. Patronato de la Alhambra y Generalife.
- López Díaz de la Guardia, F. (1961). *Recinto de la Alhambra* [Copia, papel vegetal, copiativo]. APAG/ Colección de Planos/ P-001053. <https://www.alhambra-patronato.es/ria/handle/10514/16/browse?value=APAG%2F+Colecci%C3%B3n+de+Planos%2F+P-001053&type=identifiier>
- Lourenço, P. B. (2008). *Structural masonry analysis: Recent developments and prospects*. Proc. of the 14th International Brick/Block Masonry Conference, Australia.
- Lourenço, P. B. (2009). RECENT ADVANCES IN MASONRY MODELLING: MICROMODELLING AND HOMOGENISATION. In U. Galvanetto & M. H. F. Aliabadi, *Computational and Experimental*

- Methods in Structures* (Vol. 3, pp. 251–294). IMPERIAL COLLEGE PRESS.
https://doi.org/10.1142/9781848163089_0006
- Lourenço, P. B., Oliveira, D. V., Roca, P., & Orduña, A. (2005). Dry Joint Stone Masonry Walls Subjected to In-Plane Combined Loading. *Journal of Structural Engineering*, 131(11), 1665–1673.
[https://doi.org/10.1061/\(ASCE\)0733-9445\(2005\)131:11\(1665\)](https://doi.org/10.1061/(ASCE)0733-9445(2005)131:11(1665))
- Lourenço, P. B., Pereira, J. M., Getty Conservation Institute, & TecMinho (Guimarães, P. (2018). *Seismic retrofitting project: Recommendations for advanced modeling of historic earthen sites*.
http://hdl.handle.net/10020/gci_pubs/advanced_modeling
- Lourenço, P. B., & Ramos, L. F. (2004). Characterization of Cyclic Behavior of Dry Masonry Joints. *Journal of Structural Engineering*, 130(5), 779–786. [https://doi.org/10.1061/\(ASCE\)0733-9445\(2004\)130:5\(779\)](https://doi.org/10.1061/(ASCE)0733-9445(2004)130:5(779))
- Lublliner, J., Oliver, J., Oller, S., & Oñate, E. (1989). A plastic-damage model for concrete. *International Journal of Solids and Structures*, 25(3), 299–326. [https://doi.org/10.1016/0020-7683\(89\)90050-4](https://doi.org/10.1016/0020-7683(89)90050-4)
- Manucy, A. C. (1949). *Artillery Through the Ages*. United States Department of the Interior.
- Masi, F. (2020). *Fast-dynamic response and failure of masonry structures of non-standard geometry subjected to blast loads* [These de Doctorat]. L'École Centrale de Nantes.
- Meyer, C. S. (2013). Numerical Simulations of the Mechanical Behaviour of Adobe. In *Dynamic Behavior of Materials, Volume 1: Proceedings of the 2012 Annual Conference on Experimental and Applied Mechanics*. Springer New York. <https://doi.org/10.1007/978-1-4614-4238-7>
- Mills, C. A. (1987). The design of concrete structure to resist explosions and weapon effects. *Proceedings of the 1st Int. Conference on Concrete for Hazard Protections*, 61–73.
- Newmark, N. M., & Hansen, R. J. (1961). Design of blast resistant structures. In Harris and Crede (Ed.), *Shock and vibration handbook*. McGraw-Hill.
- Ngo, T., Mendis, P., Gupta, A., & Ramsay, J. (2007). Blast Loading and Blast Effects on Structures – An Overview. *EJSE Special Issue: Loading on Structures*, 17.
- Pavón Maldonado, B. (1971). La Alcazaba de la Alhambra. *Cuad. La Alhambra*, no. 7, 3–34.
- Pereira, J. M. (2014). *Security Evaluation and Design of Structures Subjected to Blast Loading* [Doctoral Thesis]. Universidade do Minho.
- Remennikov, A. M., & Rose, T. A. (2005). Modelling blast loads on buildings in complex city geometries. *Computers & Structures*, 83(27), 2197–2205. <https://doi.org/10.1016/j.compstruc.2005.04.003>
- Reza, A., Ibrahim, Z., & Vaitekunas, T. (2013). Investigation and analysis of an explosion at the goex black powder manufacturing facility. *Chemical Engineering Transactions*, 31, 475–480.
<https://doi.org/10.3303/CET1331080>
- Sadovskiy, M. A. (1952). *Mechanical effects of air shock waves from explosions according to experiments, Selected works: Geophysics and physics of explosion*. Nauka Press.
- Schinz, P. (1984). *Alhambra, Generalife and Albayzín, Granada (Spain)* [Photograph].
whc.unesco.org/en/documents/121659
- Shi, Y., Li, Z.-X., & Hao, H. (2009). Numerical investigation of blast loads on RC slabs from internal explosion. In D. Yankelevsky & H. Hao (Eds.), *Numerical investigation of blast loads on RC slabs from internal explosion: Vol. CD-ROM* (p. CD ROM). Israel Institute of Technology.
- Shrestha, K. C., Aoki, T., Miyamoto, M., Wangmo, P., & Pema. (2020). In-Plane Shear Resistance between the Rammed Earth Blocks with Simple Interventions: Experimentation and Finite Element Study. *Buildings*, 10(3), 57. <https://doi.org/10.3390/buildings10030057>
- Smith, P. D., & Hetherington, J. G. (1994). *Blast and Ballistic Loading of Structures*. Butterworth-Heinemann.
- Tarque, N., Camata, G., Spacone, E., Varum, H., & Blondet, M. (2014). Nonlinear Dynamic Analysis of a Full-Scale Unreinforced Adobe Model. *Earthquake Spectra*, 30(4), 1643–1661.
<https://doi.org/10.1193/022512EQS053M>

- Ullah, A., Ahmad, F., Jang, H.-W., Kim, S.-W., & Hong, J.-W. (2017). Review of analytical and empirical estimations for incident blast pressure. *KSCCE Journal of Civil Engineering*, 21(6), 2211–2225. <https://doi.org/10.1007/s12205-016-1386-4>
- US Army Corps of Engineers, Naval Facilities Engineering Command. (2008). *Structures to Resist the Effects of Accidental Explosions*, Air Force Civil Engineer Support Agency (UFC 3-340-02; p. 1943). US Department of Defense.
- US Army Corps of Engineers, Naval Facilities Engineering Command, Air & Force Civil Engineer Support Agency. (2002). *Design and analysis of hardened structures to conventional weapons effects* (UFC 3-340-01; Supersedes TM5-855-1/NAVFACP-1080/AFJAM32-1055/DSWA DAHSCWEMAN-97 August 1998). US Army Corps of Engineers and Defense Special Weapons Agency.
- Villegas, D. C. (2012). *Análisis estructural del patrimonio histórico: Torre del Homenaje de la Alhambra* [Master de Estructuras, Universidad de Granada]. <https://doi.org/10.30827/Digibug.25169>
- Vuoto, A. (2020). *Numerical safety assessment of earthen structures in La Alhambra, Granada, Spain* [Masters Thesis]. Universidade do Minho.
- Wangmo, P., Shrestha, K. C., Miyamoto, M., & Aoki, T. (2019). Assessment of out-of-plane behavior of rammed earth walls by pull-down tests. *International Journal of Architectural Heritage*, 13(2), 273–287. <https://doi.org/10.1080/15583058.2018.1433903>
- Wu, C., & Hao, H. (2005). Modeling of simultaneous ground shock and airblast pressure on nearby structures from surface explosions. *International Journal of Impact Engineering*, 31(6), 699–717. <https://doi.org/10.1016/j.ijimpeng.2004.03.002>
- Yandzio, E., & Gough, M. (1999). *Protection of buildings against explosions*. Steel Construction Institute.
- Zakrisson, B., Wikman, B., & Häggblad, H.-Å. (2011). Numerical simulations of blast loads and structural deformation from near-field explosions in air. *International Journal of Impact Engineering*, 38(7), 597–612. <https://doi.org/10.1016/j.ijimpeng.2011.02.005>
- Zapata, B. J., & Weggel, D. C. (2008). Collapse Study of an Unreinforced Masonry Bearing Wall Building Subjected to Internal Blast Loading. *Journal of Performance of Constructed Facilities*, 22(2), 92–100. [https://doi.org/10.1061/\(ASCE\)0887-3828\(2008\)22:2\(92\)](https://doi.org/10.1061/(ASCE)0887-3828(2008)22:2(92))
- Žmindák, M., Pelagić, Z., Pastorek, P., Močilan, M., & Vyboštok, M. (2016). Finite Element Modelling of High Velocity Impact on Plate Structures. *Procedia Engineering*, 136, 162–168. <https://doi.org/10.1016/j.proeng.2016.01.191>